DEFORMATION ACROSS THE SEISMIC CYCLE IN TECTONICALLY ACTIVE REGIONS: IMAGING, MODELING, AND INTERPRETATIONS

A Dissertation

Presented to the Faculty of the Graduate School

of Cornell University

in Partial Fulfillment of the Requirements for the Degree of

Doctor of Philosophy

by

William Douglas Barnhart

May 2013

DEFORMATION ACROSS THE SEISMIC CYCLE IN TECTONICALLY ACTIVE REGIONS: IMAGING, MODELING, AND INTERPRETATIONS

William Douglas Barnhart, Ph.D.
Cornell University 2013

Images of surface displacements in response to tectonic forces can provide independent, spatially dense observations that assist in understanding sub-surface processes. When considered independently or augmented with more traditional observations of active tectonics such as seismicity and ground mapping, these measurements provide constraints on spatially and temporally variable fault behavior across the seismic cycle. Models of fault behavior inferred from these observations in turn allow us to address topics in geologic hazards assessment, the long- and short-term character of strain in deforming regions, and the interactions between faults throughout the crust. In this dissertation, I use remotely sensed observations of ground displacements from interferometric synthetic aperture radar (InSAR) to approach several problems related to earthquake and aseismic fault slip. I establish image processing and inverse methods for better detailing subsurface fault slip and apply these to the 2010-2011 Canterbury, New Zealand sequence. Then, I focus on the active tectonics of the Zagros Mountains in southern Iran. There, I show through orogen-wide InSAR time series analysis that active strain is accommodated across the width of the mountain belt. I also use a combination of InSAR, local seismicity, and structural modeling to demonstrate that strain is vertically partitioned within the Zagros fold-and-thrust belt, with earthquakes controlling deformation in the underlying basement while the overlying sedimentary section shortens in transient, earthquake-triggered aseismic slip events. In certain examples, these aseismic slip events directly contribute to the growth of fault-bend folds. I use these inferences to explore a previously noted discrepancy between observed shortening and that which is expected from known earthquakes. I show that the earthquakes and short-term aseismic slip cannot account for this discrepancy, and that additional deformation mechanisms must be active.

BIOGRAPHICAL SKETCH

The story of William (Bill) Barnhart is best understood as an ever-changing arc between social and ideological niches. Born to Sarah and Doug (Barnhart) in Alexandria, Virginia, Bill lived his earliest days in Georgetown South before moving to southeast Virginia and eventually the salty naval capital of Norfolk. In his earliest academic days, Bill learned to read, do algebra, and compete in baseball and basketball at Trinity Lutheran School. His time at Trinity Lutheran was followed by a tour of duty at Christ the King Catholic School for middle school, all whilst attending an Episcopalian church and watching his younger brother play basketball at the local Jewish Community Center (starting to see the ideological arcs?).

In 2000, he moved to Granby High School for his final four years of primary school. There, he split (quite unevenly) his time between studies and athletics. While devoting significant time to baseball and swimming for the Granby Comets, he developed a burgeoning love for the biological sciences, constitutional law, and philosophy. Although baseball would ultimately determine his collegiate path, the sciences were firmly ingrained as a possible, though unlikely necessary, fallback should the major leagues never come calling with a multi-million dollar contract.

After graduating from Granby, Bill moved to the great Shenandoah Valley to begin southern finishing school at Washington and Lee University. Very quickly, Bill realized the major leagues would not be calling anytime soon, so academics would have to be the focus of his time. Initially claiming to be a pre-med student, he found chemistry to be his weak hand after posting a stellar 2.1 GPA his first semester. Needing to regroup, Bill was coaxed into taking an elective course entitled “Geology of the Natural Parks,” and the person you see today began. He

soon took the introductory geology course and was locked into the cultish world of undergraduate geology majors.

After his first college year, Bill followed the adage of many before him and went west. But not very far, just to West Virginia. There he began his double life: Clean college student at a liberal arts college by winter, dirty whitewater raft guide by summer. Guiding the New and Gauley Rivers through all four college summers, Bill learned countless and untellable lessons on life and survival. Upon returning to W&L each fall, he was lovingly (he assumes) referred to as "that guy who disappears into the woods every summer."

2007 was a climactic year for Bill. In the spring, he traveled with a class to New Zealand where he was first introduced to active and neo-tectonics, subjects that would become his vocation in the following years. In the fall, he began the arduous task of figuring out his near future when he contacted Muawia Barazangi at Cornell University, who informed Bill he would no longer be taking students or acting on student committees (see Acknowledgements). Dr. Barazangi in turn introduced Bill to a recently hired, tenure-track professor, Dr. Rowena Lohman (see more Acknowledgements). After a riveting application process and chasing down spam-filtered emails, Bill bravely traveled north of the Mason-Dixon line to the greatest city of Ithaca. Upon that visit, Bill decided he would spend the next few years in central New York. Much to his mother's chagrin, Bill left the south in the fall of 2008 to begin his graduate studies, and this dissertation is the result.

Adventures in graduate school were bountiful, from cougar/ex-president encounters in the Argentine Andes, an appearance on ESPN SportCenter's Top 10, all the way to hitchhiking with truckers from central Idaho to Salt Lake City. Bill's time at Cornell was short though, and 4½ eventful years later, he moves on to new adventures west of the Mississippi.

ACKNOWLEGEMENTS

First and foremost, the work presented in this dissertation was not possible without the funding and data provided through various funding and international space agencies. Principal funding for the included work comes from the Cornell Engineering Long Fellowship, the NASA Graduate Fellow Program, an NSF RAPID grant, a grant through the American Chemical Society Petroleum Research Fund, and two grants from the Southern California Earthquake Center (SCEC). Additionally, raw ERS and Envisat SAR data was provided through a Category-1 proposal through the European Space Agency, and raw ALOS SAR data was provided from the Japanese Space Agency (JAXA) via the Alaska Satellite Facility (ASF). SRTM digital elevation models, Landsat, and MODIS multispectral data were provided through NASA. High-resolution, commercial optical imagery were provided through Digital Globe.

Many acknowledgements and thanks are owed to individuals of the academic community who helped in the shaping and critical development of both this dissertation and myself as a scientists and academic community member. From Washington and Lee University, Lisa Greer introduced me to geology, driving and inspiring me to continually push the envelope of my abilities both inside and outside the classroom. Jeffrey Rahl gave me my first opportunities for both independent research and teaching. Both Lisa and Jeff continue to be invaluable mentors and friends.

At Cornell, several groups and individuals made this experience all the more fruitful and entertaining. The Active Tectonics (Phil, Veronica, Chelsea) and Remote Sensing (Jennifer, Andrew, Scott, Holly, Neesha, Eva, Mike, and Julie) groups made it easier to get up for cold winter Friday mornings and provided plenty of horribly off topic

conversations. This group atmosphere is a style I hope to bring to another department in the future. Participants of the Andes Seminar gave many others and me the opportunity to develop the paramount scientific skill of communication while providing critical, usually useful, knife wielding research critiques.

Individually, I want to thank Phoebe Judge for giving me a non-southern reeducation, putting my pillow in the way of pumas, and selflessly allowing me to tell our tales of Argentina to former heads of state; Chris Andronicos for pushing me to think beyond the obvious interpretations; Chris Connors for staring at interferograms and GoogleEarth for many hours with me; Julie Elliot for commiserating with me about job applications and website creation; George Hade for your ribbing and help in my beer making adventures; Larry Brown, CC, and Diego for your constant support and enthusiasm, the opportunities to become a seismologist, and most of all, for allowing me to bring my trade to my home, even if I wasn't able to teach you what poison ivy looked like until it was too late. To my family, thank you for always embracing my decisions and continuing to support me through everything I try to tackle.

To Dr. Mary K., you made this experience more fulfilling than I could have ever hoped, even if you were implicit in my rampant coffee addiction. You have been nothing short of my best friend, partner, fellow hockey instigator, and, most unlikely, paleontology colleague. I look forward to many more years of ups and downs, Colorado adventures, and cabining with your family.

To my committee members: Wilkins, thank you for commandeering my Q-exam and addressing all the topics for which I had explicitly prepared, and thank you for preparing me to address colleague across multiple fields; Derek, thank you for graciously

stepping in late in my grad school tenure and for energetically saying hi to me on the streets despite probably having no clue who I was for the longest time. To Muawia, thank you for your education about the history of plate tectonics, Middle Eastern geology and politics, and for your "encouragement" from the back row during Andes Seminars. It is truly an honor to be apart of your last committee assignment, though I doubt I will indeed be the last. To Rick, thank you for your always welcomed and constructive critiques and for your mentorship beyond research. You have truly shown me how to be a better scientist. You also provided me with two of my best stories from grad school: "The time I went to Argentina," and "The time the professor told me 'That was the worst talk ever.'" And to Matt, though you were not on my committee, you provided invaluable advice and mentoring, both in and away from research, throughout my time at Cornell.

Most of all, I thank Rowena. It would be naïve to think I could have accomplished anything at Cornell beyond just showing up without your guidance and advising. You took a field geologist stuck on lower-crustal microstructures in the Swiss Alps, and turned me into ::*gasp*:: a computer modeling, image processing geophysicist. I am so thankful for not only your guidance in research, but also your encouragement of my growth as an educator, colleague, and individual. You have been an invaluable mentor, showing me the ways of toilet demolition, freeway diaper changing (I originally spelled diapir here), and the correct spelling of "assess." You exhibited infinite patience through my many near-meltdowns and entertained some of my craziest ideas. I am proud to say I got to be your first PhD student, and I hope I can live up to a mere fraction of the expectations that come from being "A Lohman Student." Thank you.

TABLE OF CONTENTS

Biographical Sketch iii
Acknowledgements v
Table of Contents viii

CHAPTER ONE: 1
Introduction 1
1.1 Introduction
1.2 References 4

CHAPTER TWO: 6
Background: InSAR and Inverse Methods
2.1 Introduction 6
2.2 General Methods
2.2.1 InSAR 6
2.2.1.1 Interferogram Formation 7
2.2.1.2 InSAR Noise Sources 11
2.2.2 Source Inversions 16
2.2.3 Fault Slip Resolution 18
2.3 References 22

CHAPTER THREE 26
Automated Fault Model Discretization
3.1 Abstract 26
3.2 Introduction 27
3.3 Method 29
3.3.1 Slip Inversion and Model Resolution 29
3.3.2 Model Construction 33
3.3.3 Downsampling 34
3.3.4 Complete Model Resampling 35
3.4 Synthetic Tests 38
3.4.1 Setup 38
3.4.2 Synthetic Inversion Results 42
3.5 Real Data Inversions 45
3.5.1 The 2004 Parkfield Strike-Slip Event 45
3.5.1.1 Data and Model Parameters 46
3.5.1.2 Inversion Results 47
3.5.2 The 1995 Antofagasta Subduction Zone Event 50
3.5.2.1 Data and Model Parameters 51
3.5.2.2 Inversion Results 53
3.6 Conclusions 54
3.7 References 56

CHAPTER 4 60
InSAR and Optical Constraints on Fault Slip During the 2010-2011 New Zealand Earthquake Sequence

4.1 Introduction 60
4.2 Tectonic Setting 61
4.3 Data: Availability and Processing Results 64
4.4 Modeling Results 71
4.4.1 Darfield Earthquake 71
4.4.2 Christchurch Earthquakes 73
4.4.3 Coulomb Stress Change 74
4.5 Discussion 75
4.6 Conclusions 77
4.7 References 78

CHAPTER 5 82
Zagros Time Series and Regional Trends in Active Diapirism
5.1 Abstract 82
5.2 Introduction 82
5.3 Zagros Mountains and Hormuz Diapirism 84
5.4 Methods: InSAR Time Series 86
5.5 Results and Discussion 90
5.6 References 93

CHAPTER 6 98
Phantom Earthquakes and Triggered Aseismic Creep: Vertical Strain Partitioning During Earthquake Sequences in Iran
6.1 Abstract 98
6.2 Introduction 98
6.3 The Zagros Mountains and Disagreement Between Data Types 100
6.4 Fault Slip Resolution 102
6.5 Discussion 106
6.6 References 109

CHAPTER 7 113
Accommodation of Arabian-Eurasian Convergence in Southern Iran from InSAR, GPS, and Seismology
7.1 Introduction 113
7.2 Active Tectonics of Southern Iran 115
7.3 Surface Deformation Sources 118
7.3.1 InSAR Data and Analysis 118
7.3.2 InSAR Results 121
7.3.2.1 Zagros SFB Events 121
7.3.2.2 Missing Events 124
7.3.2.3 2010-2011 Lut Block Slip Sequence 125
7.3.3 InSAR-Seismic Misfit 126
7.4 Geodetic and Seismic Strain Rates 129
7.4.1 Calculating Strain Rates 130
7.4.2 Results: A Persistent Slip Discrepancy 133
7.5 Discussion 134

7.6 Conclusions 136
7.7 References 137

Appendix A.1: $_j\mathfrak{R}_i$ Regularization 143
A.1.1 Regularization 143
A.1.2 Calculating $_j\mathfrak{R}_i$ for Exact Data 145
A.1.3 Approximating $_j\mathfrak{R}_i$ for Real Data: $_j\mathfrak{R}_i^a$ 147

Appendix A.2: InSAR Acquisitions for Iran 149

Appendix A.3: Iran Slip Distributions 151

CHAPTER 1

INTRODUCTION

1.1 Introduction

Since the 1960s, global studies of earthquakes from seismology have provided a strong framework for our understanding of how strain is accommodated along active plate boundaries. More recently, geodetic observation of ground displacements in response to tectonic forces have illuminated a spectrum of "silent" modes of transient deformation [*Barnhart and Lohman*, accepted; *Dragert et al.*, 2001; *Peng and Gomberg*, 2010], as well as providing independent and, often, spatially dense measurements of earthquake deformation [e.g., *Bürgmann et al.*, 2000; *Fialko et al.*, 2001; *Simons et al.*, 2002]. When used in concert, seismic and geodetic observations, both in-situ and remotely sensed, can allow researchers to constrain the spatially and temporally variable complexities of active deformation - characteristics that are critical for the assessment of geologic hazards, plate boundary stress evolution, earthquake physics, and links between short- and long-term geologic strain rates.

This dissertation concentrates on the imaging, modeling, and interpretation of tectonically driven ground displacements captured by remote sensing geodetic observations, principally Interferometric Synthetic Aperture Radar (InSAR). I focus primarily on the active tectonics of the Zagros Mountains of southern Iran. The Zagros are an ideal natural laboratory for studies of active tectonics using InSAR owing to superb imaging conditions (arid, gentle relief, ample SAR acquisitions) and several frequently active sources of observable ground deformation (earthquakes, aseismic slip, groundwater

and hydrocarbon withdrawal). The Zagros are an exceptional example of an active salt-detached fold-and-thrust belt with high seismicity rates wherein an 8-10km thick sedimentary section is separated from underlying crystalline Arabian basement by the extraordinarily thick (1-2km) infra-Cambrian Hormuz Salt [*Falcon*, 1974; *Stocklin*, 1974]. While likened to the early stages of the more famous Himalayan orogeny [*Ni and Barazangi*, 1986; *Hatzfeld and Molnar*, 2010], many aspects of the active tectonics of the Zagros orogeny are poorly resolved, due mainly to political inaccessibility and difficulties in seismic imaging of salt-laden regions. Satellite-based observation of deformation, integrated with seismic observations, provide the opportunity to address several unsettled questions concerning the active accommodation of continental collision in the Zagros. Issues specifically addressed in this dissertation include:

1. What are the depths of common and moderate (<Mw 6.5) thrust and strike-slip type earthquakes?
2. What are the time scales and modes of aseismic strain that account for the significant (~80%) seismic strain rate deficit inferred across the mountain belt [*Jackson and McKenzie*, 1988; *Masson et al.*, 2005]?
3. How does strain accommodation vary spatially and with depth within the fold-and-thrust belt?
4. Are large (>Mw 6.5-7.0) earthquakes likely in the future in this region, which has poor earthquake engineering standards and a history of devastating events, such as the 2003 Bam Earthquake (>26,000 deaths)?

In Chapters 2 and 3, I establish the methodologies, advantages, and limitations of InSAR

imaging techniques and inverse methods for generating models of sub-surface fault slip [*Barnhart and Lohman*, 2010]. In Chapter 4, I apply these techniques to the 2010-2011 Canterbury, New Zealand earthquake sequence to highlight one application of modeling earthquake fault slip and evaluating the stress interaction between earthquakes [*Barnhart et al.*, 2011]. In Chapter 5, I develop and present an orogen-wide InSAR time series across the Zagros Mountains that images the currently deforming diapirs of Hormuz Salt across the mountain belt [*Barnhart and Lohman*, 2012]. I use these flowing diapirs as strain markers to show that shortening is distributed across the width of the mountain belt, not concentrated at the mountain front, and that the Zagros Mountains simultaneously undergo thin- and thick-skinned style deformation. In the final two chapters, I examine earthquake-like surface displacements that appear in co-seismic interferograms. I show that the displacements signals dominating individual interferograms result from significant aseismic fault slip within the 8-10km thick sedimentary section that is likely triggered by deeper earthquakes with similar magnitude in the underlying crystalline basement [*Barnhart and Lohman*, accepted]. These observations demonstrate that the style of shortening (aseismic vs. seismic fault slip) is vertically partitioned in the Zagros and that earthquakes are likely relegated to the basement while the sedimentary section shortens aseismically. The prodigious moment associated with the triggered aseismic slip, which is equal to or greater than the earthquake magnitude itself, shows that significant aseismic shortening in the Zagros is accommodated on the time scales of days to weeks following individual earthquakes. However, I show that these coupled earthquake-aseismic slip events cannot account for the full shortening inferred from GPS

across the mountain belt [*Barnhart et al.*, in prep]. The remaining strain budget can be accounted for by one earthquake as large as Mw6.8-7.0 per year, but this is unlikely given the lack of such events in the instrumental and historical records. Instead, I suggest the remaining shortening occurs as a combination of long-term continuous deformation and, potentially, transient aseismic deformation events occurring during other portions of the interseismic period.

1.2 References

Barnhart, W. D., and R. B. Lohman (accepted), Phantom earthquakes and triggered aseismic creep: Vertical partitioning of strain during earthquake sequence in Iran, *Geophys. Res. Lett.*

Barnhart, W. D., and R. B. Lohman (2010), Automated fault model discretization for inversions for coseismic slip distributions, *J. Geophys. Res.*, *115*(B10), B10419, doi:10.1029/2010JB007545.

Barnhart, W. D., and R. B. Lohman (2012), Regional trends in active diapirism revealed by mountain range-scale InSAR time series, *Geophys. Res. Lett.*, *39*(8), L08309, doi:10.1029/2012GL051255.

Barnhart, W. D., R. B. Lohman, and R. J. Mellors (in prep), Accommodation of active plate convergence in southern Iran from InSAR, GPS, and seismicity,

Barnhart, W. D., M. J. Willis, R. B. Lohman, and A. K. Melkonian (2011), InSAR and Optical Constraints on Fault Slip during the 2010–2011 New Zealand Earthquake Sequence, *Seismological Research Letters*, *82*(6), 815–823, doi:10.1785/gssrl.82.6.815.

Bürgmann, R., P. A. Rosen, and E. J. Fielding (2000), Synthetic Aperture Radar Interferometry to Measure Earth's Surface Topography and Its Deformation, *Annual Review of Earth and Planetary Sciences*, *28*(1), 169–209, doi:10.1146/annurev.earth.28.1.169.

Dragert, H., K. Wang, and T. S. James (2001), A Silent Slip Event on the Deeper Cascadia Subduction Interface, *Science*, *292*(5521), 1525–1528, doi:10.1126/science.1060152.

Falcon, N. (1974), Zagros Mountain, Mesozoic-Cenozoic Orogenic Belts, *Geological*

Society, London, *Spec. Pub. 4*, 199–211.

Fialko, Y., M. Simons, and D. Agnew (2001), The complete (3‐D) surface displacement field in the epicentral area of the 1999 MW 7.1 Hector Mine Earthquake, California, from space geodetic observations, *Geophys. Res. Lett.*, *28*(16), 3063–3066, doi:10.1029/2001GL013174.

Hatzfeld, D., and P. Molnar (2010), Comparisons of the kinematics and deep structures of the Zagros and Himalaya and of the Iranian and Tibetan plateaus and geodynamic implications, *Rev. Geophys.*, *48*(2), RG2005, doi:10.1029/2009RG000304.

Jackson, J., and D. McKenzie (1988), The relationship between plate motions and seismic moment tensors, and the rates of active deformation in the Mediterranean and Middle East, *Geophysical Journal*, *93*(1), 45–73, doi:10.1111/j.1365-246X.1988.tb01387.x.

Masson, F., J. Chéry, D. Hatzfeld, J. Martinod, P. Vernant, F. Tavakoli, and M. Ghafory-Ashtiani (2005), Seismic versus aseismic deformation in Iran inferred from earthquakes and geodetic data, *Geophysical Journal International*, *160*(1), 217–226, doi:10.1111/j.1365-246X.2004.02465.x.

Ni, J., and M. Barazangi (1986), Seismotectonics of the Zagros continental collision zone and a comparison with the Himalayas, *J. Geophys. Res.*, *91*(B8), 8205–8218, doi:10.1029/JB091iB08p08205.

Peng, Z., and J. Gomberg (2010), An integrated perspective of the continuum between earthquakes and slow-slip phenomena, *Nature Geoscience*, *3*(9), 599–607, doi:10.1038/ngeo940.

Simons, M., Y. Fialko, and L. Rivera (2002), Coseismic Deformation from the 1999 Mw 7.1 Hector Mine, California, Earthquake as Inferred from InSAR and GPS Observations, *Bulletin of the Seismological Society of America*, *92*(4), 1390–1402, doi:10.1785/0120000933.

Stocklin, J. (1974), Possible ancient continental margins in Iran, in *Geology of Continental Margins*, pp. 873–877, Springer, New York.

CHAPTER 2

BACKGROUND: INSAR AND INVERSE METHODS

2.1 Introduction

In this chapter, I discuss the theory and application of basic methodologies implemented throughout this dissertation. I focus on my primary data source – Interferometric Synthetic Aperture Radar (InSAR) – and general inverse methods for generating maps of sub-surface fault slip. I also introduce statistical methods that are used to estimate the contributions of various assumptions to fault slip inversions. More focused and problem-specific methodologies, such as resolution-based fault parameterization, InSAR time series, and treatment of optical imagery in geodesy are explained in subsequent chapters.

2.2 General Methods

2.2.1 InSAR

Interferometric Synthetic Aperture Radar (InSAR) is a form of imaging geodesy that records ground displacements between two Synthetic Aperture Radar (SAR) images (Figure 2.1). InSAR observations provide spatially dense (pixel sizes on the order of meters) measurements of ground displacement and topography on a nearly global scale over land. In deformation applications, images acquired at different times can record surface displacements due to earthquakes, volcanoes, landsliding, among other geologic activity. Because measurements are obtained remotely from air or space-borne platforms, InSAR allows the study of ground deformation events in inaccessible and/or remote regions without the fieldwork that would be necessary for other geodetic techniques such as GPS. Furthermore, radar allows measurements at night and over cloudy regions which is not possible with optical remote sensing methods. InSAR

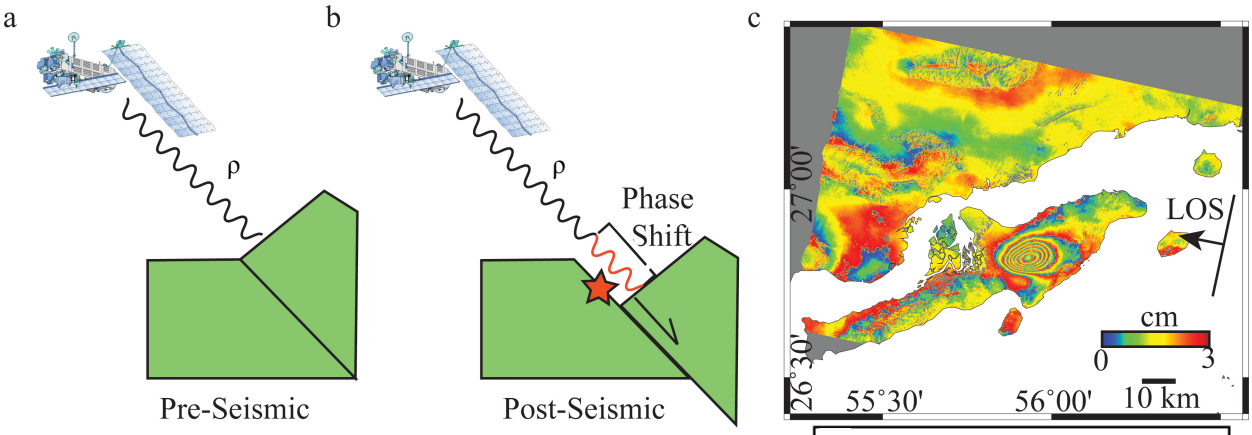

Figure 2.1: Illustration of interferogram formation for ground deformation events. a) Pre-seismic and b) post-seismic scenes measure radar phase returns from the ground. If the ground moves, a phase shift occurs that can be related to ground displacement. Phase shifts for every pixel in the scene are measured to produce an interferogram (c). Arrows and LOS indicate the satellite line-of-sight. d) Spatial geometry between subsequent SAR acquisitions. $B_\perp$: perpendicular baseline between satellites, ρ: the distance between the satellite and a pixel (range distance), and θ: the satellite incidence angle.

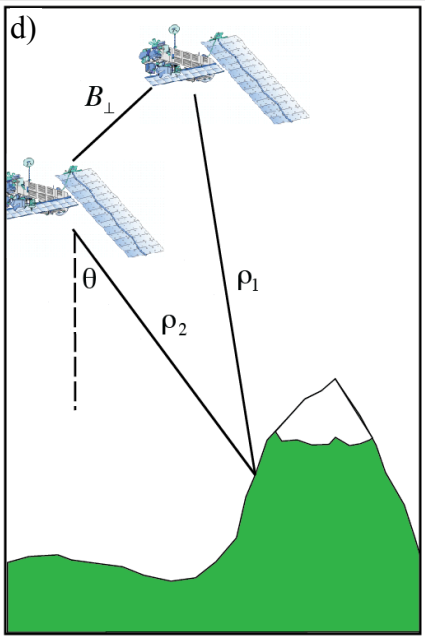

observations used in the accompanying studies are satellite-based from four instruments – the European Space Agency's ERS-1, ERS-2, and Envisat C-band (6cm wavelength) radars and the Japanese Space Agency's ALOS L-band (24cm wavelength) radar.

2.2.1.1 Interferogram Formation

Interferograms are formed by differencing radar phase observations from two SAR acquisitions separated in space and/or time (Figure 2.1):

$$\varphi = 4\pi/\lambda\ (\rho_2 - \rho_1) \qquad \text{eq. 2.1}$$

where **φ** is the phase shift between acquisitions, **λ** is the radar wavelength, and **ρ** is the distance between the satellite antennae and a point on the ground (the range direction, Figure 2.1d) [*Burgmann et al.* 2000]. In a single SAR acquisition, the phase of the reflected radar pulse is

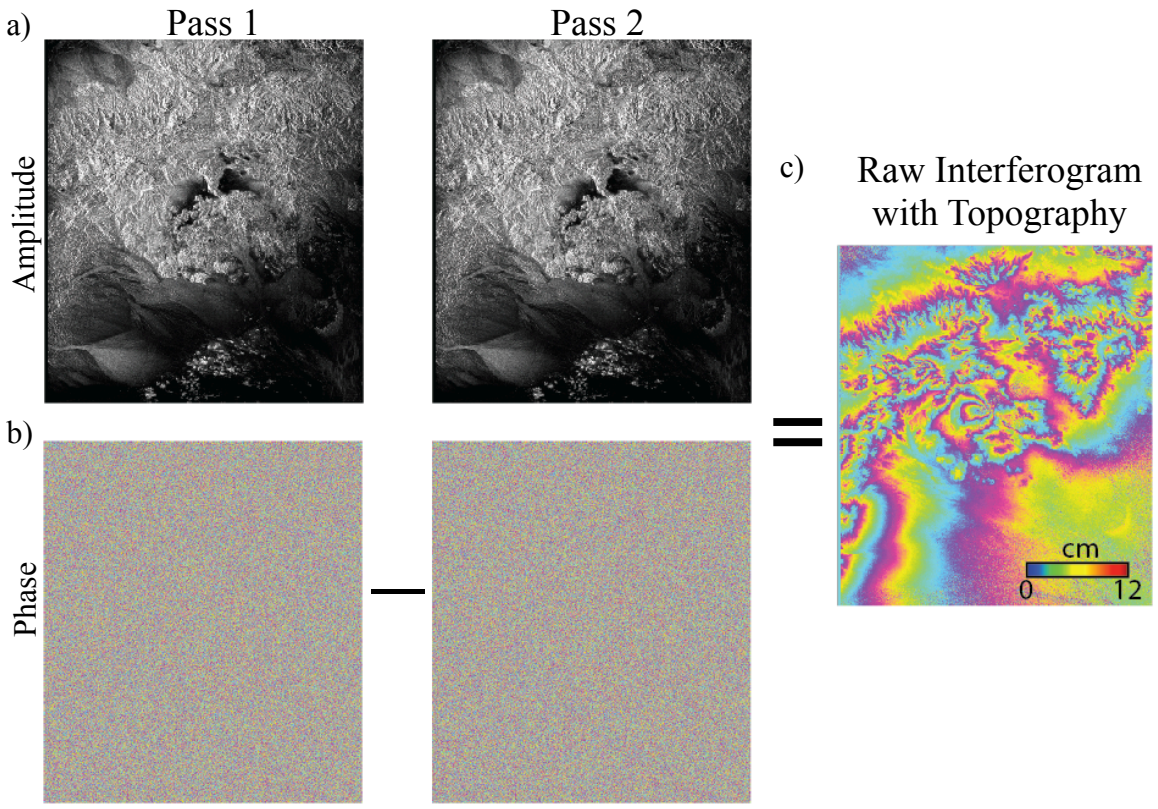

Figure 2.2: Raw interferogram formation. a) Amplitude images from two acquisitions show a coherent image of the ground and are used to coregister ("line-up") the two passes, b) phase in each acquisition is random. Phases from both acquisitions are differenced from coregistered images to produce a raw interferogram that is dominated by topographic signal (c).

random (Figure 2.2b) and the amplitude provides an image of the Earth's surface within the radar footprint (Figure 2.2a). If the scattering properties of the pixel do not change dramatically between the two acquisitions, the differenced phases form a coherent image of phase shifts measured in radians (Figure 2.1c, 2.2c). A single 2π cycle (or "fringe") in an interferogram is equivalent to half the radar's wavelength. These fringes can be thought of as contours of motion and topography; for example one cycle in a L-band (24cm) interferogram is 12cm of motion toward or away from the satellite (Figure 2.2c). Interferograms are sensitive to only one component of the full-three dimensional displacement field, the satellite's line of sight (LOS), which is near-vertical for most satellites. When multiple viewing geometries are available, those

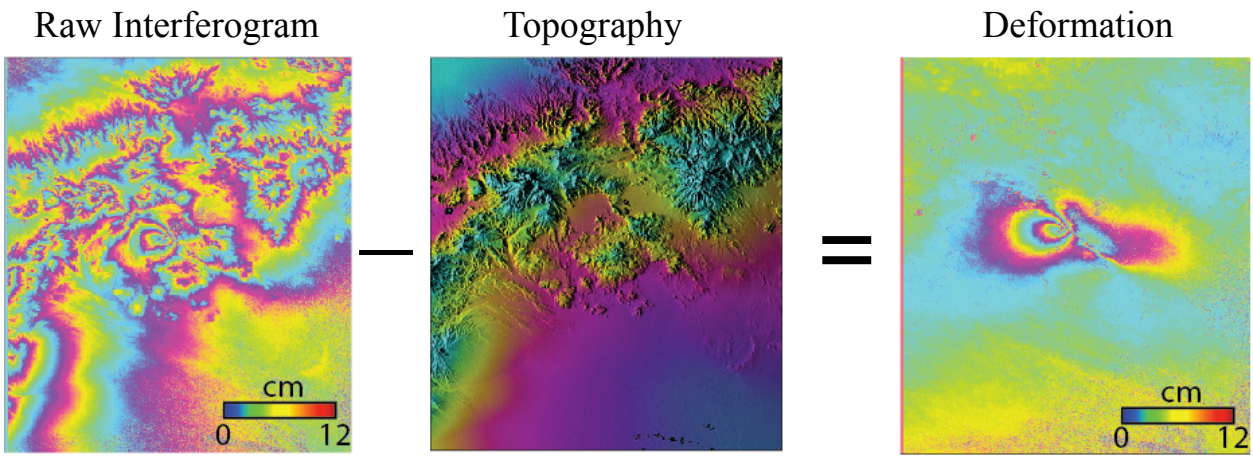

Figure 2.3: Removal of topographic signal from the raw interferogram to produce an interferogram showing only ground displacement and noise.

interferograms can place constraints on the full three-dimensional displacement field. This can be achieved by using multiple interferograms from different orbital look directions (descending tracks move from north to south, ascending tracks from south to north) or by augmenting with other data, including GPS or the offsets of individual pixels in optical and SAR imagery, as discussed in Chapter 4.

The signal in a raw interferogram (φ_{raw}, Figure 2.3a) includes contributions from topography (φ_{topo}), ground deformation (φ_{def}), variations in the properties of the atmosphere (φ_{atmos}) and ionosphere (φ_{ion}) along the path between the satellite and the ground, as well as inaccurate orbital position estimates (φ_{inst}) and changes in the reflective properties of the ground surface (φ_{corr}):

$$\varphi_{raw} = \varphi_{topo} + \varphi_{def} + \varphi_{atmos} + \varphi_{ion} + \varphi_{inst} + \varphi_{corr} \qquad \text{eq. 2.2}$$

The final four terms in equation 2.2 can be considered noise terms for tectonic deformation applications and are discussed in the following section. The phase from topography (φ_{topo}) results when the satellite is not in the exact same orbit on both passes (Figure 2.1d). The magnitude of the topographic phase shift is linearly dependent on perpendicular baseline ($B_{\perp}$, the

physical distance in orbit between the satellite passes, Figure 2.1d) [e.g., *Burgmann et al.,* 2000]:

$$\phi_{topo} = \rho \cos\left[\sin^{-1}\left(\frac{\lambda\phi_{raw}}{2\pi B_{\perp}}\right)\right] \qquad \text{eq. 2.3}$$

A model of topography, such as a digital elevation model (DEM), is used to remove the topographic signal, leaving measurements of phase shift caused by ground displacement and noise (Figure 2.3). To convert the interferogram signal into meaningful measurements of ground displacement, the interferogram phase is "unwrapped" (Figure 2.4) [*Goldstein et al.,* 1988, *Chen and Zebker,* 2001], meaning the 2π phase contours are summed to produce an image of the physical ground displacements in the instrument line-of-sight. The unwrapped interferogram is then geocoded for modeling of deformation signals, mapping, or other applications (Figure 2.4 a-b). In most instances, I use the Caltech/JPL ROI_PAC processing package [*Rosen et al.*, 2004] to form interferograms, remove topographic effects with the Shuttle Radar Topography Mission (SRTM) DEM [*Farr et al.*, 2007], and unwrap using either a branch-cut algorithm

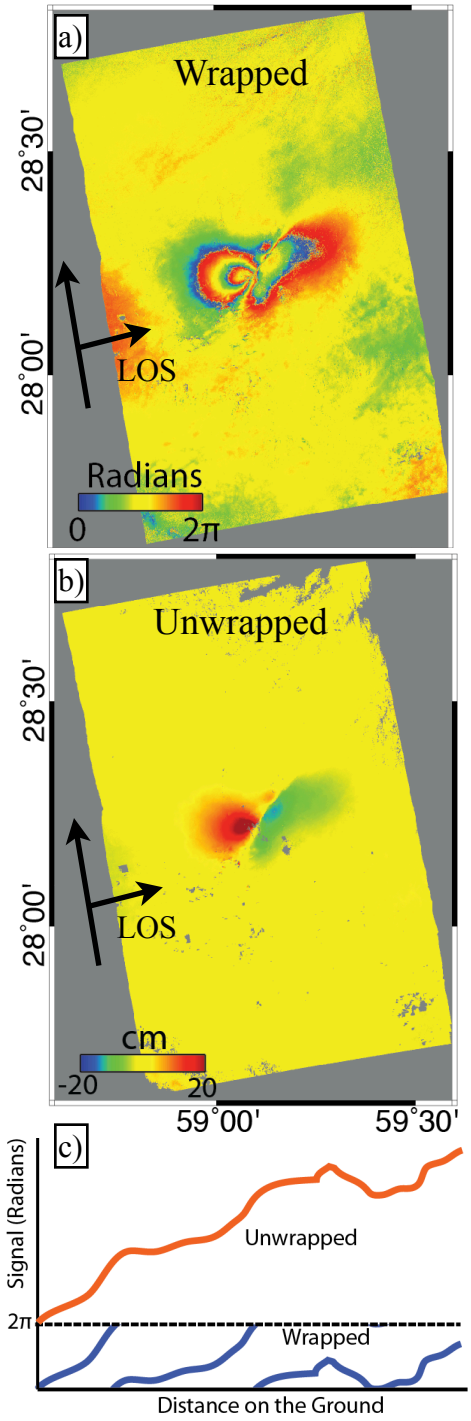

Figure 2.4: Example of a wrapped (a) and unwrapped (b) ALOS interferogram. Earthquake is the 2010 Mw 6.5 Makran strike-slip event (Chapter 7). Arrows indicated satellite orbital path and look direction (LOS). c) Schematic comparison of wrapped vs. unwrapped phase in 2-dimensions.

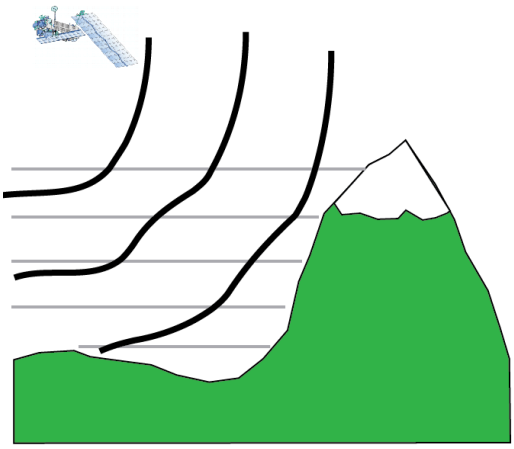

Figure 2.5: Illustration of SAR phase delays (black arcs) through the stratified atmosphere (gray lines). SAR phase is refracted through stratified layers, leading to topographically-correlated signal in repeat acquisitions when atmospheric water vapor characteristics change.

[*Goldstein et al.,* 1988] or SNAPHU [*Chen and Zebker,* 2001].

2.2.1.2 InSAR Noises Sources

In addition to topography and ground displacements, interferograms include signals that are attributed to various noise sources. One major source of noise in interferograms is correlated atmospheric noise caused by phase delays as the radar signal passes through the stratified atmosphere [e.g., *Emardson et al.* 2003] (Figure 2.5). Water vapor concentrations in the atmosphere vary in time, so different delays at each acquisition date result in apparent displacements called the "wet delay." Wet delay can be substantial, as much as several centimeters [e.g., *Emardson et al.* 2003, *Lohman and Simons* 2005] over short spatial wavelengths (<10km), and wet delays signals are often spatially correlated with topography (Figure 2.5-2.7). This noise is problematic in studies of deformation sources that produce small magnitude surface displacements (e.g. deep, small source) or where the expected tectonic signal mimics topography (e.g. mountain uplift). In addition to correlating spatially, atmospheric noise is non-stationary, meaning the characteristics of spatial correlation change across a single interferogram [*Barnhart and Lohman,* in prep] (Figure 2.7). This means that wet delays in interferograms cannot simply be "corrected" by removing functional fits between signal and topography.

There are several techniques to mitigate the effects of correlated atmospheric noise. In investigations of single deformation events, we exploit the redundancy of the signal of interest

by using multiple interferograms with independent acquisitions dates. With this technique, a single interferogram with substantial atmospheric noise does not dominate the deformation source inversion. We can also estimate the covariance of the noise [*Lohman and Simons*, 2005a] in order to down-weight the contribution of a noisy interferogram during the inversion.

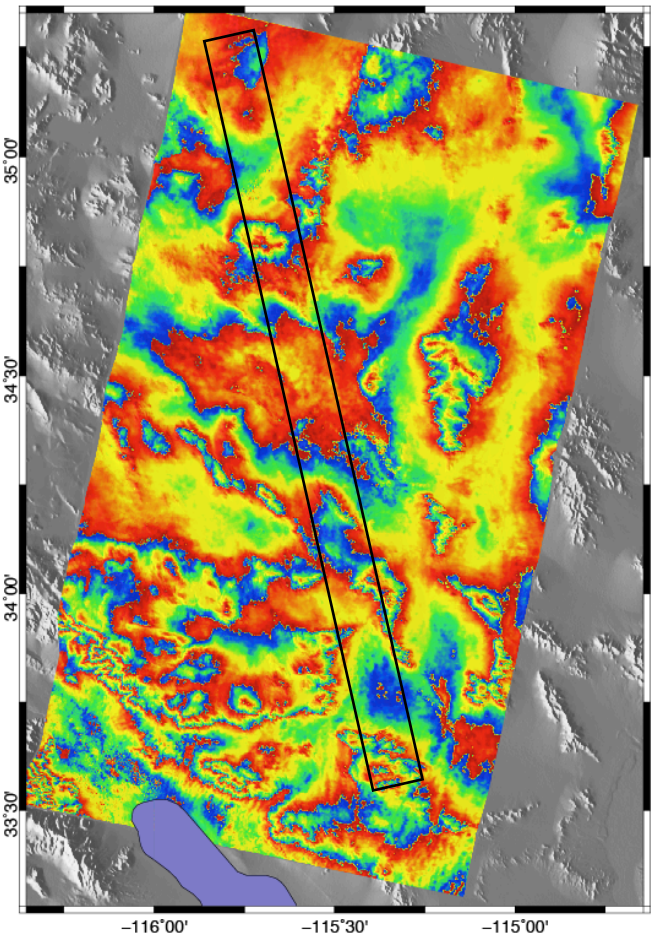

Figure 2.6: A single, one-month Envisat (C-band) wrapped interferogram over the stable (non-deforming) Mojave Desert in southern California. Observed signals are topo-correlated atmospheric noise. Points within the box are shown in Figure 2.7.

Another method for minimizing the impact of atmospheric noise is to stack (average) interferograms or generate InSAR time series. In theory, the sign of wet delay variations due to the atmosphere are random in time. For example, in one interferogram, a non-deforming basin may appear to uplift; whereas, in a separate interferogram with independent acquisitions, that same basin may appear to subside, both instances due to noise in the data. If sufficient interferograms are available, when we "stack" interferograms – adding multiple pairs then dividing by the total time interval to produce a mean LOS velocity map– the wet delay should average out to zero, leaving only the tectonic signal [e.g., *Fialko* 2006]. Similarly, in InSAR time series analysis, a technique that uses many interferograms to solve for the time-variable ground displacement history

(discussed in Chapter 5) [*Ferretti et al.*, 2001; *Berardino et al.*, 2002; *Hooper et al.*, 2004], the average displacement rates over the full set of interferograms caused by wet delay should average out to zero. In practice, because of the limited number of available SAR acquisitions and their irregular seasonal distribution, displacement rates from the wet delay do not average out to zero in InSAR time series, even in best-case scenarios where many SAR acquisitions exists (e.g. Southern California, Figure 2.8) [*Barnhart and Lohman*, in prep]. For tectonic applications, this non-zero apparent deformation is most problematic in locations of large topographic relief where we expect tectonic signals to both mimic topography and be near the detection threshold of the time series (e.g., interseismic deformation across faults). Interferogram stacking and time series techniques greatly reduce the magnitude of the wet delay (Figure 2.8); however, the aforementioned residual displacement rates across major topographic structures in non-deforming regions are often near the magnitude and spatial wavelength of expected interseismic displacements rates in deforming regions.

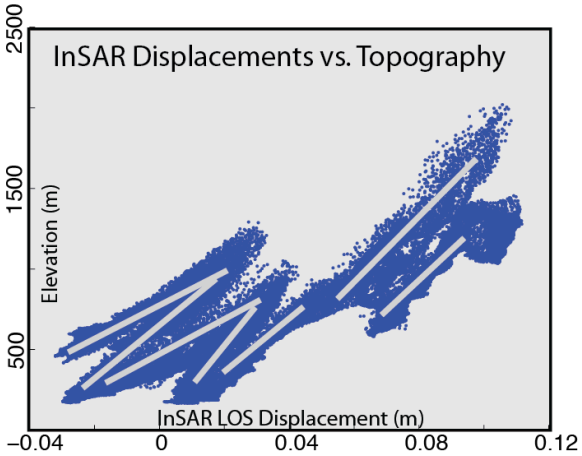

Figure 2.7: InSAR displacements verses topography from the profile in Figure 2.6. Trends indicate correlation between displacements and elevation. Variations in the slope of trends indicates the noise is non-stationary.

To understand the contribution of wet delay in InSAR time series measurements where ground-based measurements of atmospheric water vapor properties are not available, we can use independent measurements of atmospheric water vapor from remote sensing instruments such as the Moderate Resolution Imaging Spectroradiometer (MODIS, Figure 2.8) [e.g., *Barnhart and Lohman*, in prep; *Li et al.,* 2005, *Fournier et al.*, 2011]. MODIS is a multispectral satellite-borne

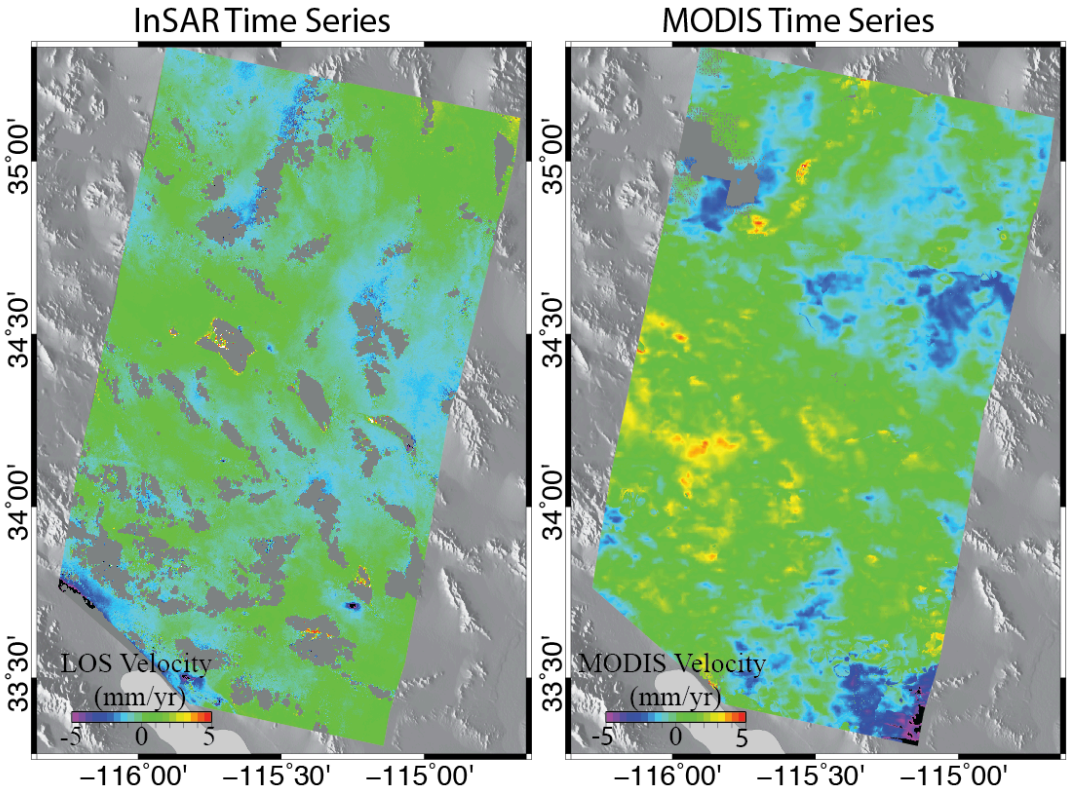

Figure 2.8: Comparison between an InSAR and single MODIS time series over the Mojave Desert, CA. The MODIS (right) and InSAR (left) time series exhibit similar topography correlated signals, showing that the wet delay does not average to zero for this particular set of acquisitions.

instrument that senses the integrated concentration of water vapor in the atmosphere at the time of the acquisition. We create "MODIS Interferograms" by differencing two MODIS acquisitions at similar acquisition dates as the available SAR images. These measurements are then converted to a wet delay in the SAR line-of-sight to provide an estimate of the contribution of atmospheric noise to observed signals in a single SAR interferogram:

$$IWD = \frac{PWV}{\Pi}\cos\theta \qquad \text{eq. 2.4}$$

where **IWD** is the wet delay projected into the radar line-of-sight, **PWV** is precipitable water vapor measured with MODIS, Π is a dimensionless conversion factor analytically determined from GPS and weather models [*Bevis et al.,* 1992], and θ is the radar incidence angle (Figure

2.1d) [*Li et al.,* 2005]. MODIS observations are acquired on a nearly daily basis, but we cannot use these observations to directly correct interferograms because MODIS data is not acquired at the same time of day as SAR, is often not available due to cloudiness or nighttime observation, and is not acquired at the same look angle. Instead of directly comparing MODIS and InSAR noise, we construct many MODIS time series with similar date pairs as an InSAR time series (Figure 2.8). By building multiple MODIS time series, we can assess the likelihood of biases introduced by our SAR acquisition history, and we are able to identify InSAR time series surface displacements that are likely significant and larger than the expected noise [*Barnhart and Lohman*, in prep].

Other sources of noise in InSAR are typically not as substantial as atmospheric noise but can nonetheless inhibit imaging of both large and small magnitude tectonic signals. Signal decorrelation (φ_{corr}, eq.2.2; empty regions in Figure 2.8) caused by changes in ground properties from processes such as weathering, snow, or large ground displacements leads to phase shifts that are no longer spatially coherent and appear as white noise. While there are image filtering and coregistration techniques that can overcome some of these effects, decorellated signals cannot be used to determine useful ground displacements. Similarly, DEM errors introduce spurious phase shifts during topographic signal removal. Lastly, imprecise estimates of perpendicular baseline (φ_{inst}, eq. 2.2) between two SAR acquisitions leads to long-wavelength signals across an interferogram, commonly referred to as the orbital ramp. In most cases, orbital ramps can be estimated and removed by subtracting a polynomial surface from the scene. Although this step does not substantially degrade signals such as those associated with moderate-sized earthquakes and volcanoes, it does remove signals with long spatial wavelengths such as

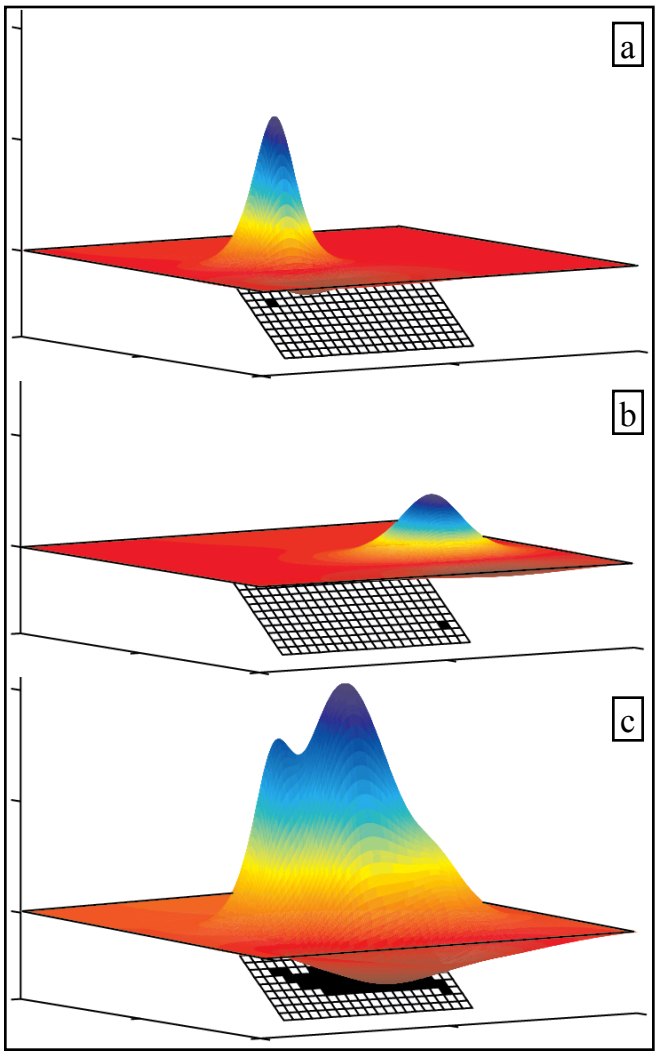

Figure 2.9: Forward models showing response of a free surface to slip on a dipping fault patch (black rectangles). a) Shallow slip, b) deep slip, c) distributed slip. Surface displacements are projected into a common InSAR line-of-sight. Surface motions are vertically exaggerated 500X.

expected interseismic motion along plate boundaries or deformation during large subduction zone earthquakes [e.g., *Fialko* 2006, *Fournier et al.* 2011].

2.2.2 Source Inversions

Observations of surface displacements from interferograms, GPS or other geodetic techniques can inform our understanding of the subsurface processes that produced the signal. In earthquake and aseismic fault slip studies, the goals are often to determine both the geometry and location of the responsible fault in addition to the distribution and magnitude of slip on the fault (Figure 2.9c). Fault slip inversions are important tools for learning about regional tectonics such as seismogenic depths, fault segmentation, and how earthquakes and aftershocks collocate. Slip distributions also allow researchers to drive sophisticated models of post-seismic stress change and fault interaction [e.g., *Freed and Lin,* 2001, *Hearn et al.,* 2002]. Burgeoning research is now working to incorporate slip distributions inverted from high-rate GPS displacements into earthquake early warning systems [e.g., *Bock et al.,* 2000, *Crowell et al.,* 2012].

Details of fault slip inversions are discussed in Chapter 3, but here I introduce the basic theory. The problem is treated as an inverse problem in which I relate finite displacement on a dislocation in a homogenous, elastic halfspace to displacements on a free surface [e.g., *Okada*, 1992; *Meade*, 2007]:

$$\mathbf{Gm=d} \qquad \text{eq. 2.5}$$

G is the Green's function (a [**P** x **S**] matrix) relating slip on a dislocation (also termed a patch), **m** (a [**S** x 1] vector), to displacements on a free surface, **d** (a [**P** x 1] vector)(Figure 2.9). Before inverting for slip, interferograms are spatially downsampled from ~10^6 to a computationally feasible ~10^2 data points [*Lohman and Simons,* 2005a] (Figure 2.10b). To solve for the spatial distribution of slip (the "slip distribution") that best fits the data, I take a two-part least squares approach that first solves for the geometry (centroid location, strike, dip) of a single fault patch using the Neighborhood Algorithm, a global optimization technique that efficiently searches multidimensional parameter spaces [*Sambridge*, 1999]. When the data require distributed slip, I fix the best-fit fault geometry from the Neighborhood Algorithm then use an iterative approach that generates a slip distribution where individual patches vary in size to reflect the resolution ability of the data (Figure 2.10) [*Barnhart and Lohman*, 2010, Chapter 3]. Slip direction (rake) in distributed slip inversions can be fixed (based on the Neighborhood Algorithm inversion, seismic focal mechanism, or other proxies) or allowed to vary from patch to patch. Spatially variable rake inversions are sometimes required by complexity in the data, such as during the 2010 Darfield, New Zealand strike-slip earthquake [*Barnhart et al.*, 2011, Chapter 4]. Variable rake inversions should be interpreted with caution, however, because of tradeoffs that can occur between slip on multiple faults. I use a single fault with distributed slip to characterize an

earthquake unless the data or independent observations require multiple faults. In the Darfield example, I explicitly define a four-segment fault geometry based on surface rupture observations and aftershock locations.

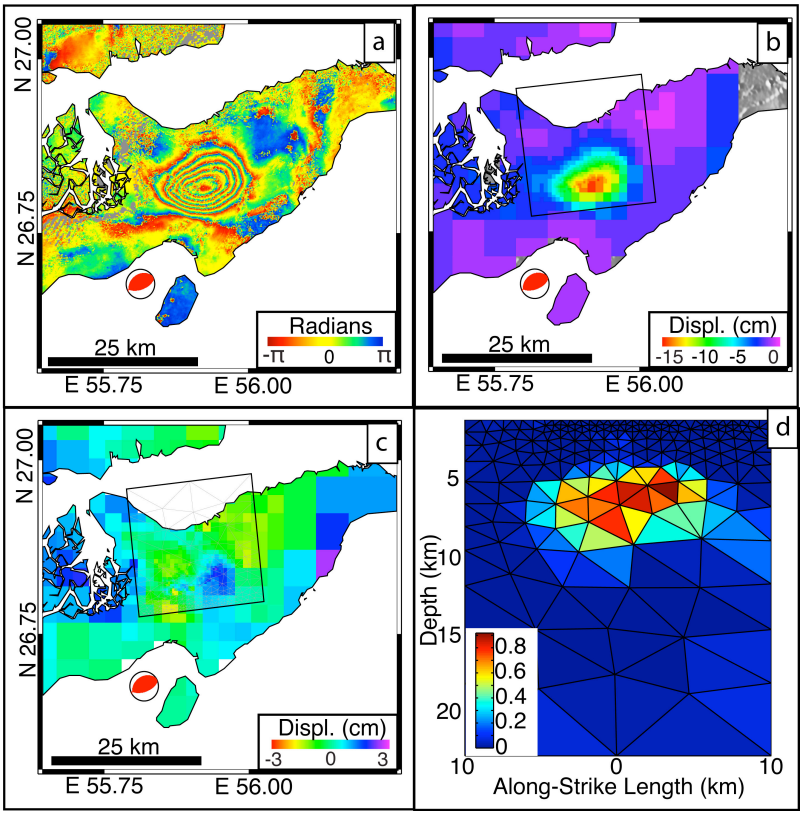

Figure 2.10: Example slip inversion for the 2005 Qeshm aseismic slip event (Chapter 6). A wrapped interogram is unwrapped (a) then downsampled (b). The best-fit fault centroid from the Neighborhood Algorithm is then variably discretized (c, d). c: Model residual with surface projection of discretized fault geometry, d: Slip distribution, viewed orthogonal to the fault plane.

2.2.3 Fault Slip Resolution

An essential consideration when analyzing co-seismic geodetic measurements is the choice of source type for modeling observed surface displacements. Substantial aseismic deformation can accompany an earthquake or earthquake swarm [e.g., *Johanson et al.*, 2006; *Lohman and McGuire*, 2007; *Barbot et al.*, 2009]. Geodetic observations (with the exception of high-rate GPS and strainmeters) are indifferent to whether the displacement source is seismic or aseismic. Because they measure the integrated ground displacements within a finite time period bounding an earthquake, geodetic observations include coseismic, postseismic, and aftershock deformation. By conflating aseismic and seismic fault slip sources, important information about modes of strain release is lost and impedes seismic hazard analysis and our understanding of

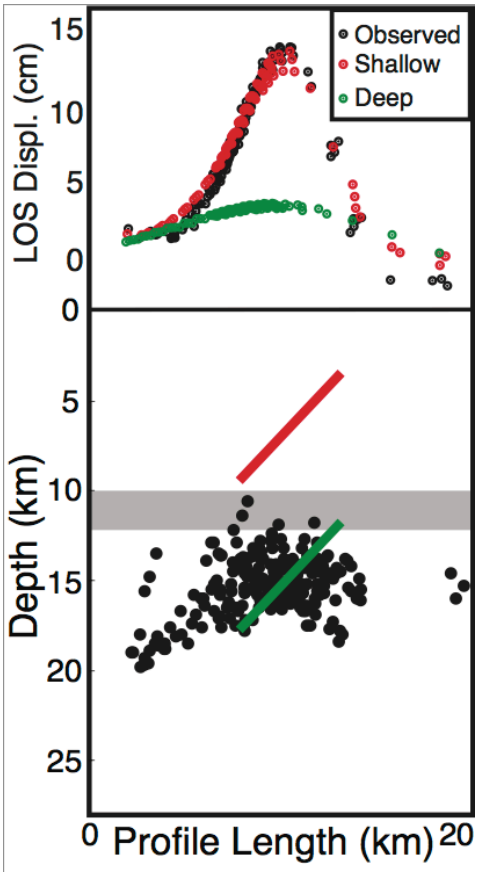

Figure 2.11: Comparison of observed surface displacements (black profile) to predicted surface displacements from a shallow (red) and deep (green) slip source of the same magnitude and orientation. The shape and magnitude of the surface motions constrain the depth of slip very well. This example is from the 2005 Qeshm earthquake (Chapter 6).

plate motion dynamics. It is critical to fully understand the source of observed deformation by integrating independent data sources and careful and thoughtful treatment of the data.

The resolution of slip distributions should always be considered when using inverse methods to learn about subsurface processes. We must address two aspects when considering the resolution of slip distributions (or any other inverse problem): the quantitative resolution of the inversion and the accuracy of the inversion with respect to the real Earth. The resolution of the inversion is dependent on the quality and spatial distribution of data with respect to the inferred fault plane. There are specific aspects of slip we can resolve very well with InSAR observations or reasonably dense GPS networks: the depth ranges and along-strike length extent of slip. In inverse problems with sufficient data, these two aspects are well-constrained (to within a kilometer) because they are directly related to the spatial characteristics of the surface displacement field (Figure 2.11). By comparison, teleseismic waveform inversions for earthquake location for moderate events ($<M_w6.5$) often exhibit errors as large as 50km in epicenter and ~10km in depth [e.g., *Maggi et al.*, 2000; *Lohman and Simons*, 2005b; *Engdahl et al.*, 2006; *Devlin et al.*, 2012, Chapter 7]. While the spatial resolution of geodetic slip inversions

is not perfect, it can be an order of magnitude better than teleseismic inversions. Of course, if the earthquake is too deep or not under land, then available geodetic measurements cannot constrain the earthquake.

In terms of the accuracy of the slip distribution, we must acknowledge that we have extremely limited information on the geometry of the fault plane beneath the surface, whether slip occurs on a single surface, a diffuse shear zone, or multiple planes/shear zones, and how the mechanical behavior of rocks, which vary in three-dimensions and in time, affect the observed surface displacements. Adding complexity, whether realistic or not, that is neither well-constrained nor required by the data to an inverse problem only serves to increase unquantifiable uncertainty to the slip distribution. While certain assumptions we make do not necessarily affect the quantitative resolution of the inverse problem, they play a significant role in how we interpret a slip distribution in a real tectonic setting and what attributes of the slip distribution we assign to real Earth behavior. As mentioned previously, inverting for slip with variable rake on a single fault may give an equivalent "best-fit" as slip on multiple faults. This particular scenario requires additional information from independent data sources. Furthermore, there are tradeoffs between the degree of complexity we allow in an inversion or forward model and computational feasibility. For example, it may be prudent to include vertical variations in rock behavior and complicated fault geometries in a study of long-term post-seismic deformation on a multi-cluster computer system, but the simplest assumptions are adequate to estimate the magnitude and location of an earthquake from GPS offsets on a home laptop.

We can quantitatively assess how specific assumptions (noise structure, elastic behavior, etc.) affect inversions. In cases where we have good constraints on the characteristics of the noise

(e.g., variance, spatial correlation), and when the inversion is linear, we can directly propagate data errors through the inversion. In scenarios where the inversion is non-linear, such as when we search for geometry or impose non-negative slip constraints, we use Monte Carlo methods to estimate the effects of data and model errors. The Monte Carlo approach I use produces populations of inversions that reflect the ensemble behavior of fault inversions due to noise. For instance, when investigating the effects of the wet delay on inferred fault geometry, I produce 1000 InSAR data sets that have similar noise statistics to the true data set [e.g., *Devlin et al.*, 2012]. I then invert each synthetic data set, generating a population of fault models where the spread in best-fit model parameters (e.g., location, depth, strike, dip, magnitude) is dependent on the characteristics of the noise. From this population, I can then extract meaningful statistics about the fault geometry that we can resolve given the noise (e.g., dip is $30^{o}\pm11^{o}$).

Another assumption often made for slip inversions is that the earth behaves as a homogeneous elastic halfspace. This assumption is common [e.g., *Segall and Harris,* 1986; *Jonsson et al.,* 2002; *Simons et al.,* 2011] because there is an analytical solution [*Okada,* 1992; *Meade,* 2007], because we have limited knowledge of the actual variations in elastic moduli in the subsurface, and because it is computationally efficient. We can assess the effects of this assumption by sampling reasonable ranges of rock rigidity using the Monte Carlo technique described above. One possible approach is to generate surface displacements in either a finite element model with complex subsurface properties or using analytical solutions for a layered-elastic space, then invert these data sets with a homogenous elastic halfspace model. The resulting variability will constrain how much bias is introduced by the assumption of elastic halfspace behavior in typical real-world scenarios. Previous work shows that lateral and depth-

dependent variations in rock rigidity have a small effect on first order characteristics (depth, orientation) but likely contaminate the details of slip distributions [e.g., *Savage,* 1987, *Hearn and Burgmann*, 2005].

In my work, I apply Monte Carlo methods in several ways. First, I explore the example described above for determining the sensitivity of the inferred fault geometry given data noise [*Devlin et al.*, 2012]. In Chapter 4, I apply this approach to constrain the effects of data noise on inferred static stress change between two faults [*Lohman and Barnhart*, 2010; *Barnhart et al.*, 2011]. I also apply the Monte Carlo approach to inversions for slip distributions to determine the bounds of moment magnitude that are allowable specific depth ranges [Chapter 6, *Barnhart and Lohman*, accepted]. Going forward, these Monte Carlo approaches will be used to understand the signals we observe in InSAR time series with the goal to discern between real ground displacements and atmospheric-induced signals [*Barnhart and Lohman*, in prep].

2.3 References

Barbot, S., Y. Fialko, and Y. Bock (2009), Postseismic deformation due to the Mw 6.0 2004 Parkfield earthquake: Stress-driven creep on a fault with spatially variable rate-and-state friction parameters, *J. Geophys. Res.*, *114*(B7), B07405, doi:10.1029/2008JB005748.

Barnhart, W. D., and R. B. Lohman (accepted), Phantom earthquakes and triggered aseismic creep: Vertical partitioning of strain during earthquake sequence in Iran, *Geophys. Res. Letts*.

Barnhart, W. D., and R. B. Lohman (2010), Automated fault model discretization for inversions for coseismic slip distributions, *J. Geophys. Res.*, *115*(B10), B10419, doi: 10.1029/2010JB007545.

Barnhart, W. D., M. J. Willis, R. B. Lohman, and A. K. Melkonian (2011), InSAR and Optical Constraints on Fault Slip during the 2010–2011 New Zealand Earthquake Sequence, *Seismological Research Letters*, *82*(6), 815–823, doi:10.1785/gssrl.82.6.815.

Berardino, P., G. Fornaro, R. Lanari, and E. Sansosti (2002), A new algorithm for surface deformation monitoring based on small baseline differential SAR interferograms, *IEEE*

Transactions on Geoscience and Remote Sensing, *40*(11), 2375 – 2383, doi:10.1109/TGRS.2002.803792.

Bevis, M., S. Businger, T. A. Herring, C. Rocken, R. A. Anthes, and R. H. Ware (1992), GPS meteorology: Remote sensing of atmospheric water vapor using the global positioning system, *J. Geophys. Res.*, *97*(D14), 15787–15,801, doi:10.1029/92JD01517.

Bock, Y., R. M. Nikolaidis, P. J. de Jonge, and M. Bevis (2000), Instantaneous geodetic positioning at medium distances with the Global Positioning System, *J. Geophys. Res.*, *105*(B12), 28223–28,253, doi:10.1029/2000JB900268.

Bürgmann, R., P. A. Rosen, and E. J. Fielding (2000), Synthetic Aperture Radar Interferometry to Measure Earth's Surface Topography and Its Deformation, *Annual Review of Earth and Planetary Sciences*, *28*(1), 169–209, doi:10.1146/annurev.earth.28.1.169.

Chen, C. W., and H. A. Zebker (2001), Two-dimensional phase unwrapping with use of statistical models for cost functions in nonlinear optimization, *J. Opt. Soc. Am. A*, *18*(2), 338–351, doi:10.1364/JOSAA.18.000338.

Crowell, B. W., Y. Bock, and D. Melgar (2012), Real-time inversion of GPS data for finite fault modeling and rapid hazard assessment, *Geophys. Res. Lett.*, *39*(9), L09305, doi:10.1029/2012GL051318.

Emardson, T. R., M. Simons, and F. H. Webb (2003), Neutral atmospheric delay in interferometric synthetic aperture radar applications: Statistical description and mitigation, *J. Geophys. Res.*, *108*(B5), 2231, doi:10.1029/2002JB001781.

Farr, T. G. et al. (2007), The shuttle radar topography mission, *Rev. Geophys.*, *45*(2), doi:10.1029/2005RG000183.

Ferretti, A., C. Prati, and F. Rocca (2001), Permanent scatterers in SAR interferometry, *IEEE Transactions on Geoscience and Remote Sensing*, *39*(1), 8 –20, doi:10.1109/36.898661.

Fialko, Y. (2006), Interseismic strain accumulation and the earthquake potential on the southern San Andreas fault system, *Nature*, *441*(7096), 968–971, doi:10.1038/nature04797.

Fournier, T., M. E. Pritchard, and N. Finnegan (2011), Accounting for Atmospheric Delays in InSAR Data in a Search for Long-Wavelength Deformation in South America, *IEEE Transactions on Geoscience and Remote Sensing*, *49*(10), 3856 –3867, doi:10.1109/TGRS.2011.2139217.

Freed, A. M., and J. Lin (2001), Delayed triggering of the 1999 Hector Mine earthquake by viscoelastic stress transfer, *Nature*, *411*(6834), 180–183, doi:10.1038/35075548.

Goldstein, R. M., H. A. Zebker, and C. L. Werner (1988), Satellite radar interferometry: Two-dimensional phase unwrapping, *Radio Sci.*, *23*(4), 713–720, doi:10.1029/RS023i004p00713.

Hearn, E. H., and R. Burgmann (2005), The effect of elastic layering on inversions of GPS data for coseismic slip and resulting stress changes: Strike-slip earthquakes, *Bulletin of the Seismological Society of America*, *95*(5), 1637–1653.

Hearn, E. H., R. Bürgmann, and R. E. Reilinger (2002), Dynamics of İzmit Earthquake Postseismic Deformation and Loading of the Düzce Earthquake Hypocenter, *Bulletin of the Seismological Society of America*, *92*(1), 172–193, doi:10.1785/0120000832.

Hooper, A., H. Zebker, P. Segall, and B. Kampes (2004), A new method for measuring deformation on volcanoes and other natural terrains using InSAR persistent scatterers, *Geophys. Res. Lett.*, *31*(23), L23611, doi:10.1029/2004GL021737.

Johanson, I. A., E. J. Fielding, F. Rolandone, and R. Bürgmann (2006), Coseismic and Postseismic Slip of the 2004 Parkfield Earthquake from Space-Geodetic Data, *Bulletin of the Seismological Society of America*, *96*(4B), S269–S282, doi:10.1785/0120050818.

Jónsson, S., H. Zebker, P. Segall, and F. Amelung (2002) Fault Slip Distribution of the 1999 M_w 7.1 Hector Mine, California, Earthquake, Estimated from Satellite Radar and GPS Measurements. *BSSA*, May 2002, v. 92, p. 1377-1389

Li, Z., J.-P. Muller, P. Cross, and E. J. Fielding (2005), Interferometric synthetic aperture radar (InSAR) atmospheric correction: GPS, Moderate Resolution Imaging Spectroradiometer (MODIS), and InSAR integration, *J. Geophys. Res.*, *110*(B3), B03410, doi:10.1029/2004JB003446.

Lohman, R. B., and W. D. Barnhart (2010), Evaluation of earthquake triggering during the 2005–2008 earthquake sequence on Qeshm Island, Iran, *J. Geophys. Res.*, *115*(B12), B12413, doi:10.1029/2010JB007710.

Lohman, R. B., and J. J. McGuire (2007), Earthquake swarms driven by aseismic creep in the Salton Trough, California, *J. Geophys. Res.*, *112*(B4), B04405, doi:10.1029/2006JB004596.

Lohman, R. B., and M. Simons (2005a), Some thoughts on the use of InSAR data to constrain models of surface deformation: Noise structure and data downsampling, *Geochem. Geophys. Geosyst.*, *6*(1), Q01007, doi:10.1029/2004GC000841.

Lohman, R. B., and M. Simons (2005b), Locations of selected small earthquakes in the Zagros mountains, *Geochem. Geophys. Geosyst.*, *6*(3), Q03001, doi:10.1029/2004GC000849.

Meade, B. J. (2007), Algorithms for the calculation of exact displacements, strains, and stresses for triangular dislocation elements in a uniform elastic half space, *Computers & Geosciences*, *33*(8), 1064–1075, doi:10.1016/j.cageo.2006.12.003.

Okada, Y. (1992), Internal Deformation Due to Shear and Tensile Faults in a Half-Space, *Bull. Seismol. Soc. Amer.*, *82*(2), 1018–1040.

Rosen, P. A., S. Hensley, G. Peltzer, and M. Simons (2004), Updated repeat orbit interferometry package released, *Eos Trans. AGU*, *85*(5), 47, doi:10.1029/2004EO050004.

Sambridge, M. (1999), Geophysical inversion with a neighbourhood algorithm—I. Searching a parameter space, *Geophysical Journal International*, *138*(2), 479–494, doi:10.1046/j.1365-246X.1999.00876.x.

Savage, J. C. (1987), Effect of crustal layering upon dislocation modeling, *J. Geophys. Res.*, *92* (B10), 10595–10,600, doi:10.1029/JB092iB10p10595.

Simons,M., S. E. Minson, A. Sladen, F. Ortega, J. Jiang, S. E. Owen, L. Meng, J-P. Ampuero, S. Wei, R. Chu, D. V. Helmberger, H. Kanamori, E. Hetland, A. W. Moore, and F. H. Webb (2011) The 2011 Magnitude 9.0 Tohoku-Oki earthquake: Mosaicking the megathrust from seconds to centures. *Science*, 322 (1421).

CHAPTER 3

AUTOMATED FAULT MODEL DISCRETIZATION[1]

3.1 Abstract

Geoscientists increasingly rely on co-seismic slip distributions inferred from geodetic observations to drive sophisticated models of the seismic cycle. To date, little work has been done on optimizing the parameterization of these fault models so that they reflect the resolving power of observed surface displacements. The locations of noisy surface displacement observations are often widely scattered far from features we wish to analyze in the subsurface and result in highly variable resolving power on the fault plane at depth. The few attempts to produce variably discretized fault planes [e.g. *Simons et al.* 2002, *Pritchard et al.* 2002] are generally done arduously by hand and may not correctly reflect the ability of the data to resolve slip features and magnitudes. Motivated by the increasing size of geodetic data pools and the need for distributed slip models that accurately represent features the data can resolve, we present a fully automated algorithm that iteratively adjusts the sizes of dislocations in a fault model. We use the concept of smoothing scales, derived from the model resolution matrix, to resize dislocations so that each dislocation is sized appropriately given the area over which slip in that region of the fault would be smoothed. We present a series of synthetic tests that utilize both sparse and dense data sets and compare our variably discretized inversions to traditional regularly discretized inversions. We also use our approach to invert for slip from geodetic observations of the 2004 M_w 6.0 Parkfield, California and the 1995 M_w 8.1 Antofagasta, Chile

[1] An edited version of this paper was published by AGU. Copyright 2010 American Geophysical Union. Barnhart,W.D., R.B. Lohman (2010), Automated fault model discretization for inversions for co-seismic slip distributions, J. Geophys. Res., 115, B10419.

earthquakes.

3.2 Introduction

Efforts to understand the modes of strain release across plate boundaries often require inference of subsurface processes such as fault slip, interseismic creep, and postseismic deformation, which are based on surface observations that are necessarily located far from the processes of interest. Geodetic data provided by Interferometric Synthetic Aperture Radar (InSAR) and GPS, which historically have had less than ideal spatial and temporal coverage, can nonetheless place strong constraints on geophysical models when the data are available. The current growth of the catalog of InSAR observations represents a substantial increase in our understanding of deformation throughout the seismic cycle, and the potential addition of NASA's Uninhabited Aerial Vehicle Synthetic Aperture Radar (UAVSAR), the Deformation, Ecosystem Structure and Dynamics of Ice (DESDynI), and ESA's Sentinel data pools in the next decade will produce further constraints on surface deformation throughout the earthquake cycle. These increases in data require efficient, accurate, and fully automated means for assimilating them into inversions for co-seismic slip and other fault slip processes.

Increasingly, co-seismic slip distributions are used to drive sophisticated simulations of the seismic cycle [e.g. *Freed and Lin*, 2001; *Freed et al.*, 2006] that model processes such as static stress changes and mantle viscoelastic responses. In many instances, the co-seismic slip distributions are inverted using fault planes that are discretized with evenly sized dislocations (fault patches in the model that may or may not slip) [e.g. *Johnson et al.*, 2001; *Funning et al.*, 2005; *Johanson et al.*, 2006]. This type of parameterization often leads to an inverse problem in which the distribution of dislocation sizes is not well suited to constrain details of the slip

distribution. In this situation, the inversion will reflect a slip distribution that is not optimally constrained by the data. Such distributions may mean we are modeling slip in too fine of detail in some parts of the fault plane and introducing slip features that the data cannot constrain. We also may be modeling slip in too broad of detail where the data can constrain much finer details [*Menke*, 2012]. In most cases, we encounter some combination of these issues depending on the location of dislocations in the fault model and the distribution and quality of data.

Here, we aim to produce fault discretizations that accurately reflect the resolving power of available data and do not map spurious slip features that are unconstrained by the data. Our goal is to generate a fault model in which slip on each dislocation is robustly constrained by the data such that dislocations are sized so that they are independent of their neighboring dislocations. Previous works [*Pritchard et al.*, 2002; *Simons et al.*, 2002; *Page et al.*, 2009] demonstrate different attempts at optimizing a slip model's resolution through use of a variably discretized fault. However, in many cases these fault models are arduously constructed manually with the final discretization not necessarily reflecting the full potential resolution of the model. We introduce two fully automated methods in which variably sized fault dislocations are iteratively generated with consideration for the resolving power of the data until we have a fault model that is well constrained by the data and is unlikely to contain misleading slip artifacts. Our method is similar to the data resampling technique developed by *Lohman and Simons* [2005] for reduction of large volumes of InSAR observations. We apply our methods to various synthetic tests then derive slip distributions from surface displacements recorded with various geodetic tools for the 2004 Mw 6.0 Parkfield, California, earthquake and the 1995 Mw 8.1 Antofagasta, Chile, earthquake. Both earthquakes are well documented in the scientific literature allowing us to

compare our results to previously published slip distributions.

3.3 Method

3.3.1 Slip Inversion and Model Resolution

Fault models discretized into equal area fault dislocations often lead to highly mixed determined inverse problems that do not accurately reflect the resolving ability of observed surface displacements [*Menke*, 2012]. Ideally, the discretization of a fault model for inversion of distributed slip would be driven by the locations and quality of data, which control the model resolution. Because spatial model resolution in fault slip inverse problems is reflected in the size of model dislocations, we desire a fault parameterization in which individual dislocations are sized to the dimensions over which slip can be accurately resolved at that location. For the methods we introduce here, we assume a fixed fault geometry. In a real scenario we would not necessarily know the correct fault geometry or slip direction (rake), but we can use nonlinear approaches such as the Neighborhood Algorithm [*Sambridge*, 1999] to first obtain a best fit fault geometry that we fix and discretize.

We begin by considering the inverse problem to be solved for distributed co-seismic slip:

$$Gm=d \qquad \text{(eq 3.1)}$$

where **G** is a matrix of Green's functions which relate slip on a dislocation at depth to displacements at a free surface, **m** is the source model which is the fault we ideally construct to reflect the resolution of the data and geology, and **d** are noisy geodetic observations, such as GPS displacements or interferogram observations. To derive Greens functions, we use field equations

that assume either a rectangular or triangular slipping dislocation within an isotropic elastic halfspace [*Okada*, 1992; *Meade*, 2007]. In cases where the fault geometry (potentially nonplanar) and rigidity structure in the region of the earthquake are well constrained, more complicated Green's functions can be utilized [*Du et al.*, 1997; *Zhao et al.*, 2004]. Interferograms are often resampled or spatially averaged for computational efficiency [e.g., *Jónsson et al.*, 2002; *Simons et al.*, 2002; *Lohman and Simons*, 2005]. We weight the data and Green's functions so that the weighted data have uniform, unit variance by premultiplying both sides of equation (1) by the inverse of the Cholesky factorization of the data covariance matrix [*Harris and Segall*, 1987].

While there are many methods for solving the inverse problem for **m** [e.g., *Parker*, 1977; *Menke*, 2012], we use higher order Tikhonov Regularization where our preferred model minimizes the norm of:

$$\min \left\| \begin{bmatrix} G \\ \lambda L \end{bmatrix} m - \begin{bmatrix} d \\ 0 \end{bmatrix} \right\| \qquad \text{(eq. 3.2)}$$

where **L** is a Laplacian smoothing matrix that penalizes steep gradients in slip between neighboring dislocations and λ is a regularization weighting parameter. To construct the Laplacian smoothing matrix for methods using triangular dislocations described later in sections 3.3.1 and 3.3.2 we first identify if the dislocation of interest is in contact with either two (a corner dislocation) or three (an internal or side dislocation) other dislocations. We assign a weight of λ to the dislocation of interest and equivalent values to each adjacent dislocation such that the sum of the weight of all the dislocations is 0. We do not weight each dislocation by its

area because we assume the area of adjacent dislocations is not significantly different since dislocation size should vary smoothly. We choose λ using the $_jR_i$ method [*Barnhart and Lohman*, 2010, Appendix A.1], an approach that balances the contribution from data noise (perturbation error) and oversmoothing (regularization error). Other popular techniques for choosing λ include identifying the corner of the L-curve [*Segall and Harris*, 1987], cross-validation [*Árnadóttir and Segall*, 1994; *Freymueller et al.*, 1994; *Cervelli et al.*, 2001; *Hreinsdóttir et al.*, 2003], and the Akaike Bayesian Information Criterion [*Akaike*, 1980; *Jackson and Matsu'ura*, 1985; *Ide et al.*, 1996]. The $_jR_i$ approach has the advantages of not requiring manual choice of a "corner", allowing nonlinear inversion approaches, and having low sensitivity to the knowledge of the exact character of the noise. The $_jR_i$ value associated with a set of smoothing values and fault parameterizations provides a metric for the quality of the inversion where a smaller $_jR_i$ value is associated with a more appropriate regularization and fault geometry. Therefore, the $_jR_i$ value can help us compare discretization choice (e.g., more or fewer dislocations) as well as l. Once an appropriate value for λ is chosen, we construct the generalized inverse:

$$G^{-g} = \left(\begin{bmatrix} G \\ \lambda L \end{bmatrix}^T * \begin{bmatrix} G \\ \lambda L \end{bmatrix} \right)^{-1} G^T \qquad \text{(eq. 3.3)}$$

Using equation (3), we can then calculate the model resolution matrix **R:**

$$R = G^{-g}G \qquad \text{(eq. 3.4)}$$

The model resolution matrix illustrates how well resolved each model parameter is given the data

kernel and a priori model inputs [*Menke*, 2012]. In cases where **m** is uniquely determined, **R** is an identity matrix. Otherwise, **R** reflects the relationship between the inverted model as a spatial averaging of the true model [*Menke*, 2012], such that:

$$m^{estimated} = Rm^{true} \qquad \text{(eq. 3.5)}$$

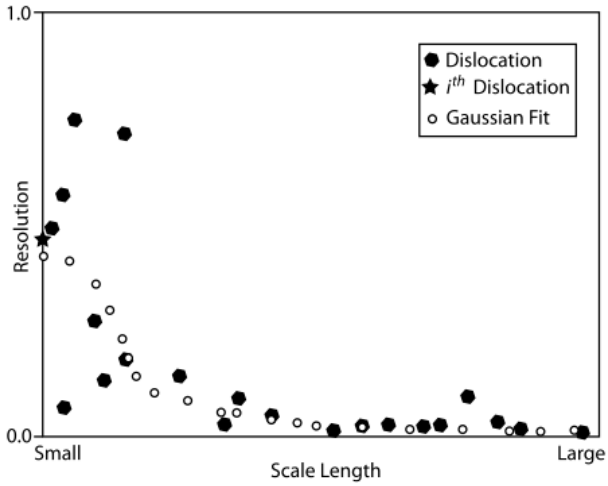

Figure 3.1: Illustration of Gaussian fit between scale length and resolution for the i^{th} dislocation in the i^{th} row of **R.** Actual values in i^{th} row of **R** are represented by black hexagons, i^{th} dislocation is represented by a black star, and Gaussian fit is represented by open circles. The characteristic height of the Gaussian curve will be the 1-σ smoothing scale of the i^{th} dislocation.

For co-seismic slip, one row of **R** demonstrates how unit slip is smoothed across other dislocations in the model [*Du et al.*, 1992]. In cases where a dislocation is very well resolved, slip on the row of **R** corresponding to that dislocation would appear as a delta function centered on the dislocation. When a dislocation is poorly resolved, inferred slip will be distributed onto neighboring dislocations. For a very poorly resolved dislocation, there may be significant contribution to slip on that dislocation from dislocations far away in the fault model. For example, large amounts of slip may be erroneously mapped to deep dislocations by the inversion when true co-seismic slip is physically concentrated in shallow regions of the rupture area.

In each of the examples described later, we apply positivity constraints to the inversion. This ensures that each inversion forces the same sense of slip given the rake we define, and it

makes each inversion nonlinear. Because we use positivity constraints, **R** may not be a perfect metric for model resolution, yet **R** still performs well and each inversion shown later is consistent in its assumptions of positivity.

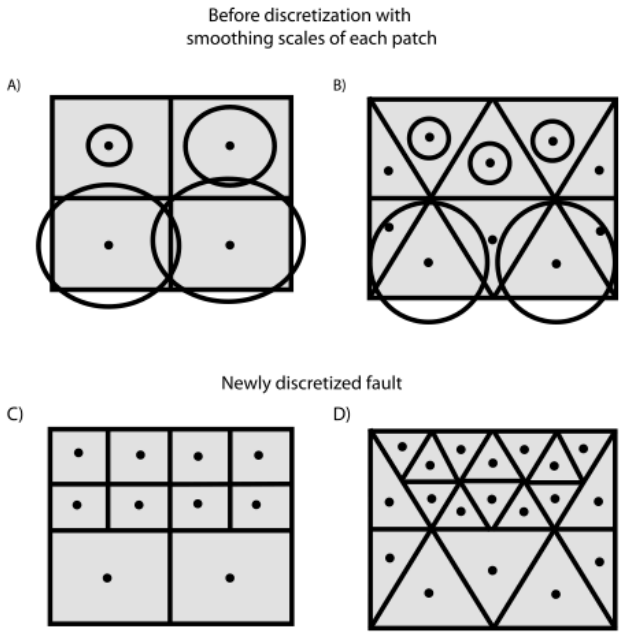

Figure 3.2: Schematic illustration of downsampling for rectangular and triangular dislocations. (a and b) The initial dislocation geometries with the centers of each dislocation marked (points) and the smoothing scale of each dislocation shown as a circle (some were not drawn for diagram clarity). (c and d) The newly discretized fault in which dislocations that were larger than their smoothing scale are downsampled and those that were smaller are left alone.

3.3.2 Model Construction

Using **R**, we can determine which dislocations are overdetermined or underdetermined and generate new distributions of dislocations that better reflect the resolving power of the data. We desire a fault discretization that minimizes the amount of slip smoothed onto neighboring dislocations. To do so, our dislocations must be the approximate size of the distance over which slip is smoothed.

To assess the resolution of a dislocation, we fit a Gaussian curve to the relationship between the i^{th} row of **R** associated with the ith dislocation and the distance to the center of all other dislocations (Figure 3.1). Other line-fitting methods may be used, for example, *Biggs et al.* [2006]fit a negative exponential to the relationship of RMS data misfit to model roughness to determine an appropriate smoothing weight. The width of the Gaussian, which we designate as the smoothing scale, is the characteristic distance over which the slip from the dislocation of interest is smoothed across surrounding dislocations and represents the 1-σ smoothing distance. If

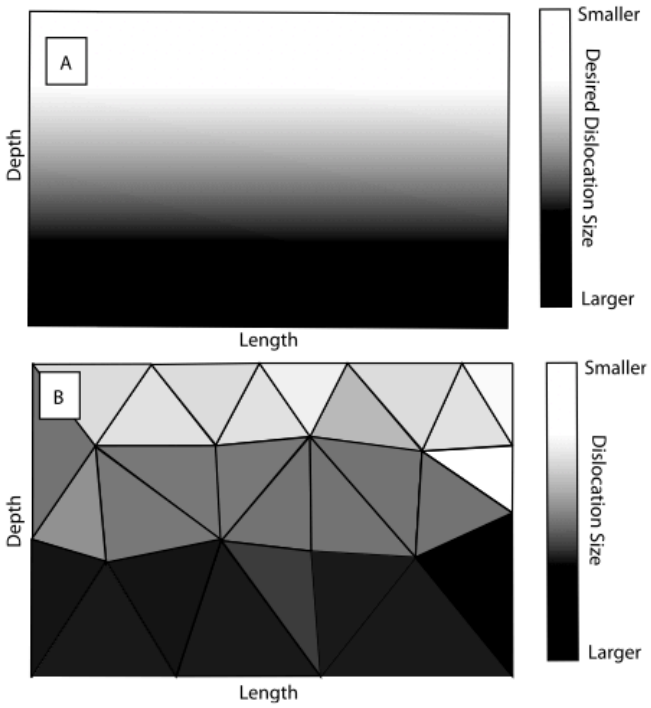

Figure 3.3: Illustration of complete mesh resampling through use of a size function. (a) Desired size distribution of disloca- tions across a fault model with smallest dislocations near the surface and largest dislocations at depth. (b) Rediscretized fault plane meshed according to the size function with triangles sized such that they approximate the desired size function.

the smoothing scale is either much larger or much smaller than the actual dimensions of the dislocation, then we claim the dislocation is incorrectly resolved. If the smoothing scale is on the order of the dislocation dimensions, then the dislocation is likely sized appropriately. Once we generate a new smoothing scale for each dislocation in the model, we then adjust the dislocation distribution by means of either downsampling or complete mesh resampling.

3.3.3 Downsampling

The simplest form of constructing optimally parameterized fault models is by downsampling a coarsely discretized model (Figure 3.2). In order to downsample dislocations, we start with a user-selected initial distribution of dislocations. Following the algorithm described above, we derive smoothing scales for each dislocation and compare the smoothing scale of each dislocation with the dislocations actual size. If a dislocation is larger than its smoothing scale, we claim the dislocation is overresolved and downsample it. For rectangular dislocations, we divide each dislocation equally into four smaller rectangles (quadtree approach, Figures 3.2a and 3.2b). For triangles, we downsample a single dislocation into four smaller triangles by allowing the midpoint of each side of the triangle to become a vertex for the four new triangles (Figures 3.2c and 3.2d). If the dislocation is smaller

than its smoothing scale, we claim the dislocation is adequately well resolved and retain its current size. We then iterate until all dislocations are smaller than their smoothing scales.

Downsampling of dislocations proves to be a simpler process than complete mesh resampling (described in section 3.3.4); however, there are many aspects of downsampling dislocation models that are unfavorable. First, dislocations can only be divided equally into four smaller dislocations one way, so our final model is highly dependent on the initial coarse model parameterization. Equal division into four smaller units requires a factor of two size change that imposes potentially undesirably steep gradients in dislocation size. Also, since dislocations cannot become larger in our algorithm and if our initial mesh is too fine some dislocations far from data points may remain poorly resolved following complete downsampling and inhibit the robustness of the inversion.

3.3.4 Complete Model Resampling

Whereas downsampling is restricted by the initial model input, a method for resampling the fault after each iteration according to a size function behaves independent of the initial inputs and allows for a model parameterization that more accurately reflects the model resolution. Various meshing algorithms developed for use in finite element models are excellent tools for deriving such distributions with variable dislocation size.

We begin by generating estimates of smoothing scales on a coarse, uniformly discretized triangular mesh over the target fault plane. To mesh the fault plane into triangles, we use the unstructured finite element meshing routine MESH2D developed by Engwirda [2005] which takes as inputs the overall fault plane geometry (length and width) and the desired dislocation sizes as a function of location on that fault plane (Figure 3.3a) after one iteration. We set the new

smoothing scales as the desired size distribution. Instead of downsampling each dislocation individually, the MESH2D algorithm produces a fully resampled field of dislocations sized according to the size function and constrained by the geometric bounds of the fault plane (Figure 3.3b).

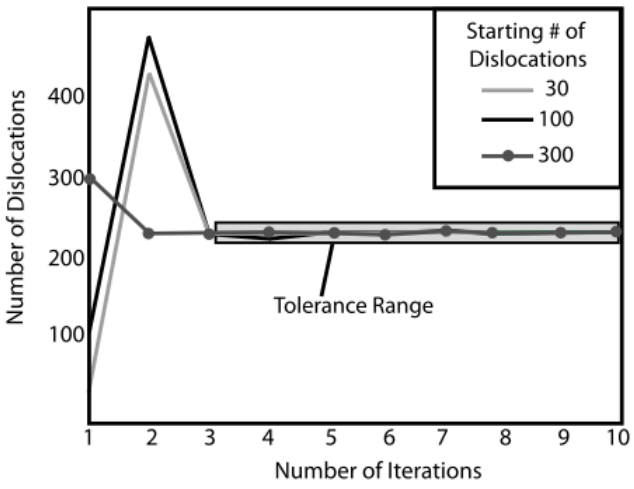

Figure 3.4: Example of criterion for termination of complete mesh resampling algorithm. Each line reflects a different starting number of dislocations and reflects the number of dislocations remaining after each iteration. Eventually, the number of dislocations stabilizes, allowing a termination tolerance range to be picked (boxed).

As with the down sampling method, we iterate over the regularization and resampling process for each realization of the model. Because triangular dislocations can both grow and shrink via unstructured meshing, we cannot simply terminate resampling when all patches are smaller than their smoothing scales as is done in section 3.3.3. While meshing routines can take a desired size function as an input, there may always be dislocations that are sized inappropriately due to the geometric restrictions of triangles or because the Gaussian poorly fits a few points. We thus need to derive a resampling termination criterion that minimizes user bias introduced by manually terminating iterations. If we allow the algorithm to iterate over the same noisy data set many times, we find that the number of dislocations generated after each iteration stabilizes and each subsequent iteration produces only a slightly different number of dislocations. We define a tolerance criterion as some desired percent difference in total dislocation number (Figure 3.4). If the number of new dislocations after a single iteration is within the tolerance of the previous iteration, the algorithm is terminated. If not, we iterate over the algorithm again. Tests of various initial input models with the same geometry and noisy data set, but with different initial

discretizations, produce the same final stable set of dislocations. This demonstrates that the unstructured mesh resampling method is not dependent on the initial manually parameterized input model unlike the downsampling approach discussed in section 3.3.3.

An important factor to consider in using finite element meshing programs is the criterion used to assess the quality of individual triangular elements. In finite element models, it is usually advantageous to have triangular elements as close to equilateral as possible since solving routines are often evaluated at the vertices of each triangle. Meshing routines will generally have specific criteria for eliminating triangles that exceed some shape quality constraint. This effectively prevents steep spatial gradients in the element sizes used in the mesh. Because we are concerned with the size of each dislocation, not the shape, and spatial resolution of the model may change abruptly depending on data type, we allow the meshing routine to construct triangular meshes with large size gradients so as to avoid artifacts in model resolution caused by the meshing routine itself.

For the following examples, we will use the resampling algorithm with triangles. Triangular dislocations prove to be more versatile than rectangles in meshing complicated surfaces such as undulating subduction interfaces or complex fault networks. Triangles also allow smoothly varying size distributions of dislocations that are easier to regularize. Rectangular dislocations are more difficult to adapt without gaps to these complex geometries without creating strain singularities at dislocation edges [e.g., Meade, 2007]. This extreme restriction imposed by rectangular dislocations leads us to favor methods that parameterize fault planes using triangular dislocations. The algorithm source code and relevant updates are available on www.roipac.org.

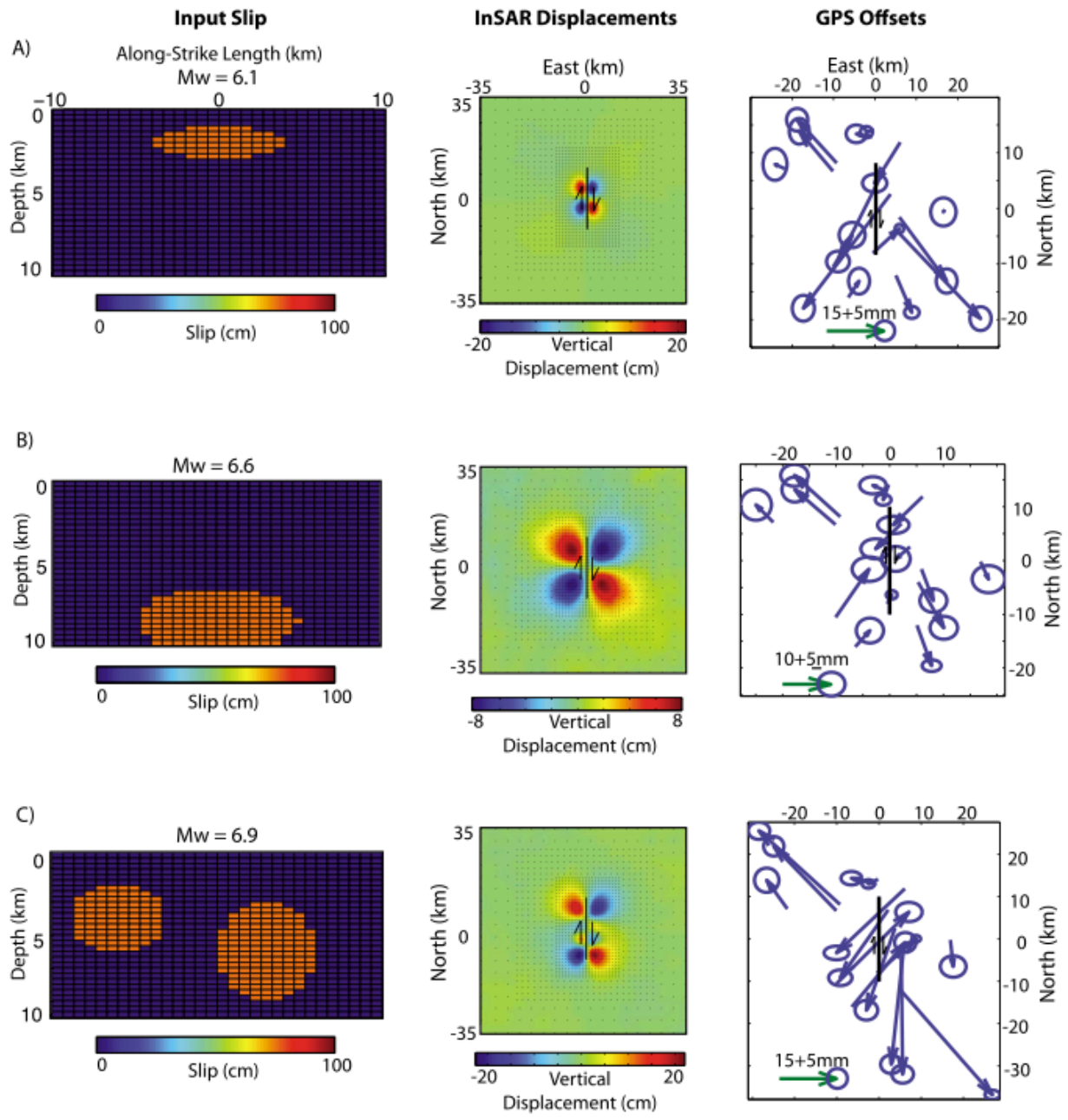

Figure 3.5: Results of synthetic tests. (Left) Synthetic, imposed input slip distributions. (middle) Noisy synthetic interferograms. Dots indicate locations of data points. (right) GPS offsets. Top row: (a) Shallow slip test. Middle row: (b) Deep slip test. Bottom row: (c) Slip asperity tests. Fault trace and sense of offset are shown in black, and GPS errors are shown as ellipses. Mw is the synthetic seismic moment for each slip distribution.

3.4 Synthetic Tests

3.4.1 Setup

We wish to demonstrate the ability of our resampling technique to optimally parameterize a fault model for inversion of co-seismic slip on a simple fault plane. We also wish to illustrate the

sensitivity of the resampling routine to data locations and noise. A common approach in assessing the ability of an inversion technique to robustly constrain an unknown model is to invert synthetic noisy data sets where the input slip solution is prescribed. We use the following three synthetic tests: (1) a single region of shallow slip, (2) a single region of deep slip, and (3) two slip asperities (Figure 3.5).

Each synthetic test is designed to demonstrate the ability of our fault discretizing algorithm to derive a fault parameterization that can resolve details related to the spatial distribution and magnitude of slip. In the shallow slip test, we will be able to demonstrate that our method can accurately resolve the maximum depth of slip and slip magnitude when slip is located in very well resolved regions, such as those close to data locations. In turn, the deep slip synthetic test will demonstrate that our algorithm will not infer fine details in slip where such details are not well resolved by the data. Lastly, the slip asperities test will illustrate the ability of our algorithm to distinguish between distinct slip regions where model resolution is good, as well as model the extent and magnitude of slip in each region. To demonstrate the dependence of dislocation sizes on data distribution, we also compare results using dense gridded data sets analogous to InSAR observations, and sparse, unevenly spaced data sets analogous to GPS.

Figure 3.5 shows the three synthetic slip distributions and the noisy data. We use a 20 × 10 km vertical strike-slip fault with purely right lateral strike-slip motion. The fault is initially partitioned into a grid of 30 × 30 rectangular dislocations (Figure 3.5). Green's functions are calculated for each geometry and noise-free data are generated. For the sparse data set (GPS analogue), we add random noise with 1 cm variance at the 15 stations and only use the horizontal components of displacements. We model the dense data set as InSAR observations and add

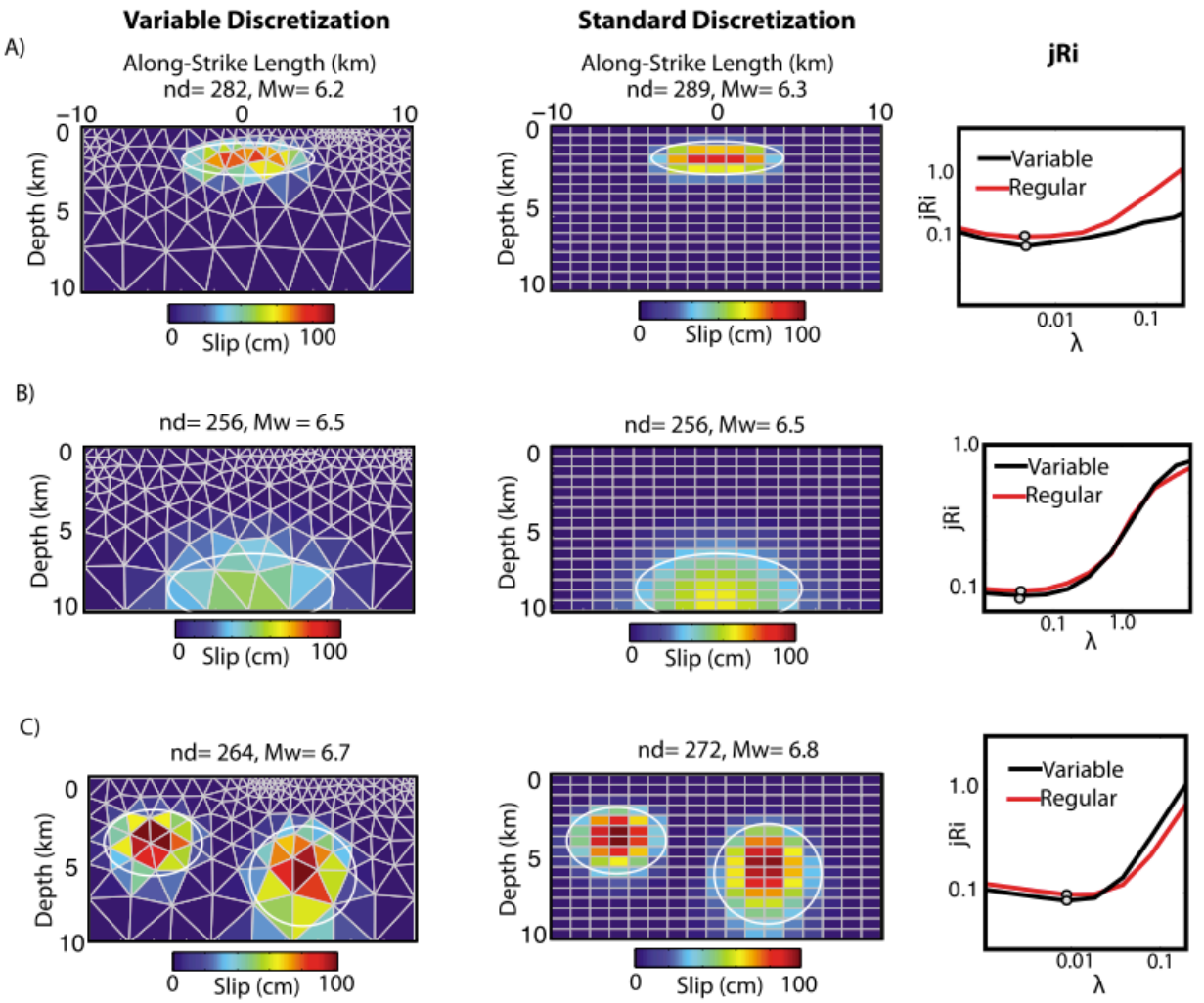

Figure 3.6: Results of using complete mesh resampling discretization technique applied to sparse (GPS) data sets. (left) Variably discretized plane with inverted slip. (middle) Regularly discretized plane with inverted slip. (right) A comparison of the $_{j}\boldsymbol{R_i}$ curves for each inversion. Points on $_{j}\boldsymbol{R_i}$ curves are the l value and corresponding $_{j}\boldsymbol{R_i}$ value used to weight the smoothing of each inversion shown. Inversions with a smaller $_{j}\boldsymbol{R_i}$ value are considered to be better. Variably discretized $_{j}\boldsymbol{R_i}$ curve is black, regularly gridded $_{j}\boldsymbol{R_i}$ curve is red, nd is number of dislocations in each model, and Mw is calculated seismic moment for each slip distribution. (a) Shallow test. (b) Deep test. (c) Slip asperities test. White circles show extent of synthetic input slip models shown in Figure 3.5. All inversions are shown with the same color scale as in Figure 3.5.

spatially correlated noise with 1-cm variance on a spatial scale of 20 km and project deformation into a vertical line of sight. We create a synthetic resampled interferogram with more data points located close to the fault than far from the fault as would be the case if we used the data resampling technique of Lohman and Simons [2005] (Figure 3.5, middle column). For simplicity, we do not include a ramp, which is typically used to model the effects of satellite orbital errors or

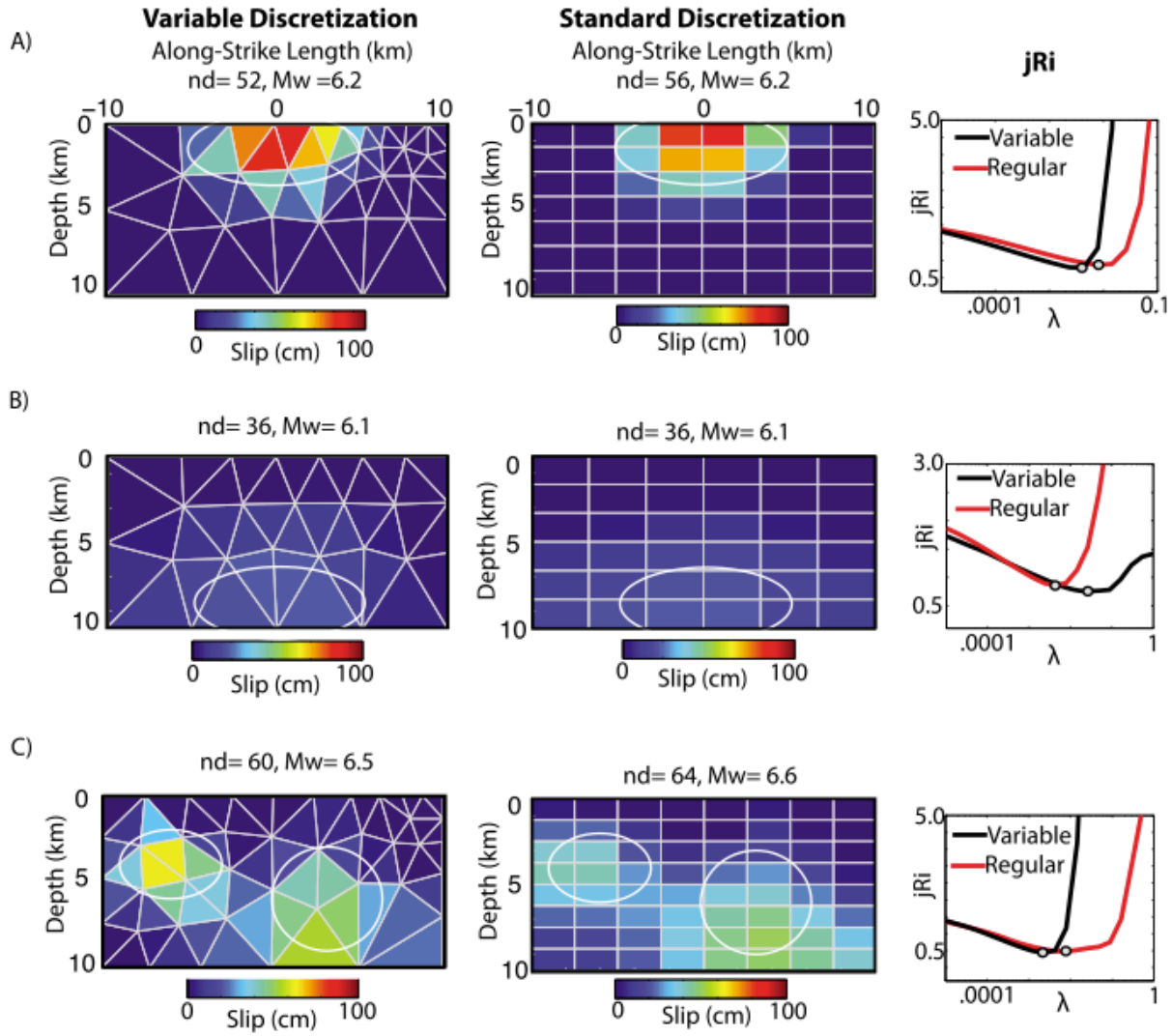

Figure 3.7: Results of using complete mesh resampling discretization technique applied to dense (InSAR) data sets. (left) Variably discretized plane with inverted slip. (middle) Regularly discretized plane with inverted slip. (right) A comparison of the $_jR_i$ curves for each inversion. Notice differences in slip magnitudes. Points on $_jR_i$ curves are the l value and corresponding $_jR_i$ value used to weight the smoothing of each inver- sion shown. Inversions with a smaller $_jR_i$ value are considered to be better. Variably discretized $_jR_i$ curve is black, regularly gridded $_jR_i$ curve is red, nd is number of dislocations in each model, and Mw is the seismic moment of each slip distribution. (a) Shallow test. (b) Deep test. (c) Slip asperities test. White circles show extent of synthetic input slip models shown in Figure 3.5. All inversions are shown with the same color scale as in Figure 3.5.

long-scale atmospheric noise [*Hanssen*, 2001] in any of the synthetic examples. To invert each noisy data set for distributed slip, we discretize the fault model using the complete mesh resampling technique with triangles discussed in section 3.3.4. We use the same fault geometry and slip direction used to derive the synthetic data, though as mentioned before, these parameters

could first be solved using a nonlinear inversion in a real-world scenario where the fault geometry is not known.

3.4.2 Synthetic Inversion Results

Figure 3.6 shows the results of discretizing and inverting the sparse (GPS) data set while Figure 3.7 shows the results of using the dense (InSAR) data set. The GPS examples demonstrate better resolution despite sparse data locations than the InSAR inversions. This is related to the SAR line-of-sight constraining a limited component of the displacement field. We also show inversions of the same data sets onto fault planes of the same geometry discretized into regularly gridded rectangular dislocations and compare the $_jR_i$ values of each inversion. We discretize the regularly gridded faults with a number of dislocations similar to that derived from the variable fault discretizer in each case. In each example, the $_jR_i$ value corresponding to the picked smoothing value (l) for the variably discretized fault is better (i.e., lower) than for the regularly gridded fault, suggesting that our variably discretized fault allows for an inversion that better balances the errors due to oversmoothing and from data noise. We are able to recover the moment of the input slip model in each of the inversions onto variably and evenly discretized grids.

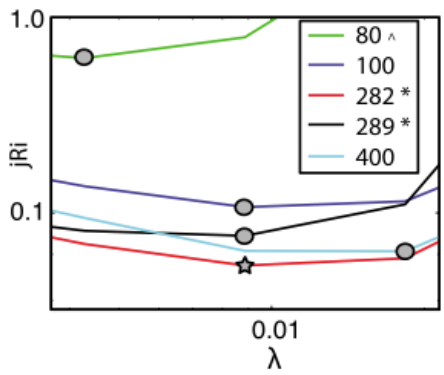

Figure 3.8: The $_jR_i$ curves for inversions of InSAR-based test data onto variously discretizated planes (the numbers in the legend are the number of dislocations used). Curves with circles are derived from evenly discretized rectangular dislocations. The curve with a star is variably discretized. Asterisk indicates that inversions are shown in Figure 3.7a.

The greatest discrepancies between dislocation sizes between the variably and regularly discretized models occur in the dense (InSAR) examples (Figure 3.7). In each InSAR example, both the variably and regularly discretized fault models predict similar areas of fault slip. This is, perhaps, not surprising because in these examples, the dislocation sizes in the vicinity of fault

slip are fairly similar. However, the differences in dislocation size with depth, particularly in the GPS-like slip asperities example (Figure 3.6c), allows the variably discretized planes to more accurately resolve details in the spatial extent of slip. Additionally, the variable discretizations concentrate the output resolution in the regions of the fault plane that are best resolved, resulting in good constraints on the region that did not slip: a characteristic that is often of great interest to geophysicists. In each of the GPS-based variable discretizations, we observe an interesting trend along strike in which greater numbers of shallow dislocations are present in regions where near-fault surface offsets are greatest. This is particularly apparent in the shallow slip and slip asperities tests (Figures 3.6a and 3.6c), where two regions of denser fault dislocations are formed along strike where separate lobes of surface deformation exist. While slip is concentrated in the downdip center of the fault, high concentrations of shallow small dislocations are present at the end of the fault. In the sparse deep test (Figure 3.6b), the much sparser nature of the data and small displacements lead to a discretization where there is very little variability in dislocation size. This may initially seem surprising, since our fault discretization is based on the model resolution matrix, **R**. As Menke [2012] points out, **R** only reflects the data kernel and a priori knowledge of the model, such as geometry and number of dislocations. **R** does not have knowledge of the data magnitude. However, considering equations (3) and (4), the generalized inverse $\mathbf{G}^{-g}$ is regularized by l, which is chosen with the ${}_j\boldsymbol{R}_i$ technique. ${}_j\boldsymbol{R}_i$ does utilize the magnitude (more specifically, the signal-to-noise ratio) of the data. Thus, there is a consideration for the data magnitudes in **R** inherited through our choice of regularization. This inheritance is reflected in the greater numbers of dislocations located where data offsets and signal-to-noise ratios are largest.

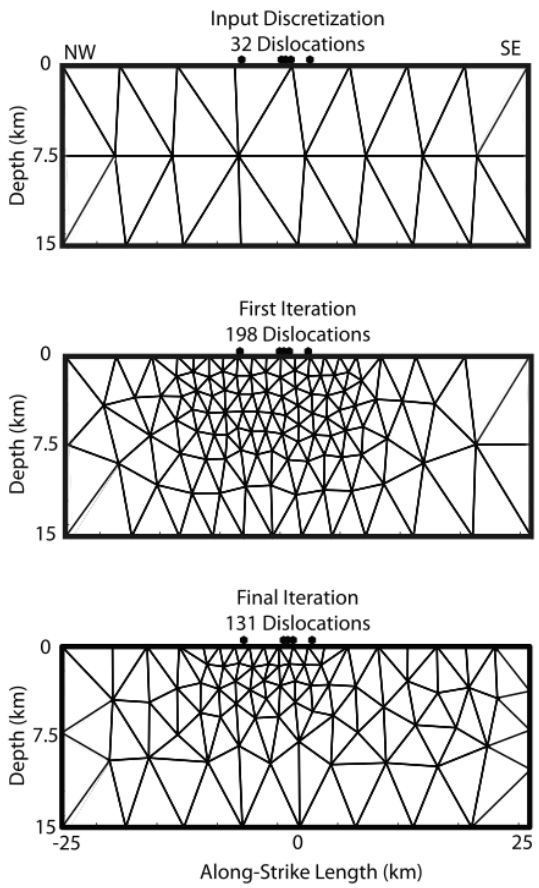

Figure 3.9: Dislocation geometry for the three iterations necessary to discretize the Parkfield fault model. The final iteration is the fault parameterization used for the distributed slip inversion shown in Figure 3.10. Dots at the fault surface show the locations of the five GPS stations located closest to the surface trace of the fault model.

In each of the synthetic examples, we have inverted slip onto a fault evenly discretized with a number of dislocations analogous to the total number of dislocations derived using the variable meshing routine. In this case, the number of dislocations derived through variable meshing reflects the optimal number of dislocations given the model resolution. By inverting onto an evenly discretized fault with essentially the same number of dislocations as the variable model, we are using the "optimally evenly discretized" fault model; thus, we would not expect large differences in the slip distribution, $_jR_i$ value, or data misfit. This assertion is consistent with what we observe in Figures 3.6 and 3.7, where in the vicinity of regions of fault slip, the dislocation sizes are similar.

However, in a real scenario, we would not necessarily know a priori what the optimal number of dislocations would be for an evenly discretized model. Figure 3.8 demonstrates tests using the InSAR-like data in which we compare the optimized fault discretization and inversion for the shallow slip test (Figure 3.7a) with inversions onto evenly discretized fault models with greater and fewer dislocations than the optimal model. The $_jR_i$ values (Figure 3.8) demonstrate that our variable fault model produces the lowest $_jR_i$ value and remains the best model of those tested. As

we progressively increase or decrease the number of evenly discretized dislocations for the optimal number, the $_jR_i$ values become higher.

3.5 Real Data Inversions

In the previous section, we demonstrated how the complete mesh resampling technique is highly dependent on both data distributions and signal-to-noise ratios. The synthetic examples provided good evidence that our algorithm is able to automatically discretize a known fault geometry that optimally reflects the model resolution and prevents the mapping of spurious slip into inverted slip distributions. We also show that in each example, our discretizing method produces the lowest $_jR_i$ value, reflecting an overall better inversion. Here, we apply our complete mesh resampling method from section 3.3.4 to two earthquakes that are very different in both tectonic character and data type used.

3.5.1 The 2004 Parkfield Strike-Slip Event

The Mw 6.0 Parkfield Earthquake occurred on 28 September 2004, a delay of nearly 8 years from the prediction of the Parkfield Earthquake Prediction Experiment [*Bakun and Lindh*, 1985; *Bakun et al.*, 2005; *Langbein et al.*, 2005]. Numerous studies have inverted slip distributions based on various geodetic data sets for both co-seismic and postseismic slip [*Johanson et al.*, 2006; *Langbein et al.*, 2006; *Murray and Langbein*, 2006; *Page et al.*, 2009]. Geodetic inversions of co-seismic slip generally agree that the majority of slip occurred to the northwest of the initial rupture centroid [Johanson et al., 2006; Murray and Langbein, 2006] between depths of 2 and 14 kilometers. The magnitude of peak slip in these inversions varies from ~300 mm to 450 mm. The inversion by Johanson et al. [2006] using only GPS data suggest slip occurred in two asperities separated by a co-seismic gap. The first asperity, which slipped in

the region of rupture initiation, is deeper and of lower-magnitude slip than the second asperity located further north along strike. In a joint geodetic inversion, Johanson et al. [2006] show similar locations and magnitudes of slip concentrations, but with a saddle between asperaties and not a gap. Murray and Langbein do not suggest that such a separation of slip occurred; however, whereas Johanson et al. [2006] included more spatially dense interferograms in their inversion, Murray and Langbein used sparser laser ranging surveys in addition to GPS. The difference in data density may lead to the variability in the spatial resolution of slip.

3.5.1.1 Data and Model Parameters

We use a 21-station network composed of 16 campaign stations and five continuous stations (Figure 3.10b). For a complete description of the origin and time series modeling of this data set, see Johanson et al. [2006]. The continuous GPS stations represent a 2 year time series beginning January 2003 and ending January 2005, approximately three months after the earthquake. The campaign stations were surveyed at sparser time intervals, but in each case Johanson et al. [2006] remove the effects of postseismic deformation. Because they attempt to remove postseismic deformation related to both the 2004 Parkfield events and the 2003 San Simeon and Parkfield earthquakes, as well as the effects of interseismic loading, we do not attempt to model these processes in our inversion. We omit GPS station CARH because, as noted by Johanson et al. [2006], it lies between the two slipping strands of the San Andreas and experienced unknown postseismic deformation. Although geologic field evidence supports the existence of two parallel strands of the San Andreas Fault in the Parkfield area, we restrict our model to a single fault plane 50 × 15 km that strikes 140°, dips 87°, and ruptures the surface. We reduce by half the number of potential free parameters in the inversion by fixing the slip

direction to purely right lateral strike-slip motion (rake=180°). The vertices of the fault are pinned to 35.75°N, 120.3°W and 36.1025°N, 120.6449°W. As Johanson et al. [2006] describe, modeling the Parkfield rupture on a single plane is reasonable because the potential slipping strands are close enough to each other that the effects of using one plane will only be evident in the top 1–2 km of the slip inversion.

3.5.1.2 Inversion Results

Using the complete mesh resampling algorithm described in section 3.3.4, we converge to an appropriate fault discretization with triangular dislocations after three iterations. Figure 3.9 shows the number of dislocations generated during each iteration. During the rediscretization of our initial model, the number of dislocations initially increases by a factor of six, with the highest density of dislocations located in a region where five GPS stations are positioned close to the trace of the fault (marked as hexagons at the surface of the fault). We observe a large increase in dislocation number during the first iteration because the initial coarse input discretization is unable to adequately characterize the model resolution. There are simply not enough dislocations to allow for a model resolution matrix that contains smooth gradients across neighboring patches that can be fit well by a Gaussian relationship. The algorithm then reduces the number of dislocations to 131 which would not be possible through downsampling. Our final discretization is again dominated by a large density of smaller patches near the five GPS locations located nearest the fault. This represents the region of greatest model resolution in our inversion. From this portion of the fault, the area of dislocations increases both downdip and along strike where GPS stations are located farther from the trace of the fault model. In general though, the final fault discretization demonstrates highly variable dislocation sizes with steep gradients in size that

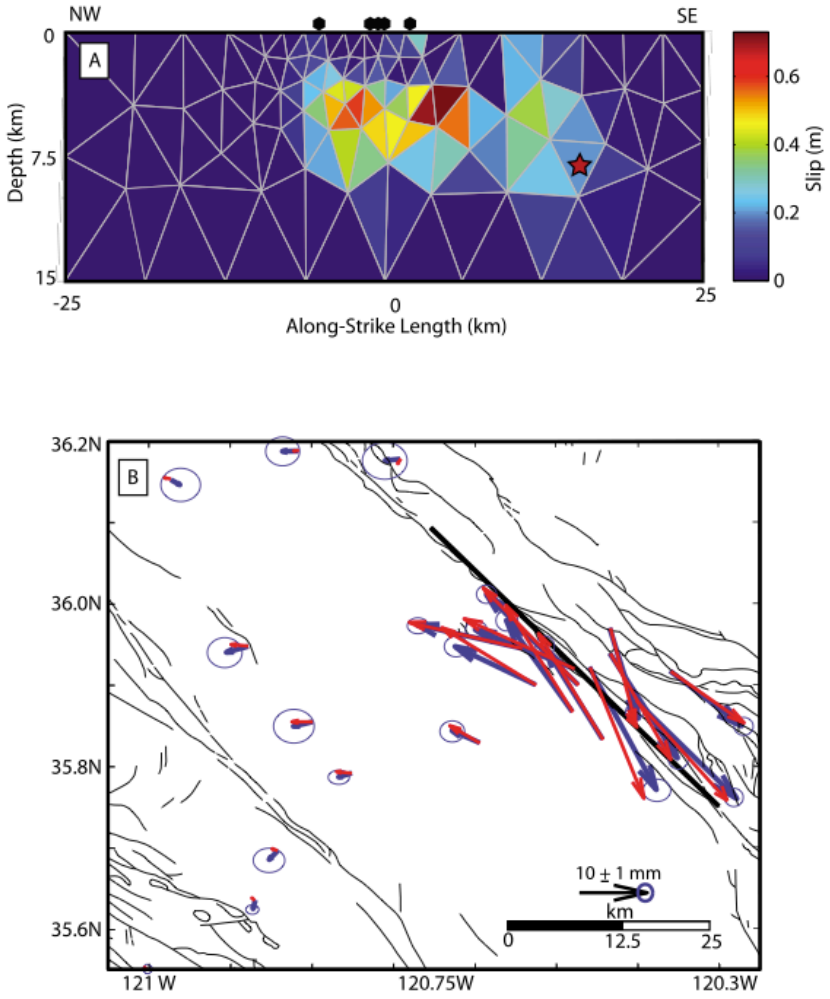

Figure 3.10: (a) Inferred slip distribution for the Parkfield earthquake. Star is location of the Harvard centroid moment tensor located hypocenter. Hexagons are the locations of the five GPS stations located closest to the surface trace of the fault model. (b) Observed (blue) and predicted (red) data using the slip distribution in (a). All velocities are relative to station ORES [Johanson et al., 2006]. Trace of the fault model marked by thick black line. Thin black lines are local mapped Holocene faults [Ludington et al., 2005].

are dominated by data located close to the surface trace of the fault model.

The results of our distributed slip inversion are shown in Figure 3.10a. As do previously derived slip models, our model demonstrates that the majority of slip occurred north along strike of the initial rupture point (starred). We infer maximum slip values of ~730 mm and a geodetic moment of 1.7×10^{18} Nm, or a moment magnitude (Mw) of 6.1 using a shear modulus of 34 GPa. The deepest slip is well constrained to a depth of ~10 km. We are also able to constrain some surface rupture well although the majority of slip is restricted to a minimum depth of ~2.5 km. Two principal slip asperities are apparent: a region in the southeast with relatively low slip magnitude and a region in the northwest with relatively high slip magnitude. The southeastern

asperity is located in the region of initial rupture, much like that of the region modeled by *Johanson et al.* [2006]. Unlike *Johanson et al.*'s [2006] inversion of GPS only, the asperity we model is much shallower and located almost entirely updip and north along strike relative to the initial rupture point. Our model also does not demonstrate a well-resolved gap between the southeastern and northwestern asperities. Instead, we model a saddle of decreased slip (~50–200 mm) that joins the two main asperities which is more similar to *Johanson et al.* [2006] joint geodetic inversion. It should be pointed out that dislocations in this region of the fault model are larger than the width of the gap found in the model by *Johanson et al.* [2006] that uses GPS data alone. Accordingly, there may be a physical slip gap in this region that this data set is unable to resolve. We may instead observe the effects of smoothing a small region of physical slip onto larger dislocations that can be resolved by the data. The slip inversion shown fits the observed data well (Figure 3.10b). To assess the quality of our GPS-only inversions, we apply the $_jR_i$ criterion to our GPS-only slip model and one similar to that used by *Johanson et al.* [2006]. Using the fault geometry [*I. A. Johanson, personal communication,* 2010], regular fault discretization, and data distribution employed by *Johanson et al.* [2006], we invert for distributed slip using Laplacian smoothing. We fix the regularization factor λ so that we are able to obtain a close match to the GPS-only derived model shown by *Johanson et al.* [2006] and compare the $_jR_i$ value associated with this and our best fit inversion using a variably discretized fault (the slip distributions and $_jR_i$ results are shown in the auxiliary material). Through this approach, we find that our resampling technique generates a lower $_jR_i$ value, even though we use a smaller overall number of dislocations.

Our GPS-only inversion agrees well spatially with the slip distribution generated by *Kim*

and Dreger [2008] using a joint inversion of seismic, GPS, and InSAR data. Both inversions demonstrate two peaks of slip separated along strike with the majority of slip occurring at less than 10 km depth. Both inversions are able to resolve two zones of peak slip within the northernmost asperity. In general, seismic waveform inversions are better suited for resolving the extent of deep slip, and both inversions here demonstrate a similar depth for the termination of slip while other slip inversions from geodetic data generate deeper slip. This suggests that variable fault discretizing allows us to better resolve the lack of deep slip with geodetic observations alone than would otherwise be possible with an evenly discretized fault.

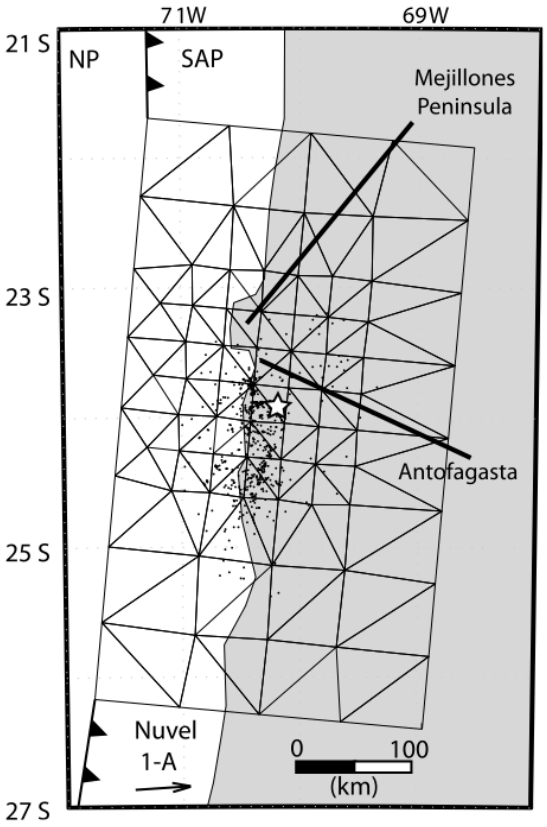

Figure 3.11: Final fault parameterization for inversion of the Antofagasta earthquake interferograms containing 130 total dislocations. Dots are aftershocks for the 1995 event [Husen et al., 1999]. Arrow is Nuvel-1A plate motion vector [DeMets et al., 1994]. Barbed lines are the along-strike extension of the subduction trench. NP, Nazca Plate; SAP, South American Plate.

3.5.2 The 1995 Antofagasta Subduction Zone Event

The 2004 Parkfield earthquake presented an example of an event well constrained by surface displacement observations over a relatively small region. Here, we use the 1995 Mw 8.1 Antofagasta earthquake in South America as an example of how a broad and densely sampled deformation field affects our discretization algorithm (Figure 3.11). Furthermore, it presents an opportunity to apply our approach to a dip-slip earthquake. On 30 August 1995, the earthquake ruptured 180 km of the Chilean subduction zone near the Mejillones Peninsula in Chile [Klotz et

al., 1999]. Previous work [*Delouis et al.*, 1997; *Pritchard et al.*, 2002] demonstrates that the megathrust ruptured in a single direction to the south with broad regions of smooth slip of up to 5 meters. For inverting co-seismic slip from GPS and InSAR observations, Pritchard et al. [2002] used a variably discretized fault plane with 41 rectangular dislocations. Sizes of the patches were chosen manually to optimize the diagonal of the model resolution matrix, **R**.

3.5.2.1 Data and Model Parameters

The InSAR observations were made from ERS-1and ERS-2 radar images spanning 1992–1997. Multiple highly coherent ascending and descending interferograms are available for this event thanks in part to the highly arid climate of northern Chile. The data set includes 8 co-seismic interferograms, 7 from ascending tracks 96 and 325, and one from descending track 89. Images were processed using the Caltech/JPL developed ROIPAC software package. Please see Pritchard et al. [2002] for a full discussion of the processing of this data set. We resample the interferograms using the method of Lohman and Simons [2005] and allow for anisotropic model covariance. The noise in the data considered here appears to be only weakly anisotropic so that assumptions of stationary isotropic noise would most likely be appropriate [*Lohman and Barnhart*, 2010]. Resampling of the data allows us to reduce the total number of observation points from the order of 10^6 to a computationally manageable 2797.

We fix the fault plane to a single plane geometry using both centroid solutions and aftershock locations (Figure 3.11)[*Husen et al.*, 1999]. We assume a strike of 005°, dip of 20° to the east, and 500 × 300 km fault dimensions. We allow the fault to intersect the surface at the trench and fix the fault vertices to 25.6545°S, 71.793°W and 21.167°S, 71.2808°W. Due to spatial signal restrictions at the Chilean shoreline, the line- of-sight (LOS) deformation signal

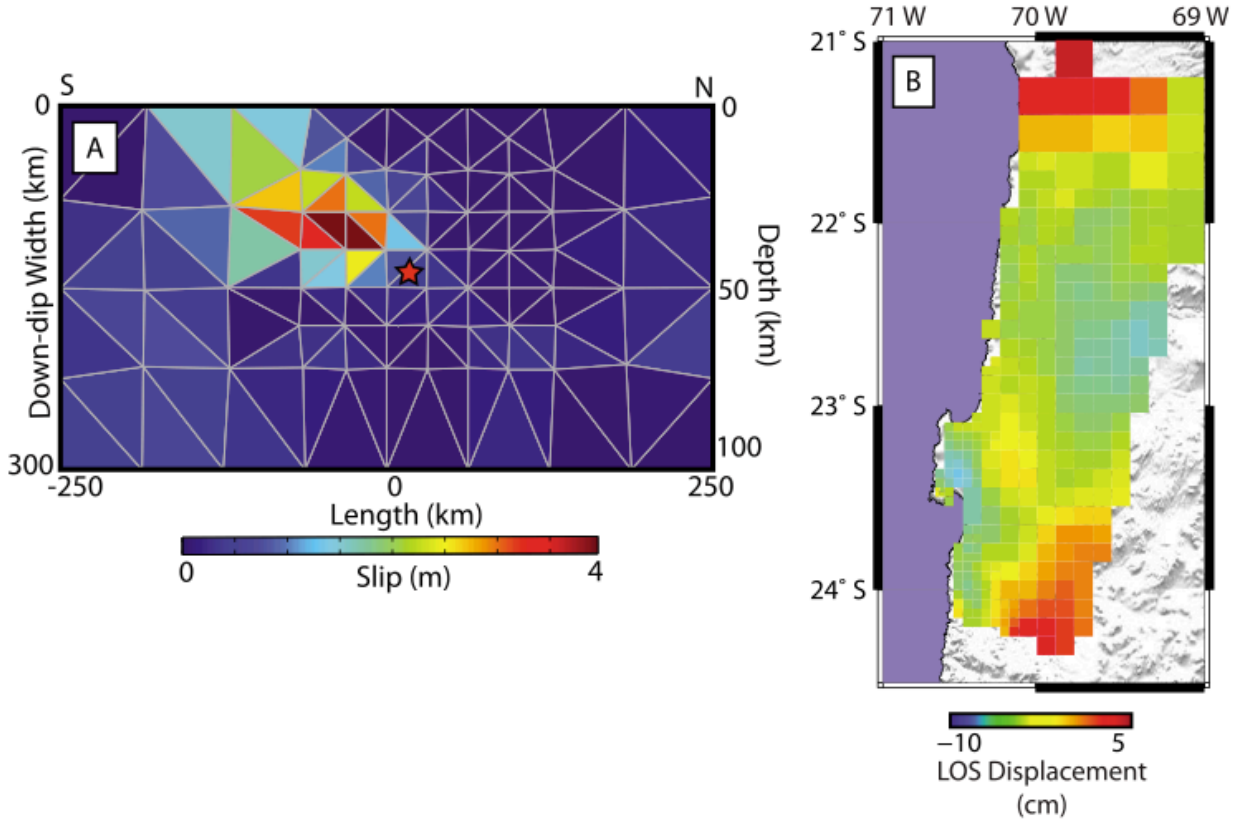

Figure 3.12: (a) Inverted slip distribution for the Antofagasta earthquake. Star is the Harvard centroid moment tensor located hypocenter. Figure 14a is to the scale of the downdip width and along-strike length. Absolute depth is shown as a reference but is not to scale with the length. (b) Model misfit of the resampled track 96 interferogram. Scale of model misfit is magnitude of surface displacements in the direction of the line of sight of the satellite, in cm. Image is draped over Shuttle Radar Topography Mission topography [Farr et al. 2007].

demonstrates principally subsidence with a small amount of uplift along the Mejillones Peninsula. Depending on inferred fault geometry and location, this signal can be fit by either thrust or normal motion. We know through inverted moment tensors and aftershock locations [Klotz et al., 1999] that this event ruptured the subduction interface; thus, we fix the approximate geometry of the subduction zone interface as our model geometry and do not allow rake to vary, fixing it to the plate motion vector of 87° from the strike direction [*DeMets et al.*, 1994]. We impose positivity constraints that ensure all slip is entirely thrust motion, so the inverse problem is nonlinear. In order to account for the effects of interseismic and postseismic deformation as well as long amplitude variations in signal from coast-parallel gradients in atmospheric water

content, we include a model for a quadratic ramp in our inversions. All resampled interferograms and ramps used in the slip inversion, as well as the data misfits of each interferogram, are shown in the auxiliary material.

3.5.2.2 Inversion Results

As for the Parkfield GPS data, we apply the algorithm of complete mesh resampling with triangles described previously to our fault geometry, beginning with an initial discretization of 100 dislocations and a percent difference tolerance of 0.10. We are able to derive a preferred fault discretization after four iterations (Figure 3.11, with aftershocks). Unlike the Parkfield fault discretization, the Antofagasta fault discretization does not demonstrate steep gradients in dislocation size. We expect such behavior because the InSAR observation points demonstrate much lower spatial variability between adjacent points than GPS stations. The data for this event are located only onshore, far from where the dipping subducting slab is shallow and near the surface offshore. Likewise, the slab dips shallowly, so there is not a large variation in depth to the fault plane perpendicular to the fault as there was for the Parkfield earthquake. The shallowly dipping slab and restriction of the observable deformation field leads to a smooth, broad deformation pattern of subsidence which in turn leads to a discretization with relatively homogenous dislocation sizes. The preferred fault discretization has smaller patches at the center of the fault and extending up-dip to the trench and offshore (Figure 3.11, 3.12). The smaller offshore dislocations are confined to the center portion of the fault along strike. This region of high resolution offshore reflects data coherence on the Mejillones Peninsula. Dislocation size increases both to the north and south along strike and down-dip. Increases in dislocation size along strike north and south of the main rupture region are due to fewer interferograms that

extend to the edge of the data distribution. down-dip increases in dislocation size are due in part to the distribution of the resampled data and increasing distance from the data with depth.

Our preferred slip model is shown in Figure 3.12a. The model demonstrates deepest slip well constrained to a depth of ~50 km, the approximate depth of rupture initiation (starred). Peak slip of 4.7 m is observed updip and to the south of the initial rupture point, supporting seismic observations that the rupture propagated unilaterally to the south. A single, broad region of slip extends from the initial rupture depth to the trench interface. We infer a geodetic moment of 1.9 × 1021 N m, or Mw 8.15 using a shear modulus of 34 GPa. The geometry and magnitude of our slip model are in general agreement with that proposed by Pritchard et al. [2002] in which they model a peak slip of ~5 m and a broad slip region extending from the rupture centroid to the trench interface. Figure 3.12b shows the model misfit for the track 96 interferogram. As we did with the Parkfield earthquake, we compare our inversion to one similar to that of Pritchard et al. [2002] via the $_jR_i$ criterion. We calculate $_jR_i$ for a slip distribution inverted using the discretization of Pritchard et al. [2002] and find that our method produces a lower $_jR_i$ value. The results of this test are shown in the auxiliary material.

3.6 Conclusions

The examples presented here demonstrate that our proposed methods for fault discretizing yield dislocation distributions which robustly resolve slip features where uniformly discretized models cannot. By using discretized fault models that accurately reflect the resolving power of the data, we can place greater confidence on inferred slip models and verify the robustness of distinct slip features inverted on to uniformly discretized models. Our synthetic cases demonstrate that the method discussed in section 3.3.4 for complete mesh resampling works well

and agrees with models that are "optimally" discretized evenly into rectangular dislocations.

The utility of the complete mesh resampling routine becomes evident when we consider slip inversions onto faults that are not uniformly discretized with an "optimal" number of dislocations. For example, in the synthetic tests, we invert slip onto faults evenly discretized with a number of dislocations similar to that derived through variable discretization. These inversions appear very similar to the inversions using a variably discretized grid, demonstrate negligible differences in data misfit, and produce similar $_{j}\boldsymbol{R}_{i}$ values. However, when we invert onto fault planes that are uniformly discretized with much greater or fewer dislocations (Figure 3.8), the resolutions of the models are greatly affected, as evidenced by poorer $_{j}\boldsymbol{R}_{i}$ values and worse recovery of input slip geometry and magnitude. The complete mesh resampling routine allows us to determine the "optimal" fault discretization without a priori knowledge of the model resolution. We are also able to avoid guess and check approaches while maximizing our computational efficiency with respect to deriving pertinent, real information about the slip geometry. The approach discussed here could be part of a data assimilation strategy where we would iterate between attempting to maximize the resampled data distribution [e.g., Lohman and Simons, 2005] and the parameterization of the fault plane.

Furthermore, as proven through our inversion of the Parkfield Earthquake using only GPS data, we are able to accurately resolve regions of the fault where slip is absent. Resolution of these regions is increasingly important in understanding the significance of observed shallow slip deficits, termination of deep slip, and termination of slip along- strike. The manner in which slip decays to zero along-strike plays an important role in stress transfer between fault segments or within sequences of earthquakes. This will prove especially important when considering slip

distributions of the 2010 Baja California event where aftershocks are concentrated at the northern end of the rupture where slip may have abruptly terminated. The Parkfield earthquake example also allows us to demonstrate that through variable fault discretization, we are able to accurately resolve slip features using a single set of geodetic observations that before were only imaged through seismic inversions or joint inversions of multiple geodetic observations. The ability to derive a model that can robustly resolve slip with minimal geodetic observations will prove to be a vital tool for studies in both remote and highly vegetated/developed regions.

3.7 References

Akaike, H. (1980), Likelihood and the Bayes procedure, *Trabajos de Estadística y de Investigación Operativa*, *31*(1), 143–166, doi:10.1007/BF02888350.

Árnadóttir, T., and P. Segall (1994), The 1989 Loma Prieta earthquake imaged from inversion of geodetic data, *J. Geophys. Res.*, *99*(B11), 21835–21,855, doi:10.1029/94JB01256.

Bakun, W. H., and A. G. Lindh (1985), The Parkfield, California, Earthquake Prediction Experiment, *Science*, *229*(4714), 619–624, doi:10.1126/science.229.4714.619.

Bakun, W. H. et al. (2005), Implications for prediction and hazard assessment from the 2004 Parkfield earthquake, *Nature*, *437*(7061), 969–974, doi:10.1038/nature04067.

Barnhart, W. D., and R. B. Lohman (2010), Automated fault model discretization for inversions for co-seismic slip distributions, *J. Geophys. Res.*, *115*(B10), B10419, doi: 10.1029/2010JB007545.

Biggs, J., E. Bergman, B. Emmerson, G. J. Funning, J. Jackson, B. Parsons, and T. J. Wright (2006), Fault identification for buried strike-slip earthquakes using InSAR: The 1994 and 2004 Al Hoceima, Morocco earthquakes, *Geophysical Journal International*, *166*(3), 1347–1362, doi:10.1111/j.1365-246X.2006.03071.x.

Cervelli, P., M. H. Murray, P. Segall, Y. Aoki, and T. Kato (2001), Estimating source parameters from deformation data, with an application to the March 1997 earthquake swarm off the Izu Peninsula, Japan, *J. Geophys. Res.*, *106*(B6), 11217–11,237, doi: 10.1029/2000JB900399.

Delouis, B. et al. (1997), The Mw = 8.0 Antofagasta (northern Chile) earthquake of 30 July 1995: A precursor to the end of the large 1877 gap, *Bulletin of the Seismological Society of America*, *87*(2), 427–445.

DeMets, C., R. G. Gordon, D. F. Argus, and S. Stein (1994), Effect of recent revisions to the geomagnetic reversal time scale on estimates of current plate motions, *Geophys. Res. Lett.*, *21*(20), 2191–2194, doi:10.1029/94GL02118.

Du, Y., A. Aydin, and P. Segall (1992), Comparison of various inversion techniques as applied to the determination of a geophysical deformation model for the 1983 Borah Peak earthquake, *Bulletin of the Seismological Society of America*, *82*(4), 1840–1866.

Du, Y., P. Segall, and H. Gao (1997), Quasi‐static dislocations in three dimensional inhomogeneous media, *Geophys. Res. Lett.*, *24*(18), 2347–2350, doi: 10.1029/97GL02341.

Freed, A. M., and J. Lin (2001), Delayed triggering of the 1999 Hector Mine earthquake by viscoelastic stress transfer, *Nature*, *411*(6834), 180–183, doi:10.1038/35075548.

Freed, A. M., R. Bürgmann, E. Calais, J. Freymueller, and S. Hreinsdóttir (2006), Implications of deformation following the 2002 Denali, Alaska, earthquake for postseismic relaxation processes and lithospheric rheology, *J. Geophys. Res.*, *111*(B1), B01401, doi: 10.1029/2005JB003894.

Freymueller, J., N. E. King, and P. Segall (1994), The co-seismic slip distribution of the Landers earthquake, *Bulletin of the Seismological Society of America*, *84*(3), 646–659.

Funning, G. J., B. Parsons, T. J. Wright, J. A. Jackson, and E. J. Fielding (2005), Surface displacements and source parameters of the 2003 Bam (Iran) earthquake from Envisat advanced synthetic aperture radar imagery, *J. Geophys. Res.*, *110*(B9), B09406, doi: 10.1029/2004JB003338.

Hanssen, R. F. (2001), *Radar Interferometry: Data Interpretation and Error Analysis*, Springer.

Harris, R. A., and P. Segall (1987), Detection of a locked zone at depth on the Parkfield, California, segment of the San Andreas Fault, *J. Geophys. Res.*, *92*(B8), 7945–7962, doi: 10.1029/JB092iB08p07945.

Hreinsdóttir, S., J. T. Freymueller, H. J. Fletcher, C. F. Larsen, and R. Bürgmann (2003), Co-Seismic slip distribution of the 2002 MW7.9 Denali fault earthquake, Alaska, determined from GPS measurements, *Geophys. Res. Lett.*, *30*(13), 1670, doi: 10.1029/2003GL017447.

Husen, S., E. Kissling, E. Flueh, and G. Asch (1999), Accurate hypocentre determination in the seismogenic zone of the subducting Nazca Plate in northern Chile using a combined on-/offshore network, *Geophysical Journal International*, *138*(3), 687–701, doi:10.1046/j.1365-246x.1999.00893.x.

Ide, S., M. Takeo, and Y. Yoshida (1996), Source process of the 1995 Kobe earthquake:

Determination of spatio-temporal slip distribution by Bayesian modeling, *Bulletin of the Seismological Society of America*, *86*(3), 547–566.

Jackson, D. D., and M. Matsu'ura (1985), A Bayesian approach to nonlinear inversion, *J. Geophys. Res.*, *90*(B1), 581–591, doi:10.1029/JB090iB01p00581.

Johanson, I. A., E. J. Fielding, F. Rolandone, and R. Bürgmann (2006), Co-Seismic and Postseismic Slip of the 2004 Parkfield Earthquake from Space-Geodetic Data, *Bulletin of the Seismological Society of America*, *96*(4B), S269–S282, doi:10.1785/0120050818.

Johnson, K. M., Y.-J. Hsu, P. Segall, and S.-B. Yu (2001), Fault geometry and slip distribution of the 1999 Chi-Chi, Taiwan Earthquake imaged from inversion of GPS data, *Geophys. Res. Lett.*, *28*(11), 2285–2288, doi:10.1029/2000GL012761.

Jónsson, S., H. Zebker, P. Segall, and F. Amelung (2002), Fault Slip Distribution of the 1999 Mw 7.1 Hector Mine, California, Earthquake, Estimated from Satellite Radar and GPS Measurements, *Bulletin of the Seismological Society of America*, *92*(4), 1377–1389, doi: 10.1785/0120000922.

Kim, A., and D. S. Dreger (2008), Rupture process of the 2004 Parkfield earthquake from near-fault seismic waveform and geodetic records, *J. Geophys. Res.*, *113*(B7), B07308, doi: 10.1029/2007JB005115.

Langbein, J. et al. (2005), Preliminary Report on the 28 September 2004, M 6.0 Parkfield, California Earthquake, *Seismological Research Letters*, *76*(1), 10–26, doi:10.1785/gssrl. 76.1.10.

Langbein, J., J. R. Murray, and H. A. Snyder (2006), Co-Seismic and Initial Postseismic Deformation from the 2004 Parkfield, California, Earthquake, Observed by Global Positioning System, Electronic Distance Meter, Creepmeters, and Borehole Strainmeters, *Bulletin of the Seismological Society of America*, *96*(4B), S304–S320, doi: 10.1785/0120050823.

Lohman, R. B., and W. D. Barnhart (2010), Evaluation of earthquake triggering during the 2005–2008 earthquake sequence on Qeshm Island, Iran, *J. Geophys. Res.*, *115*(B12), B12413, doi:10.1029/2010JB007710.

Lohman, R. B., and M. Simons (2005), Some thoughts on the use of InSAR data to constrain models of surface deformation: Noise structure and data downsampling, *Geochem. Geophys. Geosyst.*, *6*(1), Q01007, doi:10.1029/2004GC000841.

Meade, B. J. (2007), Algorithms for the calculation of exact displacements, strains, and stresses for triangular dislocation elements in a uniform elastic half space, *Computers & Geosciences*, *33*(8), 1064–1075, doi:10.1016/j.cageo.2006.12.003.

Menke, W. (2012), *Geophysical Data Analysis: Discrete Inverse Theory, Third Edition: MATLAB Edition*, 3rd ed., Academic Press.

Murray, J., and J. Langbein (2006), Slip on the San Andreas Fault at Parkfield, California, over Two Earthquake Cycles, and the Implications for Seismic Hazard, *Bulletin of the Seismological Society of America*, *96*(4B), S283–S303, doi:10.1785/0120050820.

Okada, Y. (1992), Internal Deformation Due to Shear and Tensile Faults in a Half-Space, *Bull. Seismol. Soc. Amer.*, *82*(2), 1018–1040.

Page, M. T., S. Custódio, R. J. Archuleta, and J. M. Carlson (2009), Constraining earthquake source inversions with GPS data: 1. Resolution-based removal of artifacts, *J. Geophys. Res.*, *114*(B1), B01314, doi:10.1029/2007JB005449.

Parker, R. L. (1977), Understanding Inverse Theory, *Annual Review of Earth and Planetary Sciences*, *5*(1), 35–64, doi:10.1146/annurev.ea.05.050177.000343.

Pritchard, M. E., M. Simons, P. A. Rosen, S. Hensley, and F. H. Webb (2002), Co-seismic slip from the 1995 July 30 Mw= 8.1 Antofagasta, Chile, earthquake as constrained by InSAR and GPS observations, *Geophysical Journal International*, *150*(2), 362–376, doi:10.1046/j.1365-246X.2002.01661.x.

Sambridge, M. (1999), Geophysical inversion with a neighbourhood algorithm—I. Searching a parameter space, *Geophysical Journal International*, *138*(2), 479–494, doi:10.1046/j.1365-246X.1999.00876.x.

Segall, P., and R. Harris (1987), Earthquake deformation cycle on the San Andreas Fault near Parkfield, California, *J. Geophys. Res.*, *92*(B10), 10511–10,525, doi:10.1029/JB092iB10p10511.

Simons, M., Y. Fialko, and L. Rivera (2002), Co-Seismic Deformation from the 1999 Mw 7.1 Hector Mine, California, Earthquake as Inferred from InSAR and GPS Observations, *Bulletin of the Seismological Society of America*, *92*(4), 1390–1402, doi:10.1785/0120000933.

Zhao, S., R. D. Müller, Y. Takahashi, and Y. Kaneda (2004), 3-D finite-element modelling of deformation and stress associated with faulting: effect of inhomogeneous crustal structures, *Geophysical Journal International*, *157*(2), 629–644, doi:10.1111/j.1365-246X.2004.02200.x.

CHAPTER 4

INSAR AND OPTICAL CONSTRAINTS ON FAULT SLIP DURING THE 2010-2011 NEW ZEALAND EARTHQUAKE SEQUENCE[1]

4.1 Introduction

Our study used space-based interferometric synthetic aperture radar (InSAR) and feature tracking on sub-meter-resolution optical imagery pairs to characterize surface deformation resulting from the 4 September 2010 M_w 7.1 Darfield, 22 February 2011 M_w 6.3 Christchurch, and 13 June 2011 Christchurch earthquakes (dates in local time) (Figure 4.1), each of which occurred in the Canterbury region of the South Island of New Zealand. A rapid, coordinated international emergency response is often required when strong-motion earthquakes hit urban areas. Unfortunately in these cases relief workers often have little information about the location or the extent of damage. Remote sensing can rapidly provide maps of certain key variables (*i.e.*, building damage, potential loading of nearby faults, etc.) to relief workers on the ground. These maps can cover broad areas on time scales that are only limited by the revisit time of the satellite or aircraft. Critically, imagery types such as satellite-based synthetic aperture radar (SAR) have long repeat times of up to 46 days at present, although the existence of overlapping tracks and multiple satellite platforms effectively reduces the repeat time somewhat. Here we demonstrate the impact of commercial optical imagery that can be acquired within hours to days after an earthquake, with the goal of supporting relief efforts in future earthquakes on a more rapid timescale than can be achieved with SAR imagery alone. We demonstrate that these sub-meter-

[1] Published as: Barnhart, W.D., M.J. Willis, R.B. Lohman, A.K. Melkonian (2011) InSAR and optical constraints on fault slip during the 2010-2011 New Zealand earthquake sequence. *Seism. Res. Letts.* 82 (6), 800-809. Reprinted with permission from the Seismological Society of America.

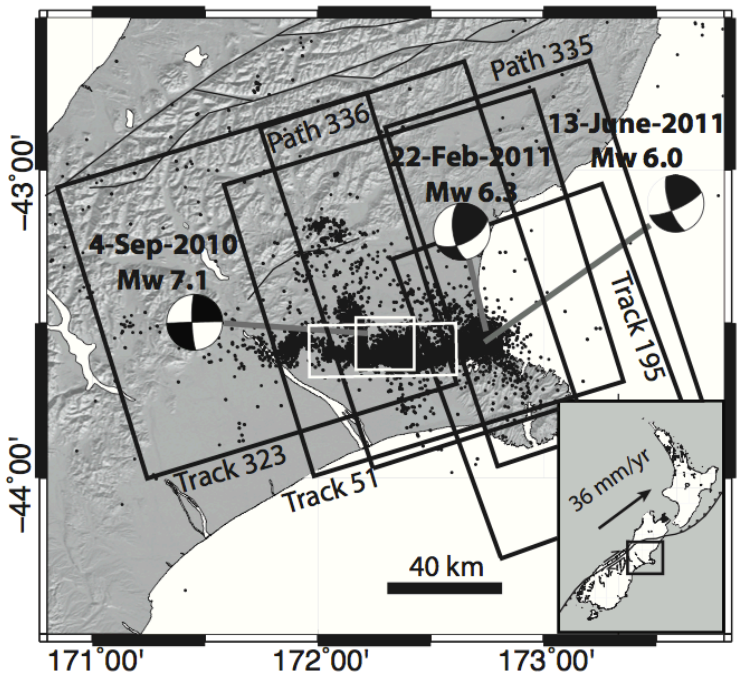

Figure 4.1: Study region and spatial coverage of data. Focal mechanisms are Global Centroid Moment Tensor (GCMT; Dziewonski et al. 1981) solutions for the 4-Sep-2010, 22-Feb- 2011, and 13-June-2011 Canterbury earthquakes. Faults (thin lines) and seismicity (black dots) are from GNS Geonet (http:// geonet.org.nz) with earthquake spanning the period 3-Sep-2010 to 1-Aug-2011. Boxes indicate extent of InSAR data (black) and optical imagery (white). Image overlaid on SRTM digital elevation model (Farr et al. 2007). Inset shows map location with major tectonic features and Nuvel-1A plate motion of Australia relative to fixed Pacific (DeMets et al. 1994).

resolution scenes are feasible tools for deriving near-fault surface displacements for use in fault slip inversions, even in areas of heavy agricultural activity.

The Darfield and Christchurch earthquakes present an opportunity to observe postseismic deformation related to multiple moderate (< M_w 7.5) earthquakes occurring in close spatial and temporal proximity with an unprecedented set of seismic and geodetic constraints spanning the two events. While there are many examples of earthquakes of this size occurring in close proximity, including the 1992 Landers and 1999 Hector Mine earthquakes, the shorter time interval between the Darfield and Christchurch events means that many instruments that were deployed after the first earthquake were still in place to observe the second and third events. We perform inversions of these data for the spatial distribution of fault slip that occurred during each of these earthquakes and assess the potential contribution of the static Coulomb stress change that occurred during the Darfield event to the eventual rupture of the Christchurch earthquake.

4.2 Tectonic Setting

The 2010–2011 Canterbury earthquake sequence occurred east of the dominantly strike-slip Pacific-Australian plate boundary, on previously unrecognized faults within the topographically smooth Canterbury Plains (Figure 4.1). The Darfield earthquake (M_w 7.0–7.1) ruptured nearly 40 km of the northern Canterbury Plains, partially on the now recognized Greendale fault, leaving extensive surface ruptures and ground warping [*Quigley et al.*, 2012]. Though surface ruptures suggest dominantly right lateral strike-slip motion, aftershock locations and focal mechanisms, first motion focal mechanisms, and subsequent geodetic modeling show that the event consisted of a complex rupture sequence involving NE-SW striking reverse faults in addition to E-W striking right lateral strike-slip faults [*Beavan et al.*, 2010; *Gledhill et al.*, 2011]. The 22 February 2011 (hereafter, 22-Feb) Christchurch earthquake (M_w 6.3, Figure 4.1) that followed five months later occurred as part of a sequence of aftershocks to the east that illuminated numerous zones characterized by both E-W striking strike slip and NE-SW striking reverse slip (Figure 4.1). The 22-Feb Christchurch event was dominantly reverse slip and occurred near the contact between the volcanic Banks Peninsula and poorly consolidated sediments underlying Christchurch. Unlike the Darfield earthquake, the 22-Feb Christchurch earthquake led to significant urban damage and casualties due both to its shallow source, its exceptionally strong ground motion [*Bradley and Cubrinovski*, 2011; *Fry and Gerstenberger*, 2011; *Iizuka et al.*, 2011], and proximity to the cities of Christchurch and Lyttelton (Figures 4.1 and 4.2). Another significant event (M_w 6.0) occurred 13 June 2011 (hereafter 13-June) near the Christchurch earthquake epicenter, causing further damage in the city of Christchurch. The Darfield earthquake exhibited a large stress drop of ~160 bars while the Christchurch events exhibited more moderate stress drops of 50–60 bars [*Fry and Gerstenberger*, 2011].

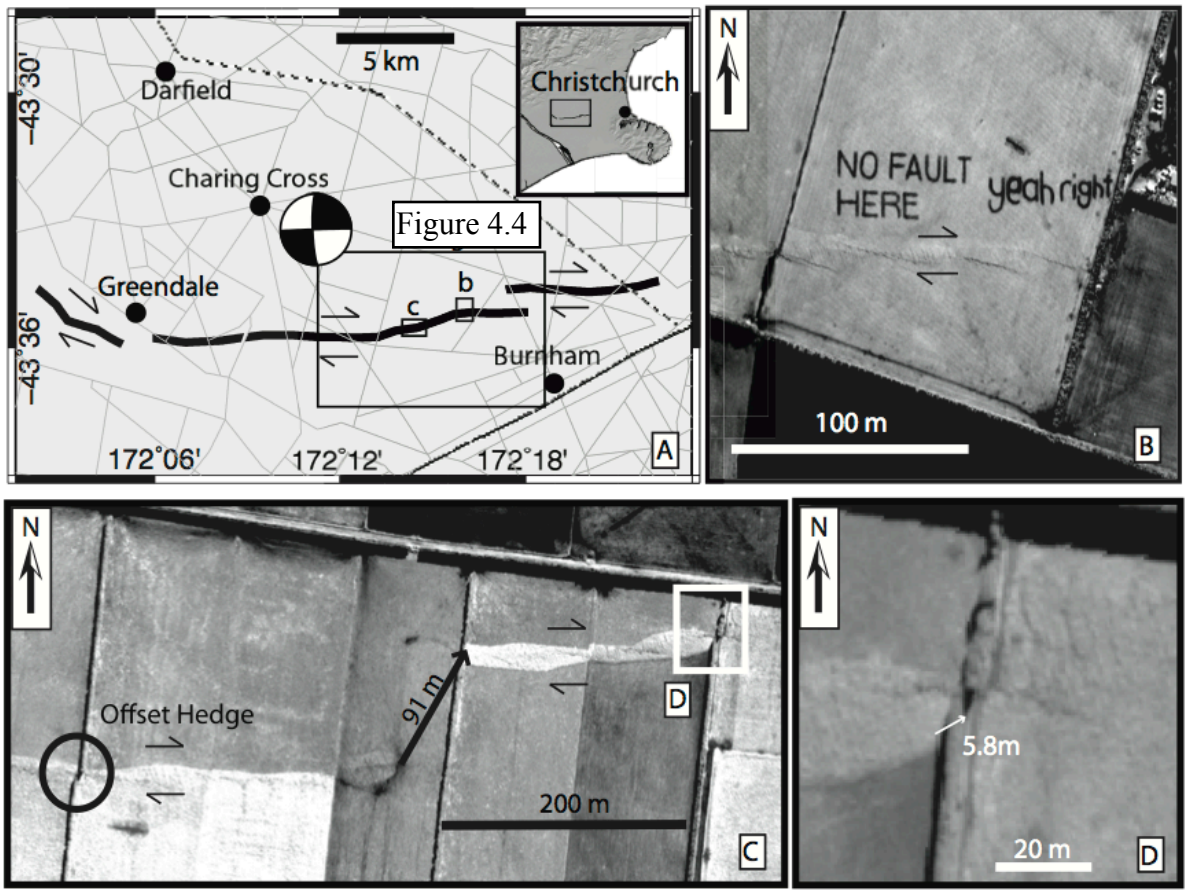

Figure 4.2: Examples of surface ruptures from the Darfield earthquake visible in postseismic WorldView 1 optical imagery. A) Overview map with surface rupture (thick black line, Quigley et al. 2011) and Global CMT solution for the Darfield event (Dziewonski et al. 1981). Roads (gray lines) and railroads (dashed lines) from http://www.diva-gis.org/. B) Example of surface rupture (arrows added by authors) and interpretive field text courtesy of local farmer (exists in field, not added by authors). C) En-echelon rupture jump of ~90 m (arrow), hedgerow offset by rupture (circle). D) Zoom view of hedge and canal offsets of ~5.8 m. Optical imagery copyright 2011 Digital Globe, provided through the NGA Commercial Imagery Program.

The city of Christchurch (Figure 4.1) is located on the eastern Canterbury Plains, an alluvial plain of Cretaceous through present sediments overlying the Late Paleozoic to Mid Cretaceous Torlesse terrain [*Mackinnon*, 1983]. The Banks Peninsula, an extinct Miocene volcanic structure, punctuates the eastern edge of the Canterbury Plains near Christchurch [*Timm et al.*, 2009]. Several other Cenozoic volcanic structures exist throughout the South Island, including near the city of Dunedin. Paleoseismic and GPS studies suggest that up to 80% of the 38 mm/yr relative Australian-Pacific plate motion occurring within the central South Island of

New Zealand [*DeMets et al.*, 1994; *Beavan et al.*, 1999; *Wallace et al.*, 2007] is accommodated by the Alpine fault [*Berryman et al.*, 1992; *Norris and Cooper*, 2001] while the Porter's Pass/ Amberly fault system, north of our study area, accommodates ~10–15% (3–8 mm/yr) [*Beavan et al. 1999; Wallace et al. 2007*]. The rates and rate uncertainties in the central South Island allow for up to 10 mm/yr of unaccounted strike-slip motion, which has been attributed to model errors or uplift in the foothills of the Southern Alps and strike-slip motion in the Canterbury Plains [*Beavan et al.*, 1999; *Sutherland et al.*, 2006; *Wallace et al.*, 2007]. Several large (>M 7.1) earthquakes are associated with the Porter's Pass fault zone in the Southern Alps foothills [*Howard et al.*, 2005] while other large Quaternary events are documented to the north in the Marlborough fault system [*Cowan*, 1991]. Documentation of active faults in the Marlborough fault system and Canterbury Plains reveals dominantly right lateral and reverse slip motion on shallow to steeply (>50 degrees) dipping planes.

Prior to the 2010–2011 earthquake sequence, the strongest historical ground motion in Christchurch was attributed to an M 7–8 event [*Stirling et al. 1999*], and the Canterbury Plains in this focus area were characterized by low to moderate rates of seismicity [*e.g., Pettinga et al. 2001*]. Seismic reflection surveys in the vicinity of the Darfield event revealed offsets and folding of Quaternary sediments older than 24 ka by thrust faults [*Dorn et al.*, 2010], leading those authors to suggest that infrequent events >M 7 with long recurrence intervals could be possible.

4.3 Data: Availability and Processing Results

Characteristics of the radar and optical data that we used in this work are summarized in Tables 4.1 and 4.2, respectively. Multiple pairs of SAR imagery with at least two different look

Satellite	Date1	Date2	Track	Frame	Bperp
Christchurch EQ: 22-Feb-2011					
ALOS	2011.01.10	2011.02.25	335	6300	421
ALOS	2010.10.27	2011.03.14	336	6290/6300	1178
Darfield EQ: 04-Sep-2010					
ALOS	2010.03.11	2010.09.11	336	6300	1215*
ALOS	2010.01.24	2010.10.27	336	6300	1893
ENVI	2010.09.01	2010.10.06	323	6309	236
ENVI	2010.07.09	2010.09.17	51	6309	532*
Post Darfield EQ					
ALOS	2010.09.11	2010.10.27	336	6300	231
ALOS	2010.09.11	2011.03.14	336	6300	1407
ALOS	2010.10.27	2011.03.14	336	6300	1173
Christchurch EQ: 13-June-2011					
ENVI	2011.06.08	2011.07.08	195	6291	14

Table 4.1: Pairs of SAR imagery used in this study for both traditional InSAR and horizontal offsets obtained through pixel tracking (*). Bperp is the perpendicular baseline for each pair, in meters. Dates are in GMT.

angles span each earthquake (spatial coverage shown in Figure 4.1, 4.3), as well as the period in between them, allowing some redundancy in the data and the assessment of whether individual features in the data are associated with the earthquake or with noise. Because of the limited number of acquisitions, we only use ascending tracks, which restricts our ability to constrain the three-dimensional deformation field for each event. For the Darfield earthquake, we successfully obtained SAR pixel offsets, which constrain displacements in the horizontal, alongtrack direction and provide an additional component of the three-dimensional deformation field [*Fialko et al.*, 2001]. We processed interferograms using the Caltech/JPL InSAR processing package ROI_PAC [*Rosen et al.*, 2004], using a digital elevation model from the Satellite Radar Topography Mission [*Farr et al.*, 2007]. PALSAR imagery from the ALOS satellite was provided by

Satellite	Date	Resolution (m)	Band	Pre/Post-seismic
		Feb. 2011 Christchurch EQ		
WorldView-1	2010.09.21	0.5	Panchromatic	Pre
WorldView-1	2011.02.26	0.5	Panchromatic	Post
		Darfield EQ		
GeoEye	2009.10.23	0.5	Panchromatic	Pre
WorldView-2	2010.09.21	0.5	Panchromatic	Post
ASTER	2006.02.11	15	-	Pre
ASTER	2010.09.18	15	-	Post

Table 4.2: Optical data used in this study. Dates are in GMT. Optical imagery copyright 2010 Digital Globe, provided by the NGA Commercial Imagery Program.

Japanese Aerospace Exploration Agency (JAXA) through an agreement with NASA and the Alaska Satellite Facility (ASF). ENVISAT imagery was acquired through a Category-1 agreement with the European Space Agency (ESA).

The strong shaking, liquefaction, and high strain gradient resulted in interferograms that require some manual phase unwrapping to connect coherent zones separated by regions of decorrelation. In these cases, we ensured that the phase unwrapping was consistent across spatially overlapping interferograms by inspection and comparison to the predicted displacement field resulting from our inversion. The large number of pixels (several million) in the final InSAR data products would be prohibitively computationally expensive to ingest into any inversion scheme. Therefore, we subsample the data using the procedure outlined in [*Lohman and Simons*, 2005] so that we retain a set of spatial averages with 138 to 376 points for each interferogram. Because we were not able to unambiguously unwrap coherent phases across the Darfield rupture for Envisat Track 51, we treat the regions north and south of the Darfield

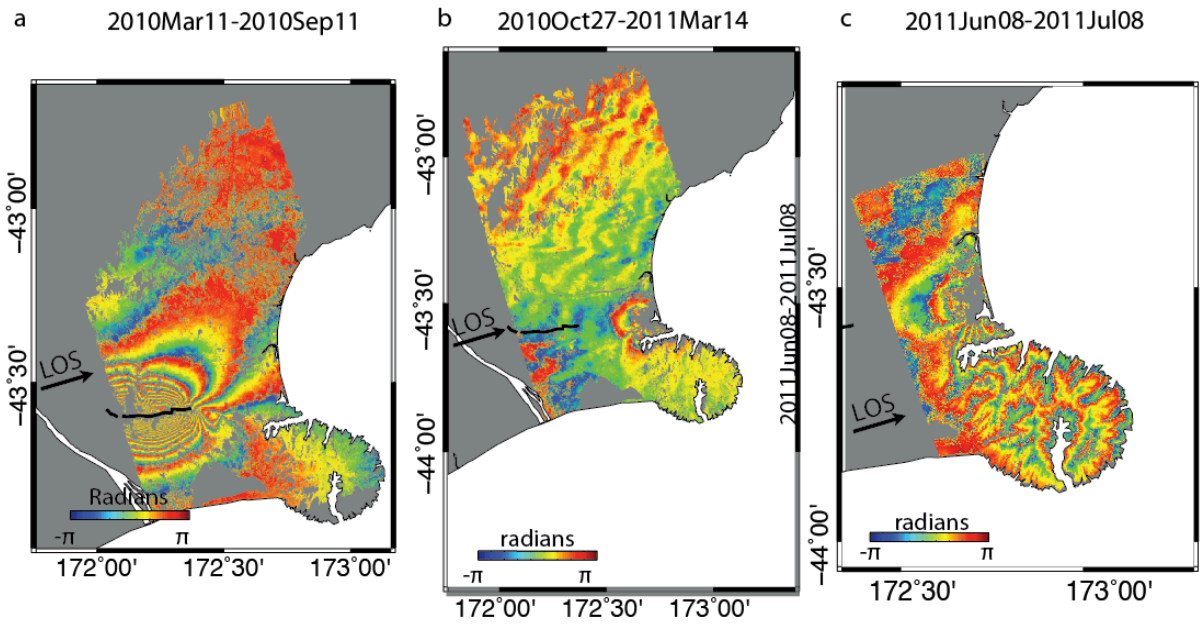

Figure 4.3: Example ascending wrapped interferograms from the a) Darfield Earthquake, b) Feb 2011 Christchurch Earthquake, and c) June 2011 Christchurch Earthquake. Black line indicates Darfield rupture trace.

rupture as two separate data sets. Peak line of sight (LOS) offsets during the Darfield earthquake were around two meters, with horizontal pixel tracking results of up to five meters. There were at least three distinct strike-slip fault planes and two zones of thrust faulting activated during the Darfield earthquake [*Beavan et al.*, 2010; *Gledhill et al.*, 2011; *Quigley et al.*, 2012]. This rupture complexity is apparent in the complicated, multi-lobed deformation field imaged with InSAR and aftershock locations (Figure 4.1, 4.3).

The 22-Feb and 13-June Christchurch earthquakes exhibit a much simpler appearance in the InSAR observations (Figure 4.3), although there is a large region of decorrelation within the city of Christchurch, and some of the deformation occurred offshore where it cannot be imaged with InSAR. The steep gradients of deformation suggest a shallow, near-surface slip source, as supported by our inversion described below. Peak observed LOS deformation associated with the 22-Feb Christchurch earthquake is 0.52 meters. We were unable to obtain subpixel, horizontal offsets from SAR imagery for the 22-Feb event, which suggests either there was no surface

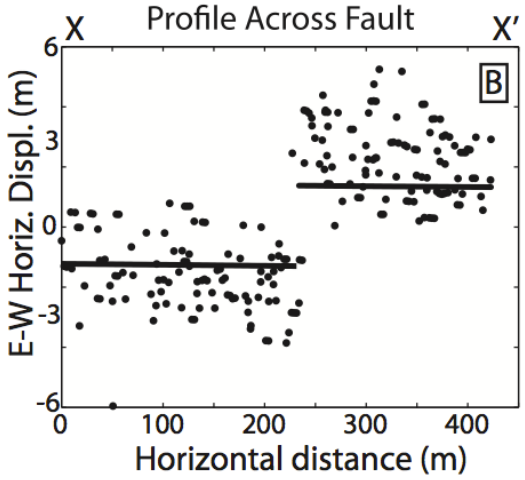

Figure 4.4: Pixel tracking results from Darfield coseismic optical imagery pairs. A) Calculated east-west pixel offsets overlaid on WorldView 1 postseismic scene (location in Figure 4.2A). Positive=east motion, negative=west motion. Pixels with a signal-to-noise ration less than 3.5 and standard deviation in the E-W component greater than 0.025 m have been masked. Black lines are mapped fault trace based on expression of surface rupture in the postseismic image. B) Profile X–X′ across the fault showing values of pixel offsets (black dots) and displacement predicted by the slip distribution shown in Figure 4.5A. Optical imagery copyright 2011 Digital Globe, provided through the NGA Commercial Imagery Program.

rupture (as confirmed by field observations) or any surface offsets were below the noise level of subpixel offset tracking (typically on the order of a meter).

High-resolution (~0.5 m resolution) optical imagery (Figure 4.2, Table 4.2) from commercial satellites was made available to scientists via the U.S. National Geospatial Agency and the National Science Foundation. We also explored the use of data from the Advanced Spaceborne Thermal Emission and Reflection Radiometer (ASTER) (Table 4.2), which has lower spatial resolution but is available on a more consistent, global basis, particularly for preseismic imagery that may not be acquired as part of the background mission for commercial

satellites. Previous work using cross-correlation of optical imagery has been primarily limited to ASTER and SPOT imagery [*Jean-Philippe Avouac*, n.d.; *Crippen and Blom*, 1991; *Michel*, 2002; *Debella-Gilo and Kääb*, 2011], with spatial resolutions of 15 and 2.5–10 m, respectively. For comparison, the GeoEye imagery used here has a pixel size of 0.5 m. We performed normalized cross-correlation of imagery [*Melkonian et al.*, 2009] processed using the *ampcor* program contained within the ROI_PAC software package [*Rosen et al.*, 2004]. Results for the higher resolution commercial data are described below, but we were unable to clearly resolve subpixel offsets for either of the earthquakes based on ASTER imagery due to striping within the data.

The GeoEye-1 satellite acquired pre-event high-resolution imagery on 23 October 2009. The panchromatic 15 km × 15 km scene is down-sampled from 41-cm resolution to 50-cm resolution for civilian use. The satellite, launched in September 2008, has precise pointing capabilities providing scenes that are geolocated with a circular error of probability (CEP) of about six meters without the use of ground control points. We extract the radiometrically corrected JPEG2000 imagery from its National Imagery Transmission Format (NTF) wrapper using the Geographic Data Abstraction Library (version 1.8, http://www.gdal.org/). The resulting 8.5 Gb 16-bit unsigned integer geotiff is geocoded, reprojected to Universal Transverse Mercator (UTM) coordinates and registered and orthorectified to a 90-m SRTM digital elevation model [*Farr et al.*, 2007]. The post-event imagery comes from the Worldview-1 satellite. This satellite, launched in September 2007, has a revisit time of 1.9 days and began imaging the Canterbury region almost immediately after the earthquake. Unfortunately clouds hampered acquisition until 21 September 2010, 17 days after the earthquake. We extracted the 17.9-km-swath-wide, half-meter panchromatic imagery using identical procedures as with the GeoEye-1 imagery.

Difficulties arise using this high-resolution imagery due to agricultural changes in the intervening year and different sun elevations and azimuths that result in a variable degree of shadowing from houses and hedgerows. Much of the imagery decorrelates over this time interval, in part because there have been dramatic changes in land use that are visible in the form of radical differences in relative brightness between fields and different plowing patterns between the two images. However, the hedgerows themselves, which are visually distorted across the fault in the postseismic images (Figures 4.2B–D), act as coherent features that provide very strong offsets from image to image. Since the hedgerows are effectively linear and have a similar brightness along their length, the offsets are better-resolved in a direction perpendicular to each hedgerow than they are along their length. Therefore, we obtain good characterization of the E-W deflection of N-S trending hedgerows across the fault, but poor results for E-W motion of hedgerows and roads that trend in a near E-W direction. Since the horizontal displacements in the E-W direction are much larger than those in the N-S direction for this earthquake, the most useful features in the imagery pixel tracking have been the N-S trending roads and hedgerows.

Figure 4.4 summarizes the results of optical imagery pixel tracking for the Darfield earthquake. Colored dots (Figure 4.4A) indicate the magnitude of displacement in an E-W direction of a 10×10 pixel box that was allowed to move for 32 pixels in any direction, posted at 5-pixel spacing. Peak displacements across the fault (Figure 4.4B) agree with what one would pick from the trend of the hedgerow using the postseismic imagery alone (Figure 4.2D). Although offsets in this example are only recoverable from anthropogenic features, processing images with shorter temporal baselines (days to months) produces coherent offsets in vegetated regions, validating that this technique can be used in remote regions if appropriate acquisitions

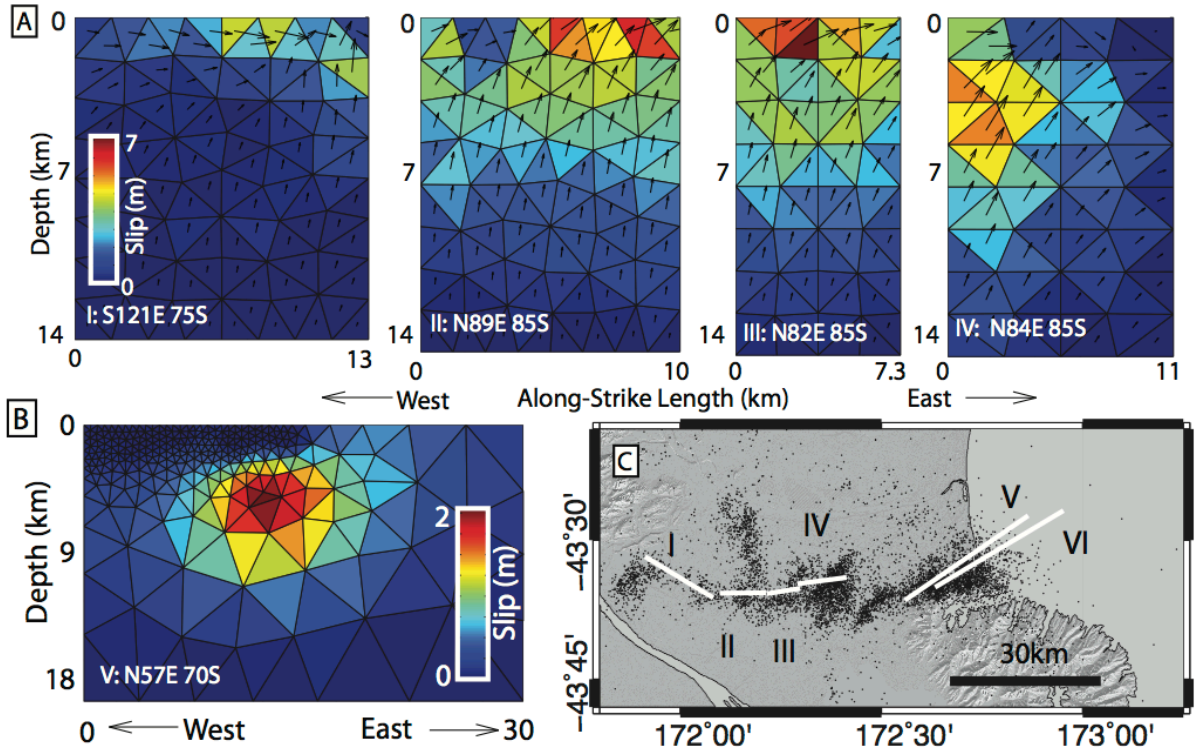

Figure 4.5: InSAR-based coseismic slip distributions. A) Darfield earthquake slip distribution. Arrows indicate motion of northern block relative to the southern block (right = right-lateral, up = reverse). Text describes strike and dip of each plane. Roman numerals correspond to fault model location in (C). B) 22-Feb Christchurch earthquake slip distribution. Text describes strike and dip of the plane. C) Model surface trace locations (I–IV: Darfield earthquake, V: 22-Feb Christchurch earthquake, VI: 13-June Christchurch earthquake). Dots are aftershocks from Geonet catalog for the period 3-Sept-2010 to 1-Aug-2011. Image overlaid on shaded SRTM DEM (Farr et al. 2007).

are available. Unfortunately, the only imagery available with these short temporal baselines is located away from the Darfield fault trace.

4.4 Modeling Results

4.4.1 Darfield Earthquake

For the Darfield and Christchurch earthquakes, we invert the geodetic observations for spatially distributed fault slip using planar fault geometries that we infer using a combination of nonlinear inversion and independent data such as surface ruptures, aftershocks, etc. For the Darfield earthquake, we use four steeply south-dipping planes to model the primarily right lateral strike-slip motion (Figures 4.5A and 4.5C) using a linear inversion for spatially distributed fault

slip on a set of 328 triangular dislocations (Meade 2007) with minimum moment regularization constraints. Beavan *et al.* [2010] demonstrated that shallow (~4 km) thrust slip in addition to right lateral slip is required to fully account for all features in the deformation field; however, our primary goal in interpreting the Darfield earthquake deformation field is to drive modeling of Coulomb stress change at the location of the Christchurch earthquake. At these distances, the effects of the shallow thrust faults are not likely to have a strong effect on Coulomb stress change [*King*, 2007]. Our Darfield fault model location is based on mapped surface ruptures [*Quigley et al.*, 2012] while dips are constrained by focal mechanisms of right lateral aftershocks. We extend our faults to the east and west to account for significant deformation apparent in the interferograms beyond mapped surface ruptures. Our best-fit slip distribution and model residual is shown in Figure 4.5A, with a moment magnitude of M_w 7.0. Slip magnitudes and depth ranges agree well with previous inversions by Beavan *et al.* [2010] using InSAR and GPS observations. We are unable to fit some features in the data near the center and easternmost end of the rupture (Figure 4.3A). The misfit is influenced by a combination of errors in model geometry, exclusion of NE-SW-dipping reverse faults, spatially correlated atmospheric noise, ionospheric perturbations, and contributions from significant postseismic deformation evident in postseismic interferograms and, therefore, likely present in varying degrees in the coseismic interferograms used in our inversions.

Figure 4.4B illustrates the predicted E-W horizontal offsets from our best-fit model at the location of the optical image pixel-tracking results. The predicted displacements across the fault are significantly smaller (~2.5 m compared with 5 m), which is not surprising given that there was a data gap in the InSAR imagery approaching the fault and that the regularization placed on

our inversion tends to reduce slip in regions that have less coverage by the data. The discrepancy may also be due, in part, to variable amounts of postseismic slip between the interferograms and the optical imagery. Overall, the difference between the observed displacements and those predicted using inversions based on InSAR data and an elastic halfspace model highlights both the importance of using near-field data when it exists as well as the potential for issues in using elastic models in regions where the deformation is clearly anelastic. However, these issues are likely to primarily affect the inversion for slip in the shallow subsurface and will not contribute much to the predicted Coulomb stress study discussed below.

4.4.2 Christchurch Earthquakes

To obtain a fault model for the Christchurch earthquakes, we use the Neighborhood Algorithm [*Sambridge*, 1999] to invert ALOS-PALSAR and Envisat interferograms (Table 4.1) for single fault dislocations. We then fix this bestfit geometry and extend the fault along-strike and down-dip to avoid spurious edge effects before performing a linear inversion for distributed slip. Model trace locations are shown in Figure 4.5C. We use the automated fault discretization algorithm described in Chapter 3 [*Barnhart and Lohman*, 2010]. For the 22-Feb event, we obtain a distributed slip model with 182 triangular dislocations (Figure 4.5B), with Laplacian smoothing constraints to regularize the inversion. We fix the slip rake direction to 64 degrees, as reported by the Global Centroid Moment Tensor (GCMT) solution [*Dziewonski et al.*, 1981]. Inversions in which we allow rake to vary reveal similar solutions. Our best-fit model strikes N57E and dips 70S beneath the Banks Peninsula. This fault geometry agrees well with the GCMT south-dipping focal solution (N59E, 64S) and distributions of aftershocks analyzed through the double-difference method [*Bannister et al.*, 2011]. The slip model suggests peak slip

of 2.1 m with the main rupture area occurring between 2 and 11 km and has a moment magnitude M_w 6.4 (Figure 4.5B). Some very shallow slip is observed in the model, although this region corresponds to areas offshore where no geodetic data is available and is probably an artifact of the inversion. Our slip model supports the ground and pixel-offset observations of no surface rupture during the Christchurch earthquake; however, data gaps in the InSAR observations within the city of Christchurch may inhibit our inversions from inferring any slip at the surface. Because only one pair of images is available to constrain slip during the 13-June event (Table 4.1, Figure 4.3C), we do not present a distributed slip model. We show the location of our best-fit single patch model in Figure 4.5C.

4.4.3 Coulomb Stress Change

In order to model the potential effects of static Coulomb stress change of the Darfield earthquake on the 22-Feb Christchurch earthquake, we use the Darfield earthquake slip distribution described above (Figure 4.5A), which predicts a static Coulomb stress change on a fault with the orientation and rake inferred for the Christchurch earthquake as shown in Figure 4.6A. In our calculation, all slip inverted for the Christchurch earthquake occurs within the region of positive Coulomb stress change (Figure 4.6A, black curve). This suggests that static Coulomb stress change from the Darfield earthquake indeed encouraged the Christchurch earthquake. Peak calculated static Coulomb stress change is 3.1 bars while the minimum is -4.5 bars.

To obtain statistics describing the significance of these inferred static Coulomb stress changes, we apply a Monte Carlo error propagation technique similar to that described in *Lohman and Barnhart* [2010]. We begin by simulating 500 noisy data sets by adding spatially

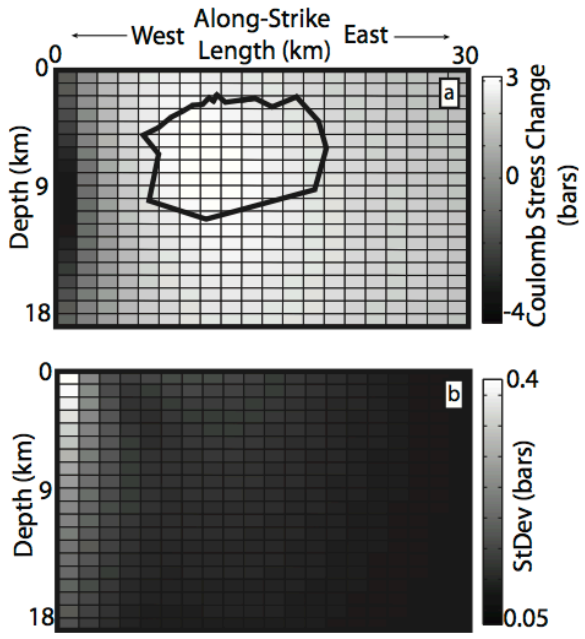

Figure 4.6: A) Static Coulomb stress change on the Christchurch earthquake fault plane predicted by the slip distribution inferred for the Darfield earthquake (Figure 4.5A). Positive Coulomb stress change encourages rupture, negative discourages rupture. Black outline shows extent of Christchurch earthquake slip with magnitude > 0.7 m(Figure 4.5B). 1σ standard deviation of static Coulomb stress change, calculated using 500 realizations of the Darfield earthquake slip distribution.

correlated noise with a spatial scale of 100 km to the predicted LOS surface displacements from our best-fit slip distribution, using the same covariance as we infer from the original Darfield data. We then invert for slip on the same four-fault geometry used above for each synthetic data set. Lastly, we calculate the static Coulomb stress change on the fault geometry and slip orientation inferred for the Christchurch earthquake for each realization of the synthetic data. This method allows us to quantify errors in predicted Coulomb stress change (Figure 4.6B) induced by data noise, such as correlated atmospheric water vapor. As can be seen in Figure 4.6B, the expected variation due to these sources is far less than the inferred increase in stress resolved on the target fault plane that ruptured during the Christchurch earthquake. Other errors due to variations in fault plane geometry, crustal elastic structure, or to the contribution from the rest of the aftershock sequence likely also contribute.

4.5 Discussion

Certain attributes of this earthquake sequence suggest reactivation of poorly developed faults. A particularly interesting attribute of seismicity during the 2010–2011 Canterbury earthquake sequence is the activity of steeply dipping (>50 degrees) reverse faults. First motion focal solutions for the Darfield earthquake reveal reverse motion rupture on a steep, east-dipping plane

[*Gledhill et al.*, 2011] before slip propagated to E-W striking strike-slip faults. In addition, aftershock locations and focal mechanisms located in NE-SW trending zones at the ends and center of the Darfield rupture reveal steeply dipping reverse-motion planes, and steep reverse faults are necessary to model geodetic observations of both the Darfield [*Beavan et al. 2010*] and Christchurch earthquakes. Traditional Andersonian-style faulting predicts that faults should form at angles of ~30 degrees to the principal shortening direction [*Anderson*, 1951], which results in reverse faults dipping 30 degrees with a horizontal shortening direction and normal faults dipping 60 degrees with a vertical shortening direction. While Anderson's theory predicts the angles at which faults form relative to the local stress field, preexisting faults can reactivate and new faults will not be formed if it is energetically more favorable to slip on non-optimally oriented planes [*Anderson 1951*]. Reactivation of non-Andersonian faults is observed in numerous tectonic environments including Iran and the Aegean [*Jackson*, 1994; *Berberian*, 1995]. The steep dip of reverse faults observed in aftershock and mainshock focal mechanisms along with geodetically derived fault geometries for the Darfield and Christchurch earthquakes strongly suggest Cretaceous-Oligocene faults, formed during formation of the Torlesse terrain and later breakup of the Rangitata Orogen, were seismically reactivated during the 2010–2011 Canterbury earthquake sequence. Likewise, the high stress drops, particularly for the Darfield event, calculated for each event [*Fry and Gerstenberger*, 2011] suggest reactivation of high friction faults under low strain rates compared to faults in the Marlborough fault zone or Puysegur and Hikurangi subduction zones.

The lack of many aftershocks west of the Darfield earthquake in the Southern Alps (Figure 4.1), where thrust faults are oriented more N-S and dip at lower angles (<40 degrees)

[*Mackinnon 1983; e.g., Dorn et al. 2010*] compared to the east implies that despite non-Andersonian dips, faults active during the 2010–2011 earthquake sequence are favorably oriented for rupture within the current stress field in the Canterbury Plains. Our calculation of positive Coulomb stress change in the location of Christchurch earthquake (Figure 4.6A) implies the Darfield earthquake likely expedited the timing of the Christchurch earthquake.

4.6 Conclusions

This earthquake sequence demonstrates the need for reassessment of seismic hazards in the eastern South Island, New Zealand, through continued GPS and seismic reflection studies (such as that by Dorn *et al.* [2010]) to identify faults active in the Quaternary beneath the smooth Canterbury Plains. As noted before, the Banks Peninsula stands out conspicuously on the eastern edge of the Canterbury Plains. The location of this earthquake sequence relative to the Miocene volcanic structure suggests the structure's location may have a strong influence on stress release in this region, as also suggested by *Sibson et al.*, [2011]. Unmapped, potentially seismogenic faults may exist in association with other volcanic structures throughout the eastern South Island such as near Dunedin.

The steadily increasing availability and shortening latency time associated with optical imagery is opening up a wide range of opportunities for its use in earthquake analysis and response. Comparing sequential optical images may allow rapid mapping of landslide locations, which will be useful for future studies of strong-motion shaking and will allow hazards assessment teams to move directly to affected regions and assess local hillslope stability. Subpixel offsets from optical imagery have the potential of allowing identification of destabilized slumps that did not fully fail but may pose a significant risk of motion during

subsequent aftershocks or rainfalls. In extreme cases, these may induce further damage or local tsunamis.

The fine resolution of the optical imagery will also enable the mapping of liquefaction within the region that experienced strong shaking. Traditional mapping of the regions of liquefaction can be based on their appearance in the imagery and on regions of decorrelation in pixel offset tracking.

4.7 References

Anderson, E. M. (1951), *The dynamics of faulting and dyke formation with applications to Britain*, Oliver and Boyd.

Bannister, S., B. Fry, M. Reyners, J. Ristau, and H. Zhang (2011), Fine-scale Relocation of Aftershocks of the 22 February Mw 6.2 Christchurch Earthquake using Double-difference Tomography, *Seismological Research Letters*, *82*(6), 839–845, doi:10.1785/gssrl.82.6.839.

Barnhart, W. D., and R. B. Lohman (2010), Automated fault model discretization for inversions for coseismic slip distributions, *J. Geophys. Res.*, *115*(B10), B10419, doi:10.1029/2010JB007545.

Beavan, J. et al. (1999), Crustal deformation during 1994–1998 due to oblique continental collision in the central Southern Alps, New Zealand, and implications for seismic potential of the Alpine fault, *Journal of Geophysical Research*, *104*(B11), 25233, doi:10.1029/1999JB900198.

Beavan, J. L., L. Sasonov,, S. Wallace, S. Ellis, and N. Palmer (2010), The Darfield (Canterbury) earthquake: Geodetic observations and preliminary source model, *Bulletin of the New Zealand Society for Earthquake Engineering*, *43*(4), 228–235.

Berberian, M. (1995), Master “blind” thrust faults hidden under the Zagros folds: active basement tectonics and surface morphotectonics, *Tectonophysics*, *241*(3–4), 193–224, doi:10.1016/0040-1951(94)00185-C.

Berryman, K. R., S. Beanland, A. F. Cooper, H. N. Cutten, R. J. Norris, and P. R. Wood (1992), The Alpine Fault, New Zealand: variation in Quaternary structural style and geomorphic expression, *Annales Tectonicae*, *6*, 126–163.

Bradley, B. A., and M. Cubrinovski (2011), Near-source Strong Ground Motions Observed in the 22 February 2011 Christchurch Earthquake, *Seismological Research Letters*, *82*(6), 853–865, doi:10.1785/gssrl.82.6.853.

Cowan, H. A. (1991), The North Canterbury earthquake of September 1, 1888, *Journal of the Royal Society of New Zealand*, *21*(1), 1–12, doi:10.1080/03036758.1991.10416105.

Crippen, R. E., and R. G. Blom (1991), Measurement of Subresolution Terrain Displacements Using Spot Panchromatic Imagery, in *Geoscience and Remote Sensing Symposium, 1991. IGARSS '91. Remote Sensing: Global Monitoring for Earth Management., International*, vol. 3, pp. 1667 –1670.

Debella-Gilo, M., and A. Kääb (2011), Sub-pixel precision image matching for measuring surface displacements on mass movements using normalized cross-correlation, *Remote Sensing of Environment*, *115*(1), 130–142, doi:10.1016/j.rse.2010.08.012.

DeMets, C., R. G. Gordon, D. F. Argus, and S. Stein (1994), Effect of recent revisions to the geomagnetic reversal time scale on estimates of current plate motions, *Geophys. Res. Lett.*, *21*(20), 2191–2194, doi:10.1029/94GL02118.

Dorn, C., A. G. Green, R. Jongens, S. Carpentier, A. E. Kaiser, F. Campbell, H. Horstmeyer, J. Campbell, M. Finnemore, and J. Pettinga (2010), High-resolution seismic images of potentially seismogenic structures beneath the northwest Canterbury Plains, New Zealand, *J. Geophys. Res.*, *115*(B11), B11303, doi:10.1029/2010JB007459.

Dziewonski, A. M., T.-A. Chou, and J. H. Woodhouse (1981), Determination of earthquake source parameters from waveform data for studies of global and regional seismicity, *J. Geophys. Res.*, *86*(B4), 2825–2852, doi:10.1029/JB086iB04p02825.

Farr, T. G. et al. (2007), The shuttle radar topography mission, *Rev. Geophys.*, *45*(2), doi: 10.1029/2005RG000183.

Fialko, Y., M. Simons, and D. Agnew (2001), The complete (3‐D) surface displacement field in the epicentral area of the 1999 MW 7.1 Hector Mine Earthquake, California, from space geodetic observations, *Geophys. Res. Lett.*, *28*(16), 3063–3066, doi: 10.1029/2001GL013174.

Fry, B., and M. C. Gerstenberger (2011), Large Apparent Stresses from the Canterbury Earthquakes of 2010 and 2011, *Seismological Research Letters*, *82*(6), 833–838, doi: 10.1785/gssrl.82.6.833.

Gledhill, K., J. Ristau, M. Reyners, B. Fry, and C. Holden (2011), The Darfield (Canterbury, New Zealand) Mw 7.1 Earthquake of September 2010: A Preliminary Seismological Report, *Seismological Research Letters*, *82*(3), 378–386, doi:10.1785/gssrl.82.3.378.

Howard, M., A. Nicol, J. Campbell, and J. R. Pettinga (2005), Holocene paleoearthquakes on the strike‐slip Porters Pass Fault, Canterbury, New Zealand, *New Zealand Journal of Geology and Geophysics*, *48*(1), 59–74, doi:10.1080/00288306.2005.9515098.

Iizuka, H., Y. Sakai, and K. Koketsu (2011), Strong Ground Motions and Damage Conditions Associated with Seismic Stations in the February 2011 Christchurch, New Zealand, Earthquake, *Seismological Research Letters*, *82*(6), 875–881, doi:10.1785/gssrl.82.6.875.

Jackson, J. (1994), Active Tectonics of the Aegean Region, *Annual Review of Earth and Planetary Sciences*, *22*(1), 239–271, doi:10.1146/annurev.ea.22.050194.001323.

Jean-Philippe Avouac, F. A. (n.d.), The 2005, Mw 7.6 Kashmir earthquake: Sub-pixel correlation of ASTER images and seismic waveforms analysis, *Earth and Planetary Science Letters*, 514–528, doi:10.1016/j.epsl.2006.06.025.

King, G. C. P. (2007), 4.08 - Fault Interaction, Earthquake Stress Changes, and the Evolution of Seismicity, in *Treatise on Geophysics*, edited by Editor-in-Chief: Gerald Schubert, pp. 225–255, Elsevier, Amsterdam. [online] Available from: **http://www.sciencedirect.com/science/article/pii/B9780444527486000699** (Accessed 23 October 2012)

Lohman, R. B., and W. D. Barnhart (2010), Evaluation of earthquake triggering during the 2005–2008 earthquake sequence on Qeshm Island, Iran, *J. Geophys. Res.*, *115*(B12), B12413, doi:10.1029/2010JB007710.

Lohman, R. B., and M. Simons (2005), Some thoughts on the use of InSAR data to constrain models of surface deformation: Noise structure and data downsampling, *Geochem. Geophys. Geosyst.*, *6*(1), Q01007, doi:10.1029/2004GC000841.

Mackinnon, T. C. (1983), Origin of the Torlesse terrane and coeval rocks, South Island, New Zealand, *Geological Society of America Bulletin*, *94*(8), 967–985, doi:10.1130/0016-7606(1983)94<967:OOTTTA>2.0.CO;2.

Melkonian, A. K., M. J. Willis, M. E. Pritchard, and S. Bernstein (2009), Glacier Velocities and Elevation Change of the Juneau Icefield, Alaska, *AGU Fall Meeting Abstracts*, *-1*, 0490.

Michel, R. (2002), Deformation due to the 17 August 1999 Izmit, Turkey, earthquake measured from SPOT images, *Journal of Geophysical Research*, *107*(B4), doi:10.1029/2000JB000102. [online] Available from: **http://adsabs.harvard.edu/abs/2002JGRB..107.2062M** (Accessed 23 October 2012)

Norris, R. J., and A. F. Cooper (2001), Late Quaternary slip rates and slip partitioning on the Alpine Fault, New Zealand, *Journal of Structural Geology*, *23*(2–3), 507–520, doi:10.1016/S0191-8141(00)00122-X.

Quigley, M., R. V. Dissen, N. Litchfield, P. Villamor, B. Duffy, D. Barrell, K. Furlong, T. Stahl, E. Bilderback, and D. Noble (2012), Surface rupture during the 2010 Mw 7.1 Darfield (Canterbury) earthquake: Implications for fault rupture dynamics and seismic-hazard analysis, *Geology*, *40*(1), 55–58, doi:10.1130/G32528.1.

Rosen, P. A., S. Hensley, G. Peltzer, and M. Simons (2004), Updated repeat orbit interferometry package released, *Eos Trans. AGU*, *85*(5), 47, doi:10.1029/2004EO050004.

Sambridge, M. (1999), Geophysical inversion with a neighbourhood algorithm—I. Searching a parameter space, *Geophysical Journal International*, *138*(2), 479–494, doi:10.1046/j.1365-246X.1999.00876.x.

Sibson, R., F. Ghisetti, and J. Ristau (2011), Stress Control of an Evolving Strike-Slip Fault System during the 2010-2011 Canterbury, New Zealand, Earthquake Sequence, *Seismological Research Letters*, *82*(6), 824–832, doi:10.1785/gssrl.82.6.824.

Sutherland, R., K. Berryman, and R. Norris (2006), Quaternary slip rate and geomorphology of the Alpine fault: Implications for kinematics and seismic hazard in southwest New Zealand, *Geological Society of America Bulletin*, *118*(3-4), 464–474, doi:10.1130/B25627.1.

Timm, C., K. Hoernle, P. V. D. Bogaard, I. Bindeman, and S. Weaver (2009), Geochemical Evolution of Intraplate Volcanism at Banks Peninsula, New Zealand: Interaction Between Asthenospheric and Lithospheric Melts, *J. Petrology*, *50*(6), 989–1023, doi:10.1093/petrology/egp029.

Wallace, L. M., J. Beavan, R. McCaffrey, K. Berryman, and P. Denys (2007), Balancing the plate motion budget in the South Island, New Zealand using GPS, geological and seismological data, *Geophysical Journal International*, *168*(1), 332–352, doi:10.1111/j.1365-246X.2006.03183.x.

CHAPTER 5

ZAGROS TIME SERIES AND REGIONAL TRENDS IN ACTIVE DIAPIRISM[1]

5.1 Abstract

We construct an orogen-wide InSAR time series over the Zagros Mountains and western Markan Subduction Zone in southern Iran from 19 Envisat tracks spanning 2003–2010. We observe active salt diapirism of the infra-Cambrian Hormuz Salt at 20 locations and identify several diapirs that are not moving. All active diapirs reach the surface within the Asmari Limestone or older rock units while we do not observe any active diapirism occurring within younger exposures, reflecting a complex vertical accumulation of the basal salt and reactivation of diapirs by erosion. Diapir reactivation of this sort may be a critical factor affecting the feasibility of sequestering nuclear waste and CO_2 in evaporite sequences over geologic time scales. The distribution of active diapirism is indifferent to increases in mean elevation, suggesting a relatively uniform thickness of the Zagros Fold Belt above the basal salt with steps in topography driven by basement thickening. We do not observe aseismic uplift of anticlines because rates are likely below the detection threshold of our time series. This suggests that uplift is accommodated at small rates (<2–3 mm/yr) over numerous structures instead of focused at the deformation front.

5.2 Introduction

Interferometric Synthetic Aperture Radar (InSAR) time series techniques allow imaging of time-variable surface displacements at mm/yr resolution on a dense spatial scale [*Ferretti et*

---

[1] An edited version of this paper was published by AGU. Copyright 2012 American Geophysical Union. Barnhart, W. D., and R. B. Lohman (2012), Regional trends in active diapirism revealed by mountain range scale InSAR time series, Geophys. Res. Lett., 39, L08309.

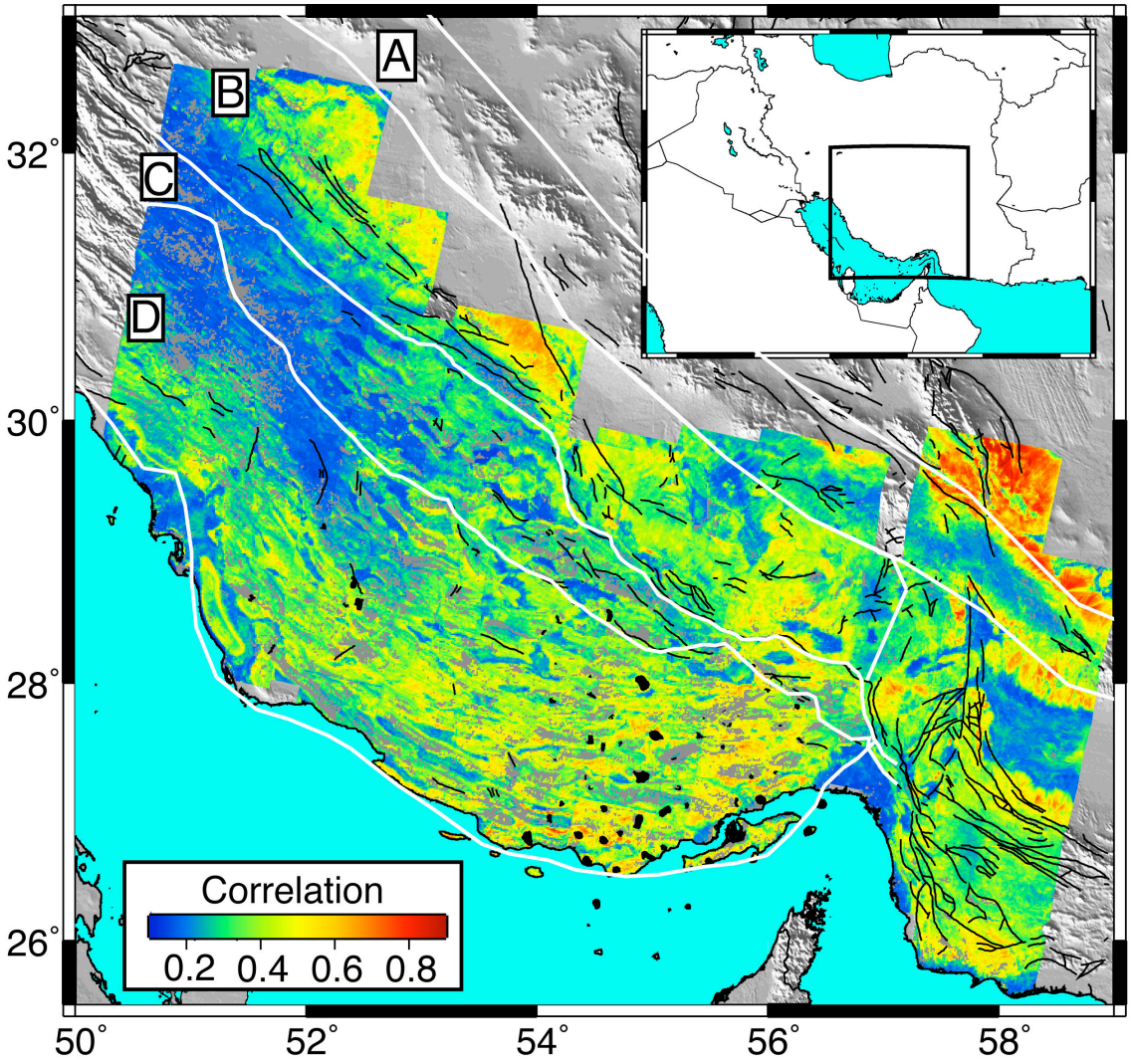

Figure 5.1: Tectonic provinces of the Zagros Mountains and mean interferogram correlation map of all descending scenes from this study over the Zagros Mountains and eastern Makran Subduction Zone, southern Iran. White outlines of provinces (modified from Alavi [1994]), A: Urumieh-Dokhtar Volcanic Belt, B: Sanandaj-Sirjan Zone, C: High Zagros, D: Active Zagros Fold and Thrust Belt (ZFTB). Black polygons are extents of surface salt exposures mapped with optical imagery. Black lines are mapped exposed faults [Huber, 1975].

al., 2001; *Berardino et al.*, 2002; *Hooper et al.*, 2004]. In this work we build an orogen-wide InSAR time series over the Zagros Mountains of southern Iran (Figure 5.1) from seven years of Envisat C-band radar acquisitions. We map the distribution of active salt diapirism, which varies in a spatially coherent manner across the mountain belt with respect to stratigraphic units, revealing a potential control on active diapirism by the level of stratigraphic exposure. Activation of diapirism by exhumation is a key consideration for the potential of evaporite units as injection

reservoirs for nuclear waste and carbon dioxide [*McEwen*, 1995; *Dusseault et al.*, 2004]. In addition to diapirism, we observe surface deformation from groundwater and hydrocarbon withdrawal and coseismic and postseismic deformation associated with earthquakes occurring during our time series, but we do not find evidence of interseismic displacements along folds or faults bounding and/or within the Zagros.

5.3 Zagros Mountains and Hormuz Diapirsm

The Zagros Mountains of southern Iran currently accommodate ~30% of the convergence between the Arabian and Eurasian plates [*Jackson and McKenzie*, 1988; *Sella et al.*, 2002; *Vernant et al.*, 2004]. Campaign GPS and seismic catalogs reveal active shortening within the Zagros Fold and Thrust Belt (ZFTB) [*Talebian and Jackson*, 2004; *Vernant et al.*, 2004] (Figure 5.1), which is a classic salt-detached fold belt overlying Precambrian crystalline basement of the Arabian shield [*Falcon*, 1974; *Stocklin*, 1974; *Davis and Engelder*, 1985]. The ZFTB is characterized by a thick (8–10 km) package of Cambrian through Recent platform and syn-orogenic sedimentary rocks that are detached from the underlying crystalline basement by the 1–2 km thick infra-Cambrian Hormuz Salt [*Falcon*, 1974; *Stocklin*, 1974; *Colman-Sadd*, 1978]. A number of controversies persist regarding the active tectonics of the Zagros, particularly with respect to the depth and lateral distribution of strain accommodation. Rare surface-rupturing earthquakes, few exposed faults, sparse GPS observations, and difficulty in seismic imaging in regions with thick evaporite layers lead to varying interpretations of deformation modes at depth, from aseismic folding of the ZFTB above Arabian basement that shortens along reactivated reverse faults [*Jackson*, 1980; *Ni and Barazangi*, 1986; *Berberian*, 1995; *Blanc et al.*, 2003; *Mouthereau et al.*, 2006] to seismically-driven shortening of the ZFTB above Arabian basement

[*Nissen et al.*, 2007, 2011; *Lohman and Barnhart*, 2010; *Roustaei et al.*, 2010]. Additionally, competing hypotheses propose strain accommodation in the ZFTB is either concentrated near the deformation front [e.g., *Oveisi et al.*, 2009] or distributed across the interior of the belt [e.g., *Costa and Vendeville*, 2002].

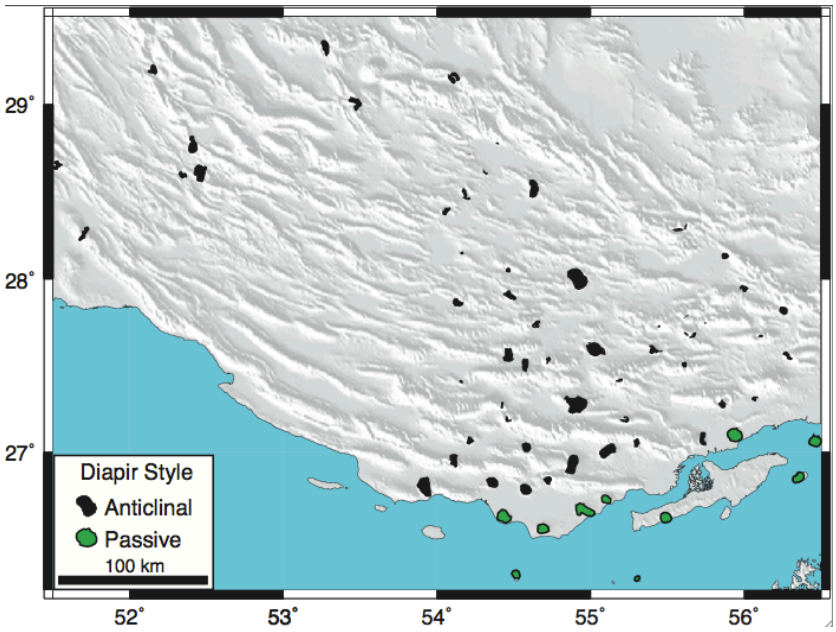

Figure 5.2: Distribution of surface diapirs categorized by style. Anticlinal diapirs are spatially related to anticlines, passive diapirs are not.

A key reason for the non-uniqueness of interpretations of shortening in the Zagros is uncertainty about the degree to which the thick Hormuz Salt and shallower salt units decouple surface and basement deformation. Weak evaporites play an important structural control in many fold and thrust belts of both tectonic and gravitational origin [*Davis and Engelder*, 1985]. Evaporites, such as halite and anhydrite, deform plastically at lower temperatures and strain rates compared to other rocks [e.g., *Hudec and Jackson*, 2007]. In diapirs, evaporites flow vertically when denser brittle overburden is reduced beyond a critical thickness and adequate evaporite material is available to source the diapir head [*Jackson*, 1995]. Conduits such as faults or accommodation spaces in fold cores, which are ubiquitous in seismically-active regions such as the Zagros, provide important pathways for vertical salt migration. Diapirs of Hormuz Salt occur at more than 100 exposures [*Kent*, 1979; *Talbot*, 1998] and are apparent in optical imagery as

surface flows and plugs (5.5c). In addition to supporting diapirism, experimental work shows the low frictional character of salt results in broad, arcuate fold belt with gentle topography [*Davis and Engelder*, 1985; *Costa and Vendeville*, 2002] in which strain accommodation is distributed throughout the belt instead of at the toe. The impermeability of salt also allows it to act as an excellent hydrocarbon trap and a potential reservoir for sequestering materials such as CO_2 and nuclear waste.

A number of studies in the Zagros highlight the history of surface motions of exposed salt flows. *Talbot et al.* [2000] used in-situ measurements to detail the flow of a salt diapir in the Kazerun strike-slip zone while *Aftabi et al.* [2010] generated a high-resolution InSAR time series of a single diapir in the eastern Zagros (Figure 5.3, ^). In both cases, the researchers found that the diapirs moved continuously with periods of enhanced surface flow caused by weakening of the surface salt by meteoric groundwater. *Jahani et al.* [2007] provide a detailed review of the Quaternary motions of most observed surface salt flows; however, many of the diapirs they classify as currently active only move after storm events and do not always show evidence for continuous motion. Our study involves two principal modes of diapirism (Figure 5.2): passive diapirs, which grow at or near the local sedimentation rate and are principally located along the coast and on offshore islands, and anticlinal diapirs, which emerge from the crests and tips of anticlines and may be controlled by different surface piercing mechanisms as described by *Hudec and Jackson* [2007].

5.4 Methods: InSAR Time Series

We construct an orogen-wide InSAR time series to constrain the spatial distribution of active salt diapirism in the Zagros Mountains (Figure 5.1). InSAR is a radar remote sensing tool

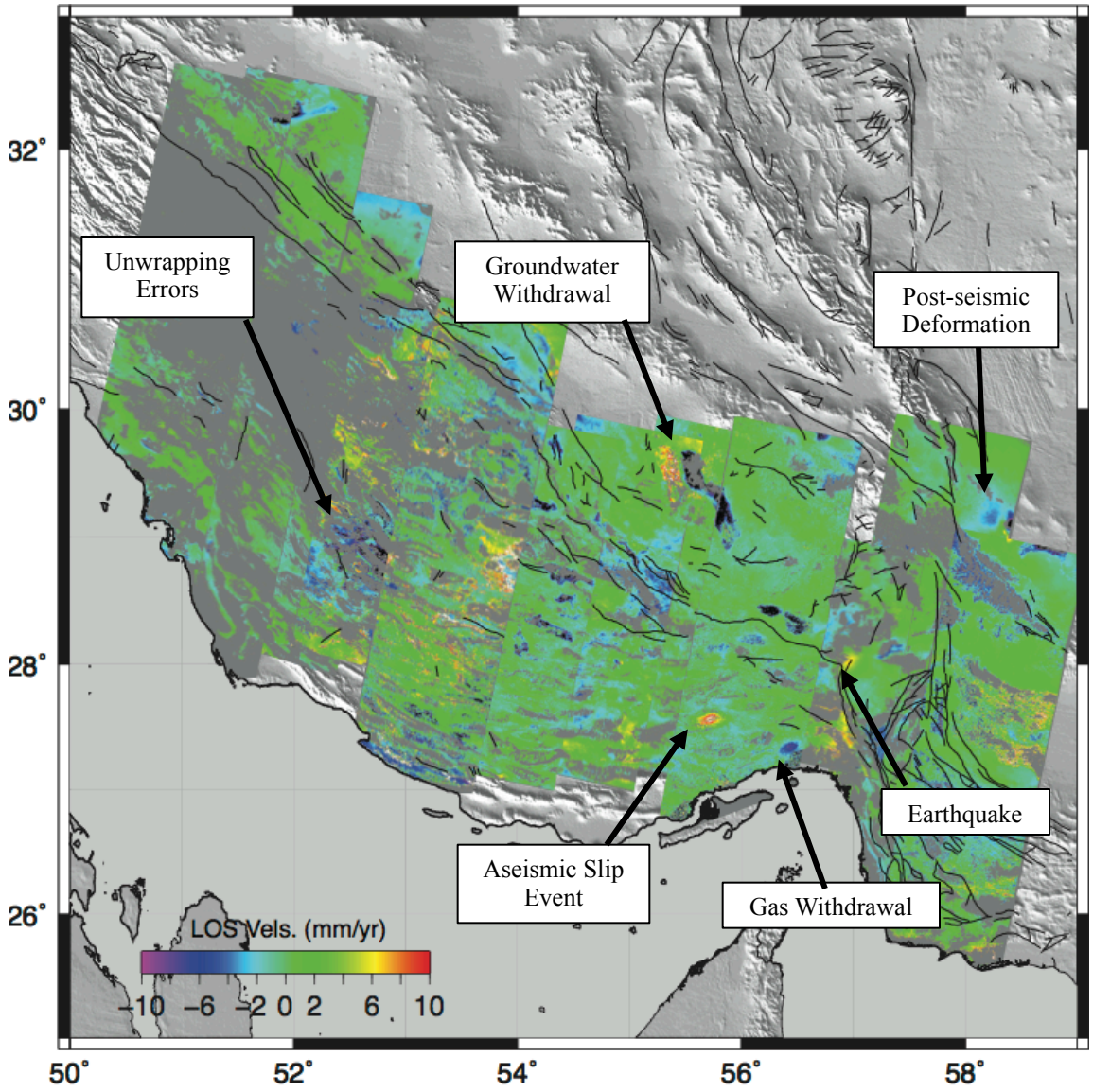

Figure 5.3 Descending LOS surface velocities annotated for different signals (color scale saturated at -10 to 10 mm/yr). Black lines are mapped surface faults (Huber 1975). Positive velocities are motion toward the satellite; negative velocities are motion away from the satellite.

that provides spatially dense measurements of surface displacements at millimeter to centimeter accuracy in the radar line of sight (LOS) [e.g., *Zebker et al.*, 1994]. In regions where multiple repeat SAR acquisitions are made, time-variable displacement can be inferred from sets of interferograms spanning a range of timespans [e.g., *Ferretti et al.*, 2001; *Berardino et al.*, 2002; *Hooper et al.*, 2004; *Fialko*, 2006]. InSAR time series techniques reduce the impact of a number of error sources including phase unwrapping errors, decorrelation, orbital baseline errors, and the

effects of signal delay through stratified atmospheric water vapor. With a large number of acquisitions (>15) in areas where the interferograms maintain coherence over the time span of available imagery, InSAR time series can constrain average surface displacement rates with accuracy better than 2–3 mm/yr over short spatial wavelengths (<25 km) [*Finnegan et al.*, 2008]. In the Zagros, gentle relief, arid climate, and slow erosion of the landscape provide excellent interferogram coherence over long spatial and temporal baselines (Figure 5.1), making the mountain belt an excellent natural laboratory for broad InSAR time series studies. We use ESA Envisat ASAR C-band radar images from the period 2003–2010 covering 19 tracks with between 14 and 47 acquisitions per track. We construct trees of interferograms with spatial baselines <500 meters and temporal baselines <5 years using the Caltech/JPL ROI_PAC software [*Rosen et al.*, 2004]. We generate individual interferograms at a resolution of 162x162 m in descending tracks (beam I2) and 157x162 m in ascending tracks (beam I6), corresponding to taking 8 looks in the range direction and 40 looks in the azimuth direction. We unwrap filtered images after masking decorrelated regions using the statistical-cost, network-flow algorithm for phase unwrapping (SNAPHU) [*Chen and Zebker*, 2001]. When we cannot unambiguously correct unwrapping errors manually, we delete that portion of the interferogram. After coregistering all interferograms to a single master, we remove a quadratic function (a ramp) from each to account for satellite orbital errors. We do not interpret any features that have a large (>50 km) spatial scale, so this step should not bias our results.

We derive time-variable displacement histories from each tree of interferograms using a methodology similar to *Berardino et al.* [2002] (Figures 5.3-5.5). When multiple interferogram subsets exist within a single tree, a situation that can occur when there are temporal and spatial

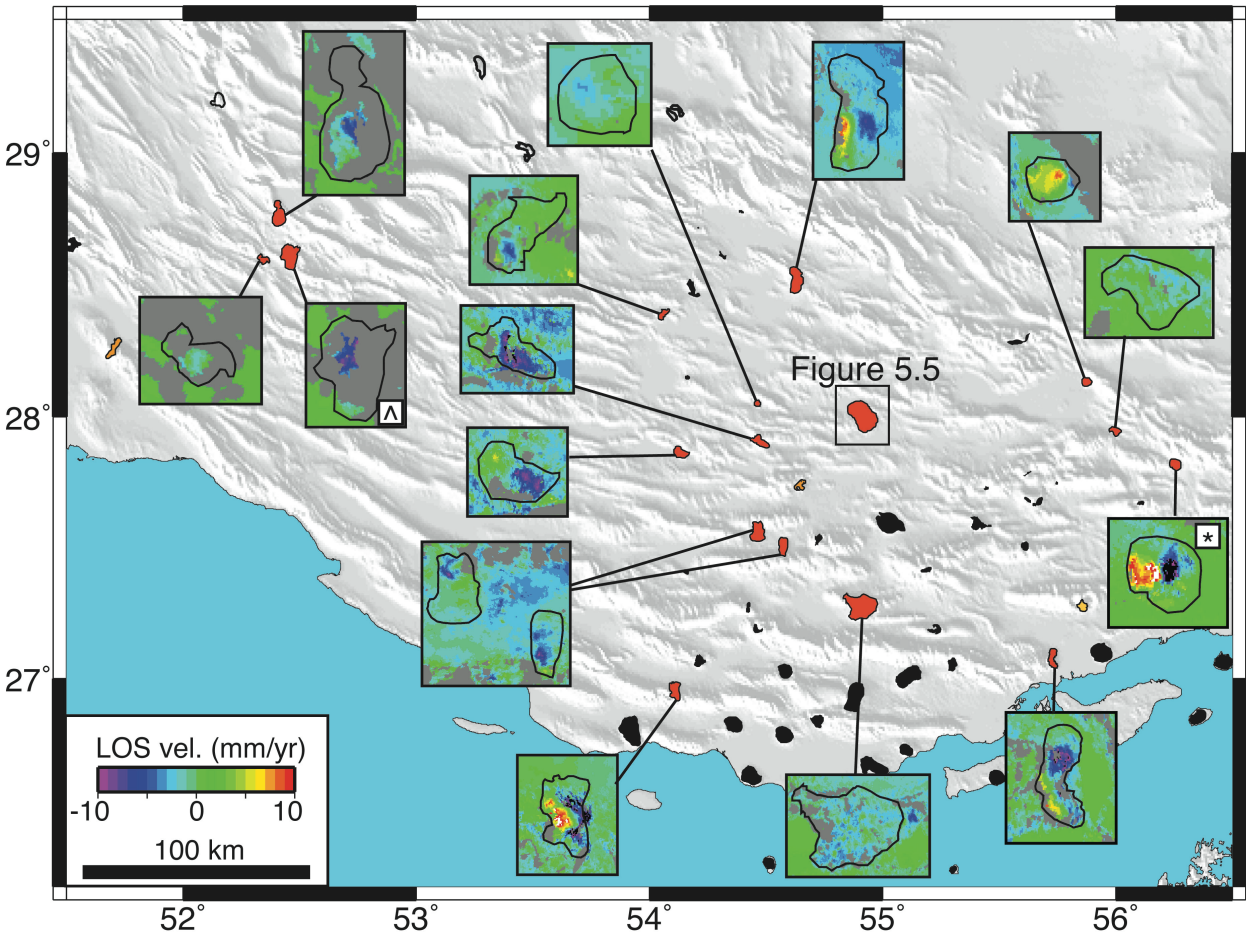

Figure 5.4: Distribution of active salt diapirs in the Zagros Mountains. Figure insets are linear rate maps from InSAR time series, saturated to the color scale -10 to 10 mm/yr. Positive is motion toward the satellite, negative is motion away from the satellite. Red polygons: Diapirs continuously active in time series. Orange polygons: Diapirs identified as active in individual interferograms but decorrelated in the full time series. Black polygons: Diapirs with well-constrained lack of surface displacements. Clear polygons: Diapirs unresolved in times series or individual interferograms. All salt diapir extents mapped with optical imagery. Diapirs studied by Talbot et al. [2000] (caret) and Aftabi et al. [2010] (asterisk) are marked.

gaps in data coverage, the inversion is poorly-posed and requires regularization. For pixels with multiple subsets, we use a damped least squares approach that drives the inversion to infer rates in the unconstrained interval that are equal to the average rate in the rest of the time series. We restrict our study to pixels where the column rank of the matrix relating displacements observed in interferograms to displacements at each acquisition is at least 80% of the full column rank. The time variable history of displacement over diapirs allows us to discern between diapirs that deform continuously throughout the observation period and those that experience episodic

deformation that may be induced by rainfall or seismic shaking. Where decorrelation or earthquakes obscure diapir signals, we also generate and inspect single interferograms from the JAXA ALOS L-band radar. The ALOS instrument provides better signal coherence in steep terrain, but acquisitions cover a much shorter time period (2006–2010) than Envisat. If the peak LOS velocities of a diapir are near the detection threshold of our time series (~3 mm/yr), we inspect a range of interferograms from the time series to verify that coherent motions are present over multiple time scales.

5.5 Results and Discussion

All diapirs we investigate can be identified in optical imagery by their morphology and generally dark color relative to their surroundings (Figures 5.5c) as well as in geologic maps [*Huber*, 1975; *Jahani et al.*, 2007]. We observe motion at 20 diapirs, all of which are anticlinal diapirs (Figure 5.4). LOS surface displacement patterns are consistent with radial spreading due to gravitationally driven flow, as observed by others (Figure 5.5) [*Talbot et al.,* 2000*; Aftabi et al.,* 2010]. Of the 20 moving diapirs, 17 deform continuously in the time series (Figures 5.5d, and 5.5e). The remaining three moving diapirs are decorrelated in the Envisat time series but show coherent motion in individual ALOS and Envisat interferograms. We attribute the decorrelation of these three diapirs to high surface velocities or steep local topography. We classify 30 diapirs, including anticlinal and passive diapirs, as “inactive” where surface displacement rates are below the detection level of our observations. The absence of resolvable surface displacements at all passive diapirs supports the observation that their deformation rates are close to local sedimentation rates, which are below our time series resolution. *Jahani et al.* [2007] classify a number of our inactive diapirs as active, but these diapirs may move only in

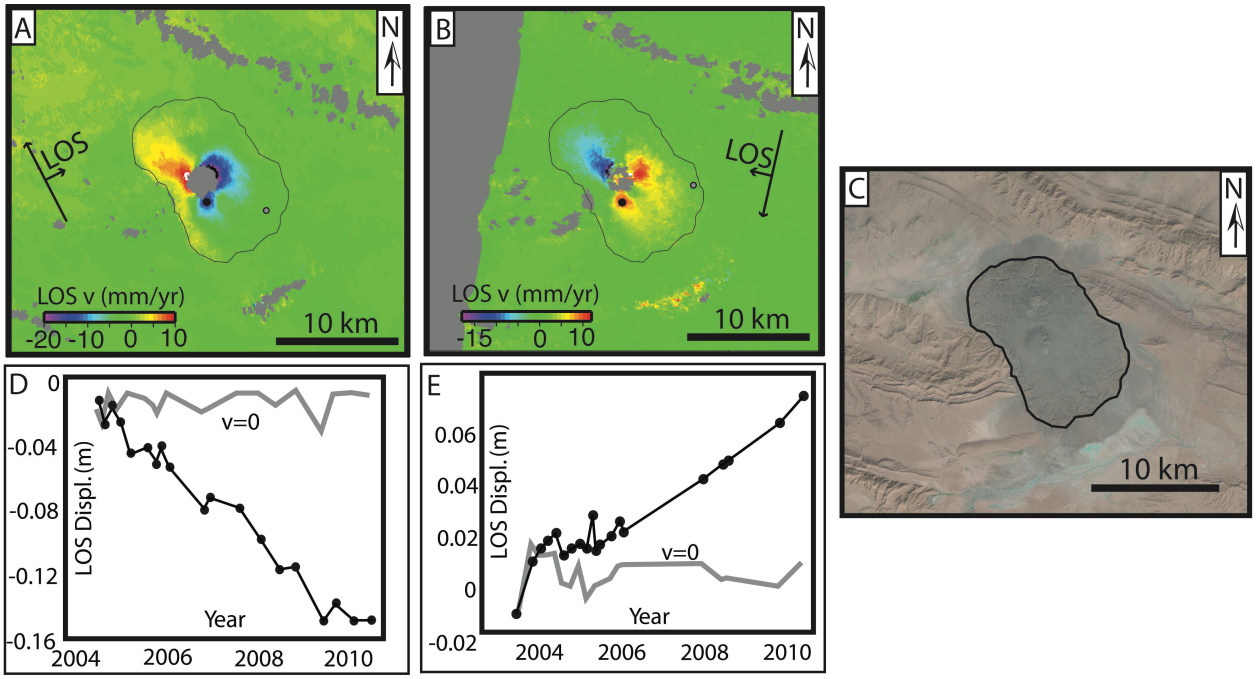

Figure 5.5: Details of a single diapir, see inset in Figure 5.4 for location. (a) Ascending track 99 linear rate map. (b) Descend- ing track 206 linear rate map. Positive is motion toward the satellite; negative is motion away from the satellite. Arrows show satellite azimuth and look direction. Positive-to-negative change across diapir reflects radial spreading from center of surface flow. (c) Landsat image of diapir (inside outline). Diapir outline mapped with optical imagery. (d, e) Time series from points within deforming region (black dot, panels a and b) and zero-velocity region (gray dots, panels a and b).

response to rain events, and may have much lower average rates. All other exposed diapirs in the Zagros are below the spatial resolution of our observations (<200 m pixels).

We observe two key trends in the distribution of active and inactive anticlinal diapirs across the Zagros with respect to exposed stratigraphy and variations in mean topography (Figure 5.6). First, all active diapirs reach the surface within the Eocene Asmari Limestone or stratigraphically lower rocks [*Huber*, 1975], while all anticlinal diapirs emerging from younger units do not demonstrate motions that are detectable in our time series. We observe the diapirs studied in detail by *Talbot et al.* [2000] and *Aftabi et al.* [2010] to deform continuously. Control of active anticlinal diapirism by the level of erosion, or erosional piercement [*Hudec and Jackson*, 2007], juxtaposed against the relative inactivity of diapirs emerging from younger rocks suggests that multiple levels of salt accumulation exist in the Zagros. This finding is also

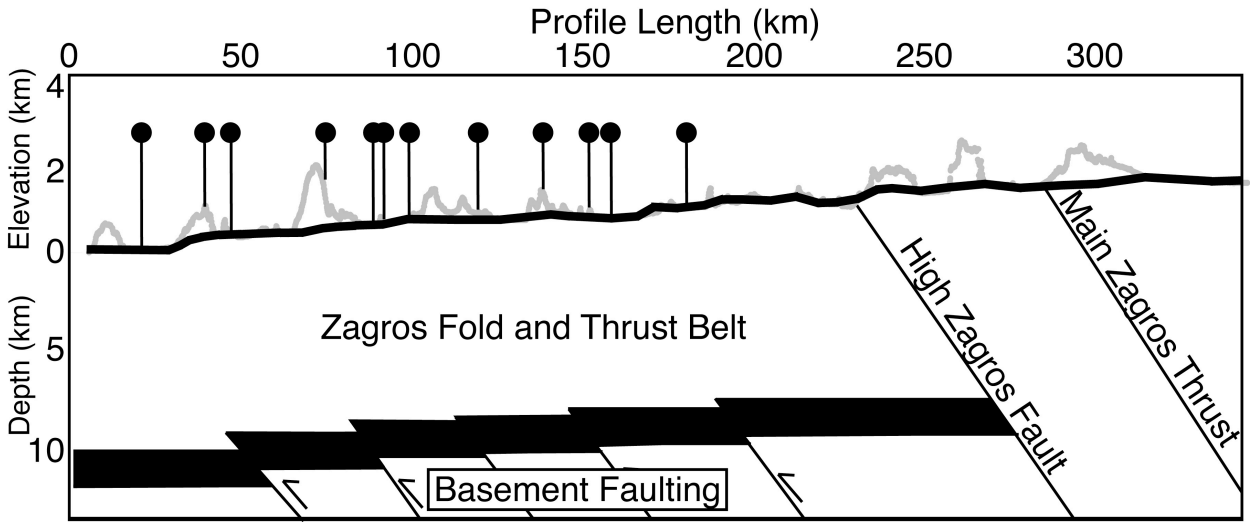

Figure 5.6: Conceptual model showing relation of basement thrusting, cover strata thickness (Zone of Folding), active diapirism, and topography. Gray profile is elevation profile perpendicular to trend of surface folds (N26.47 deg,E54.43 deg to N28.69 deg, E 55.03 deg) from SRTM DEM. Black profile is elevation profile with short wavelength (~25km) topography removed. Tadpoles are locations of active diapirs projected onto profile. Zone of folding is stratigraphic sequences above the Hormuz Salt (Black Layer). Faults are located in Arabian basement. Vertically exaggerated 10:1.

supported by seismic profiles within the region [*Jahani et al.*, 2009]. As folding and thrust faulting within the Zagros fold belt continues to evolve, the pathways sourcing now inactive diapirs from salt accumulations may have become less favorable means of releasing gravitational potential energy. Additionally activation of diapiric flow by erosion suggests salt reservoirs both in active and passive tectonic settings are not a feasible medium in which to sequester waste material over geologic time scales.

Our second observation is that active anticlinal diapirs are distributed across steps in mean topography (Figure 5.6). Previous researchers [*Berberian*, 1995; *Mouthereau et al.*, 2006] observed that topography in the Zagros occurs in two modes: short spatial wavelengths features (20–25 km across-trend) that are surface folds and long spatial wavelength features (>25 km) which, they argue, must be sustained by reverse faulting and thickening in the Arabian basement. This argument is further justified by balanced cross-sections [*Blanc et al.*, 2003; *Sherkati and Letouzey*, 2004; *Molinaro et al.*, 2005]. If the long wavelength steps corresponded to thickening

of the overburden above the basal source salt, then vertical forces induced by the additional topography would tend to preferentially drive viscous salt flow to lower elevations near the coast. Instead, our observation of active diapirism across topographic features of both short and long wavelengths is consistent with basement thickening being the primary driver for the observed steps in long wavelength topography (Figure 5.6).

In addition to salt deformation, we observe surface displacements induced by withdrawal of groundwater and hydrocarbons, as well as earthquake-related deformation (Figures 5.3). We do not observe convincing evidence of motion along the inferred range-bounding fault zones or deformation of folds other than that associated with earthquakes. The absence of detectable uplift signals on individual structures is consistent with distributed low magnitude strain accommodation across the width of the belt [e.g., *Costa and Vendeville*, 2002] in lieu of enhanced strain accommodation and uplift at the deformation front [e.g., *Oveisi et al.,* 2009]. Future missions (such as the Sentinel constellation to be launched by ESA in 2013) may provide the larger volume of data and better orbital control necessary to constrain small magnitude, regional-scale deformation signals that fall between these competing hypotheses.

5.6 References

Aftabi, P., M. Roustaie, G. I. Alsop, and C. J. Talbot (2010), InSAR mapping and modelling of an active Iranian salt extrusion, *Journal of the Geological Society*, *167*(1), 155–170, doi: 10.1144/0016-76492008-165.

Berardino, P., G. Fornaro, R. Lanari, and E. Sansosti (2002), A new algorithm for surface deformation monitoring based on small baseline differential SAR interferograms, *IEEE Transactions on Geoscience and Remote Sensing*, *40*(11), 2375 – 2383, doi:10.1109/ TGRS.2002.803792.

Berberian, M. (1995), Master “blind” thrust faults hidden under the Zagros folds: active basement tectonics and surface morphotectonics, *Tectonophysics*, *241*(3–4), 193–224, doi:10.1016/0040-1951(94)00185-C.

Blanc, E. J.-P., M. B. Allen, S. Inger, and H. Hassani (2003), Structural styles in the Zagros Simple Folded Zone, Iran, *Journal of the Geological Society*, *160*(3), 401–412, doi: 10.1144/0016-764902-110.

Chen, C. W., and H. A. Zebker (2001), Two-dimensional phase unwrapping with use of statistical models for cost functions in nonlinear optimization, *J. Opt. Soc. Am. A*, *18*(2), 338–351, doi:10.1364/JOSAA.18.000338.

Colman-Sadd, S. P. (1978), Fold development in Zagros simply folded belt, Southwest Iran, *AAPG Bulletin*, *62*(6), 984–1003.

Costa, E., and B. C. Vendeville (2002), Experimental insights on the geometry and kinematics of fold-and-thrust belts above weak, viscous evaporitic décollement, *Journal of Structural Geology*, *24*(11), 1729–1739, doi:10.1016/S0191-8141(01)00169-9.

Davis, D. M., and T. Engelder (1985), The role of salt in fold-and-thrust belts, *Tectonophysics*, *119*(1–4), 67–88, doi:10.1016/0040-1951(85)90033-2.

Dusseault, M., S. Bachu, and L. Rothenburg (2004), Sequestration of CO, *Journal of Canadian Petroleum Technology*, *43*(11), doi:10.2118/04-11-04. [online] Available from: http://www.onepetro.org/mslib/servlet/onepetropreview?id=PETSOC-04-11-04 (Accessed 24 October 2012)

Falcon, N. (1974), Zagros Mountain, Mesozoic-Cenozoic Orogenic Belts, *Geological Society, London*, *Spec. Pub. 4*, 199–211.

Ferretti, A., C. Prati, and F. Rocca (2001), Permanent scatterers in SAR interferometry, *IEEE Transactions on Geoscience and Remote Sensing*, *39*(1), 8 –20, doi:10.1109/36.898661.

Fialko, Y. (2006), Interseismic strain accumulation and the earthquake potential on the southern San Andreas fault system, *Nature*, *441*(7096), 968–971, doi:10.1038/nature04797.

Finnegan, N. J., M. E. Pritchard, R. B. Lohman, and P. R. Lundgren (2008), Constraints on surface deformation in the Seattle, WA, urban corridor from satellite radar interferometry time-series analysis, *Geophysical Journal International*, *174*(1), 29–41, doi:10.1111/j. 1365-246X.2008.03822.x.

Hooper, A., H. Zebker, P. Segall, and B. Kampes (2004), A new method for measuring deformation on volcanoes and other natural terrains using InSAR persistent scatterers, *Geophys. Res. Lett.*, *31*(23), L23611, doi:10.1029/2004GL021737.

Huber, H. (1975), Geologic map of Iran, scale 1:1,000,000, *Natl. Iran. Oil Co., Tehran*.

Hudec, M. R., and M. P. A. Jackson (2007), Terra infirma: Understanding salt tectonics, *Earth-Science Reviews*, *82*(1–2), 1–28, doi:10.1016/j.earscirev.2007.01.001.

Jackson, J., and D. McKenzie (1988), The relationship between plate motions and seismic moment tensors, and the rates of active deformation in the Mediterranean and Middle East, *Geophysical Journal*, *93*(1), 45–73, doi:10.1111/j.1365-246X.1988.tb01387.x.

Jackson, J. A. (1980), Reactivation of basement faults and crustal shortening in orogenic belts, *, Published online: 24 January 1980; | doi:10.1038/283343a0*, *283*(5745), 343–346, doi:10.1038/283343a0.

Jackson, M. P. . (1995), Retrospective salt tectonics, *Geology*, *65*, 1–28.

Jahani, S., J.-P. Callot, D. F. Lamotte, J. Letouzey, and P. Leturmy (2007), The Salt Diapirs of the Eastern Fars Province (Zagros, Iran): A Brief Outline of their Past and Present, in *Thrust Belts and Foreland Basins*, edited by O. Lacombe, F. Roure, J. Lavé, and J. Vergés, pp. 289–308, Springer Berlin Heidelberg. [online] Available from: http://www.springerlink.com/content/j667q601234037rk/abstract/ (Accessed 24 October 2012)

Jahani, S., J.-P. Callot, J. Letouzey, and D. F. de Lamotte (2009), The eastern termination of the Zagros Fold-and-Thrust Belt, Iran: Structures, evolution, and relationships between salt plugs, folding, and faulting, *Tectonics*, *28*(6), TC6004, doi:10.1029/2008TC002418.

Kent, P. E. (1979), THE EMERGENT HORMUZ SALT PLUGS OF SOUTHERN IRAN, *Journal of Petroleum Geology*, *2*(2), 117–144, doi:10.1111/j.1747-5457.1979.tb00698.x.

Lohman, R. B., and W. D. Barnhart (2010), Evaluation of earthquake triggering during the 2005–2008 earthquake sequence on Qeshm Island, Iran, *J. Geophys. Res.*, *115*(B12), B12413, doi:10.1029/2010JB007710.

McEwen, T. (1995), Selection of waste disposal sites, in *Scientific and Regulatory Basis for the Geological Disposal of Radioactive Waste*, vol. 7, pp. 201–238, John Wiley, New York.

Molinaro, M., P. Leturmy, J.-C. Guezou, D. F. de Lamotte, and S. A. Eshraghi (2005), The structure and kinematics of the southeastern Zagros fold-thrust belt, Iran: From thin-skinned to thick-skinned tectonics, *Tectonics*, *24*(3), TC3007, doi:10.1029/2004TC001633.

Mouthereau, F., O. Lacombe, and B. Meyer (2006), The Zagros folded belt (Fars, Iran): constraints from topography and critical wedge modelling, *Geophysical Journal International*, *165*(1), 336–356, doi:10.1111/j.1365-246X.2006.02855.x.

Ni, J., and M. Barazangi (1986), Seismotectonics of the Zagros continental collision zone and a comparison with the Himalayas, *J. Geophys. Res.*, *91*(B8), 8205–8218, doi:10.1029/JB091iB08p08205.

Nissen, E., M. Ghorashi, J. Jackson, B. Parsons, and M. Talebian (2007), The 2005 Qeshm Island earthquake (Iran)—a link between buried reverse faulting and surface folding in the

Zagros Simply Folded Belt?, *Geophysical Journal International*, *171*(1), 326–338, doi: 10.1111/j.1365-246X.2007.03514.x.

Nissen, E., M. Tatar, J. A. Jackson, and M. B. Allen (2011), New views on earthquake faulting in the Zagros fold-and-thrust belt of Iran, *Geophysical Journal International*, *186*(3), 928–944, doi:10.1111/j.1365-246X.2011.05119.x.

Oveisi, B., J. Lavé, P. Van Der Beek, J. Carcaillet, L. Benedetti, and C. Aubourg (2009), Thick- and thin-skinned deformation rates in the central Zagros simple folded zone (Iran) indicated by displacement of geomorphic surfaces, *Geophysical Journal International*, *176*(2), 627–654, doi:10.1111/j.1365-246X.2008.04002.x.

Rosen, P. A., S. Hensley, G. Peltzer, and M. Simons (2004), Updated repeat orbit interferometry package released, *Eos Trans. AGU*, *85*(5), 47, doi:10.1029/2004EO050004.

Roustaei, M., E. Nissen, M. Abbassi, A. Gholamzadeh, M. Ghorashi, M. Tatar, F. Yamini-Fard, E. Bergman, J. Jackson, and B. Parsons (2010), The 2006 March 25 Fin earthquakes (Iran)—insights into the vertical extents of faulting in the Zagros Simply Folded Belt, *Geophysical Journal International*, *181*(3), 1275–1291, doi:10.1111/j.1365-246X. 2010.04601.x.

Sella, G. F., T. H. Dixon, and A. Mao (2002), REVEL: A model for Recent plate velocities from space geodesy, *J. Geophys. Res.*, *107*(B4), 2081, doi:10.1029/2000JB000033.

Sherkati, S., and J. Letouzey (2004), Variation of structural style and basin evolution in the central Zagros (Izeh zone and Dezful Embayment), Iran, *Marine and Petroleum Geology*, *21*(5), 535–554, doi:10.1016/j.marpetgeo.2004.01.007.

Stocklin, J. (1974), Possible ancient continental margins in Iran, in *Geology of Continental Margins*, pp. 873–877, Springer, New York.

Talbot, C. J. (1998), Extrusions of Hormuz salt in Iran, *Geological Society, London, Special Publications*, *143*(1), 315–334, doi:10.1144/GSL.SP.1998.143.01.21.

Talbot, C. J., S. Medvedev, M. Alavi, H. Shahrivar, and E. Heidari (2000), Salt extrusion at Kuh-e-Jahani, Iran, from June 1994 to November 1997, *Geological Society, London, Special Publications*, *174*(1), 93–110, doi:10.1144/GSL.SP.1999.174.01.06.

Talebian, M., and J. Jackson (2004), A reappraisal of earthquake focal mechanisms and active shortening in the Zagros mountains of Iran, *Geophysical Journal International*, *156*(3), 506–526, doi:10.1111/j.1365-246X.2004.02092.x.

Vernant, P. et al. (2004), Present-day crustal deformation and plate kinematics in the Middle East constrained by GPS measurements in Iran and northern Oman, *Geophys. J. Int.*, *157*(1), 381–398, doi:10.1111/j.1365-246X.2004.02222.x.

Zebker, H. A., P. A. Rosen, R. M. Goldstein, A. Gabriel, and C. L. Werner (1994), On the derivation of coseismic displacement fields using differential radar interferometry: The Landers earthquake, *J. Geophys. Res.*, *99*(B10), 19617–19,634, doi:10.1029/94JB01179.

CHAPTER 6

PHANTOM EARTHQUAKES AND TRIGGERED ASEISMIC SLIP: VERTICAL STRAIN PARTITIONING DURING EARTHQUAKE SEQUENCES IN IRAN[1]

6.1 Abstract

We present evidence for significant aseismic fault slip at shallow depth above a pair of mainshock-aftershock sequences in the Zagros Mountains of Iran. The two M_w 5.9 earthquakes are each spanned by high-quality geodetic imagery and have well-recorded sequences of aftershocks that occurred beneath a salt decollement. Earlier studies of the geodetic data inferred that the mainshocks were located above the decollement, requiring a ~10km spatial separation between aftershock cluster and earthquake centroid. We find that the geodetic data simultaneously allow two slip sources of similar magnitude – one within the basement, collocated with aftershocks, and one shallow source (also equivalent to M_w 6) responsible for the primary signal apparent in the geodetic imagery. Should this phenomenon be widespread in the Zagros, it would partially explain a previously noted discrepancy between observed seismic moment release in the Zagros and current convergence rates between the Arabian and Eurasian plates.

6.2 Introduction

A key question in active tectonics is how currently observed deformation, aseismic or seismic, is accommodated across plate boundaries and contributes to seismic hazards and long-term formation of geologic structures (Jackson and McKenzie, 1988; King *et al.*, 1988; Masson *et al.*, 2005). Geodetic observations have illuminated a spectrum of episodic aseismic fault slip behavior at tectonically active boundaries (Dragert *et al.*, 2001; Fielding *et al.*, 2004; Linde *et*

[1] Accepted for publication in Geophysical Research Letters. Barnhart, W.D., R.B. Lohman, Phantom earthquakes and triggered aseismic creep: Vertical partitioning of strain during earthquake sequences in Iran.

al., 1996; Lohman and McGuire, 2007) that may contribute significantly to the strain budget in zones of continental deformation. In the Zagros Mountains of Iran, satellite-based Interferometric Synthetic Aperture Radar (InSAR) observations spanning three moderate-sized earthquakes (Figure 6.1), combined with detailed aftershock locations, provide new insight into how strain accommodation varies vertically within an actively deforming mountain belt. Here, we examine three thrust earthquakes – the 2005.11.27 Qeshm Island (M_w5.9) and 2006.03.25 Fin (M_w5.9) events in the Simply Folded Belt (SFB) and the 2006.02.28 Tiab (M_w6.0) event in the adjoining High Zagros (Figure 6.1) - where surface displacements are constrained by InSAR observations and aftershocks were recorded by temporary, densely spaced

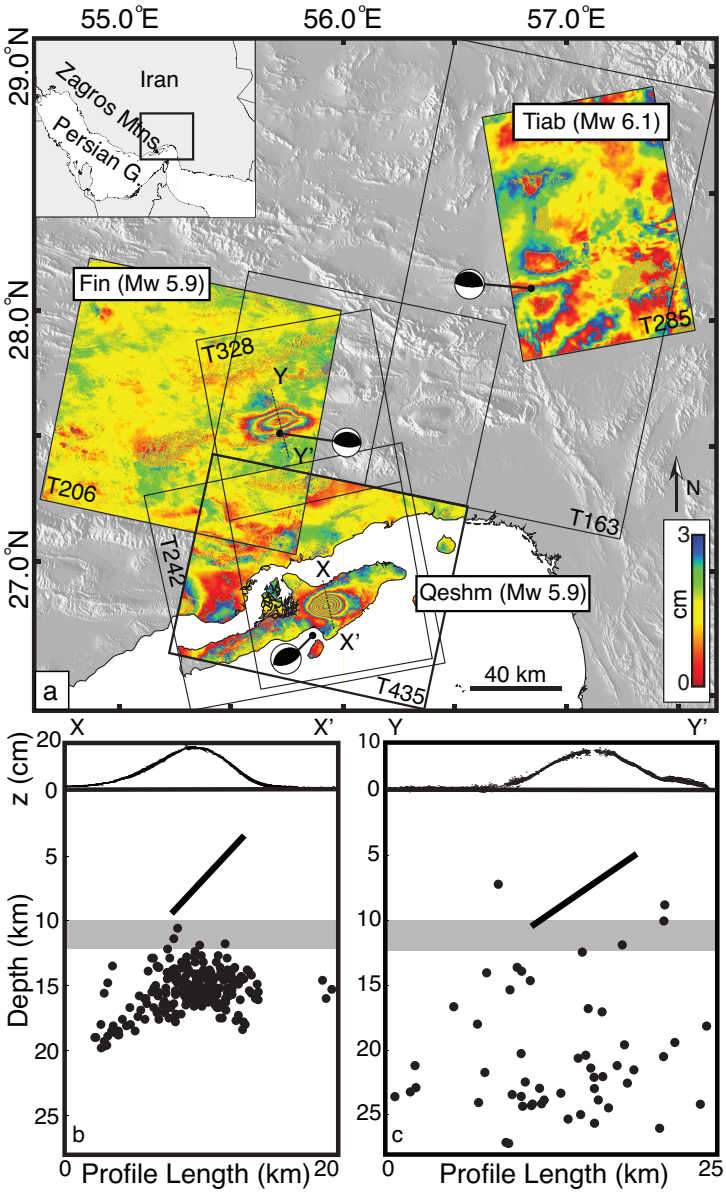

Figure 6.1: a) Location of the 2005/11/27 Qeshm, 2006/02/28 Tiab and 2006/03/25 Fin earthquakes and selected interferograms used in this study, overlain on shaded relief. Black boxes indicate SAR tracks covering each earthquake. Color cycle is wrapped line-of-sight in cm. Cross sections X-X' and Y-Y' show relationship between InSAR-modeled slip (black plane) to locally-recorded aftershocks [Nissen et al. 2010, Roustaei et al. 2010] for the a) Qeshm and b) Fin events. Data profile (z) is LOS displacement in cm. Vertical exaggeration is 1:1 for depth and horizontal scales. Details for each interferogram found in Table 6.1, Appendix A2.

Event/Date	Track	Frame	Date 1	Date 2	Bperp (m)
Qeshm	242	531	2004.07.08	2005.12.15	270
2005.11.27	328	513	2005.01.05	2005.12.21	37
	435*	3069	2005.11.24	2005.12.29	185
Tiab	163	3033/3051	2005.05.14	2006.04.29	258
2006.02.28	285*	549	2005.04.17	2006.05.07	256
Fin	206*	3051	2005.05.17	2006.05.02	1
2006.03.25	328	531	2005.05.25	2006.06.14	166
	435	3051	2005.12.29	2009.05.07	103

Table 6.1: SAR acquisitions details for all interferograms used in this study. All images are acquired by the ESA Envisat C-band SAR. Date 1 and Date 2 are pre- and post-seismic acquisitions dates. Bperp is perpendicular baseline separating satellite acquisitions. *-interferograms shown in Figure 6.1, 6.2. Track and frame spatial extents for all scenes are shown in Figure 6.1.

local seismic networks (Figure 6.2) (Gholamzadeh *et al.*, 2009; Nissen *et al.*, 2010; Roustaei *et al.*, 2010). The geodetic data for the SFB earthquakes indicate fault slip at a depth range that is significantly shallower than the depth range spanned by the aftershock cloud, although the equivalent seismic moment is similar to that detected teleseismically. We hypothesize that there are two separate deformation sources of similar magnitude for each event – one that was shallow, aseismic and that dominated the observed deformation signal, and one seismic source associated with the aftershock sequence that was deep enough to not be readily apparent in the InSAR data. We show that these results are consistent with predicted static Coulomb stress changes and regional geology.

6.3 The Zagros Mountains and Disagreement Between Data Types

The Zagros SFB is an active fold-and-thrust belt characterized by an 8-10 km thick sedimentary section that is detached from Precambrian Arabian basement by the 1-2 km thick Hormuz Salt (Alavi, 1980; Falcon, 1975). Teleseismic data and micro-earthquakes suggest that most seismicity occurs at depths of 10-25 km (Maggi *et al.*, 2000; Tatar *et al.*, 2004; Engdahl *et al.*,

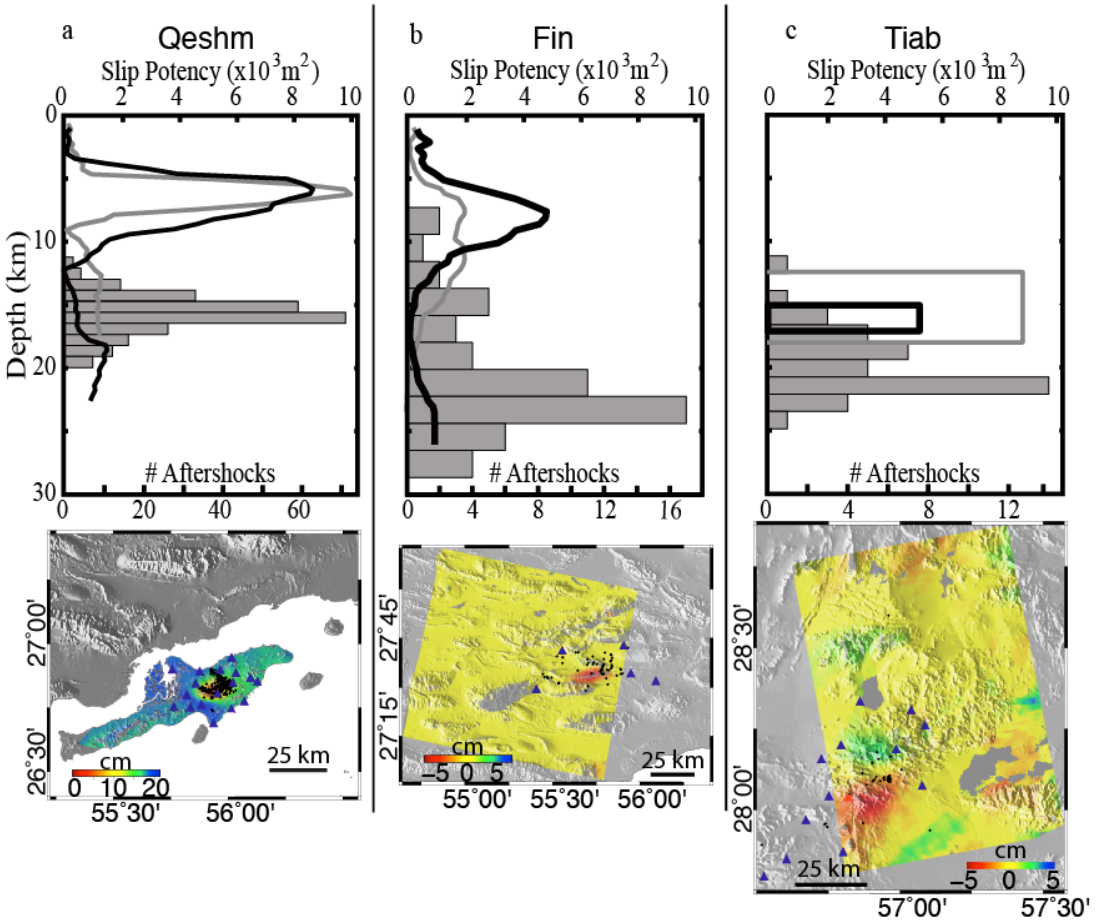

Figure 6.2: Profiles of inferred fault slip and aftershock locations [Nissen et al. 2010, Roustaei et al. 2010, Gholamzadeh et al. 2009] vs. depth for the Qeshm (a), Fin (b) and Tiab (c) earthquakes. Black and gray curves indicate slip on the fault plane with our preferred orientation and the conjugate plane, respectively. For the Tiab earthquake (c), range of slip indicates the top and bottom of fault patch with uniform slip. Gray bars indicate aftershock density. Unwrapped interferograms with aftershock (black dots) and seismometer (purple triangles) locations.

2006) within the uppermost portion of Arabian plate basement and deeper than the folded sedimentary section. Seismic moment tensors summed over the past century cannot account for the full convergence measured geodetically (Jackson and McKenzie, 1988; Masson *et al.*, 2005), implying that significant shortening in the SFB may be accommodated aseismically. The high-quality InSAR data coverage for earthquakes in the Zagros (Figure 6.1) allows reexamination of the plate motion budget and an assessment of how strain accommodation varies between the stratigraphic section and basement.

Previous studies of InSAR data spanning the 2005 Qeshm and 2006 Fin earthquakes (Lohman and Barnhart, 2010; Nissen *et al.*, 2007; Roustaei *et al.*, 2010) (Figure 6.1) inferred that coseismic slip was restricted to the sedimentary section between 3-10 km (Figure 6.2). The available SAR imagery (Table 6.1) brackets a short (weeks) time interval for the Qeshm earthquake, and a longer (months) range for the Fin event. In these two examples, inferred fault slip does not overlap with the depth range of aftershocks (10-30 km) recorded by local arrays deployed days after each event (Nissen *et al.*, 2007; Roustaei *et al.*, 2010) or micro-earthquakes recorded in the region (Tatar *et al.,* 2004). Detailed teleseismic body wave modeling of each mainshock is consistent with centroid depths within either the basement or sedimentary section (Nissen *et al.*, 2007; Roustaei *et al.*, 2010, Engdahl *et al. 2006*), as has been found elsewhere for earthquakes of similar size (Devlin *et al.*, 2012). Although aftershocks generally fill a region several times larger than the area that ruptured coseismically, the highest density of aftershocks is usually closely associated with the ruptured region itself – a relationship that is violated if the Qeshm and Fin coseismic ruptures are located in the sedimentary section. For this reason, we examine the possibility that the mainshock did occur in the basement for which the resulting deformation signals are too broad and low-magnitude to be apparent in the InSAR data

6.4 Fault Slip Resolution

We explore the significance of the apparent separation of mainshock and aftershocks for the Fin and Qeshm earthquakes by reproducing the inversions of the available InSAR data while also examining the sensitivity of the InSAR to fault slip at the depths spanned by the aftershocks. For each event, we generate interferograms using Envisat ASAR images acquired by ESA (Figure 6.1, Table 6.1). We use the JPL/Caltech ROI_PAC software package (Rosen *et al.*, 2004) and the

Model	Lon (deg)	Lat (deg)	Depth (km)	Strike (deg)	Dip (deg)	Rake (deg)	Mw
2005.11.27 Qeshm							
BL-North	55.91	26.88	3.5-9.5	264	47	68	6.1
BL-South	55.95	26.8	4.6-8.6	74	35	66	6.1
GCMT	55.8	26.66	12	257/86	39/51	83/96	5.9
ISC	55.83	26.75	10*	NA	NA	NA	NA
2006.02.28 Tiab							
BL-North	56.9	28.09	14.9-17.3	302	20	51	6.0
BL-South	57.01	28.08	12.2-18.2	93	71	143	6.0
GCMT	56.87	27.86	25.4	302/93	19/73	81/118	6.0
ISC	56.83	28.12	31.1	NA	NA	NA	NA
2006.03.25 Fin							
BL-North	55.7	27.58	5-10.5	252	34	105	6.0
BL-South	55.7	27.56	4.7-12	72	50	95	6.0
GCMT	55.6	27.43	14	269/97	28/63	83/93	5.9
ISC	55.7	27.55	10*	NA	NA	NA	NA

Table 6.2: Model results and locations of seismic and geodetic models. BL-North and BL-South indicate best-fit north and south dipping focal planes from InSAR inversions, GCMT is Global CMT, ISC is International Seismological Centre. Depth values of slip inversions indicated depth range of primary slip. Lon/Lat of geodetic inversions indicates epicentral (center of slip patch with largest slip magnitude) projection of slipping area. *-Fixed value

90m resolution Shuttle Radar Topography Mission digital elevation model (Farr *et al.*, 2007). We use a spatial resolution of ~31x55m then estimate interferogram noise structure and downsample the resulting interferograms from ~10^6 pixels to a computationally manageable ~10^2 pixels using a model resolution-based quadtree method (Lohman and Simons, 2005) (Figures S1-S3, Tables S3-S5).

To determine a best-fit fault geometry for each observed deformation signal (Table 6.2), we first invert the interferograms spanning each event for the geometry of a single rectangular fault plane with uniform slip (Okada, 1992) varying strike, dip, slip direction, hypocentral location,

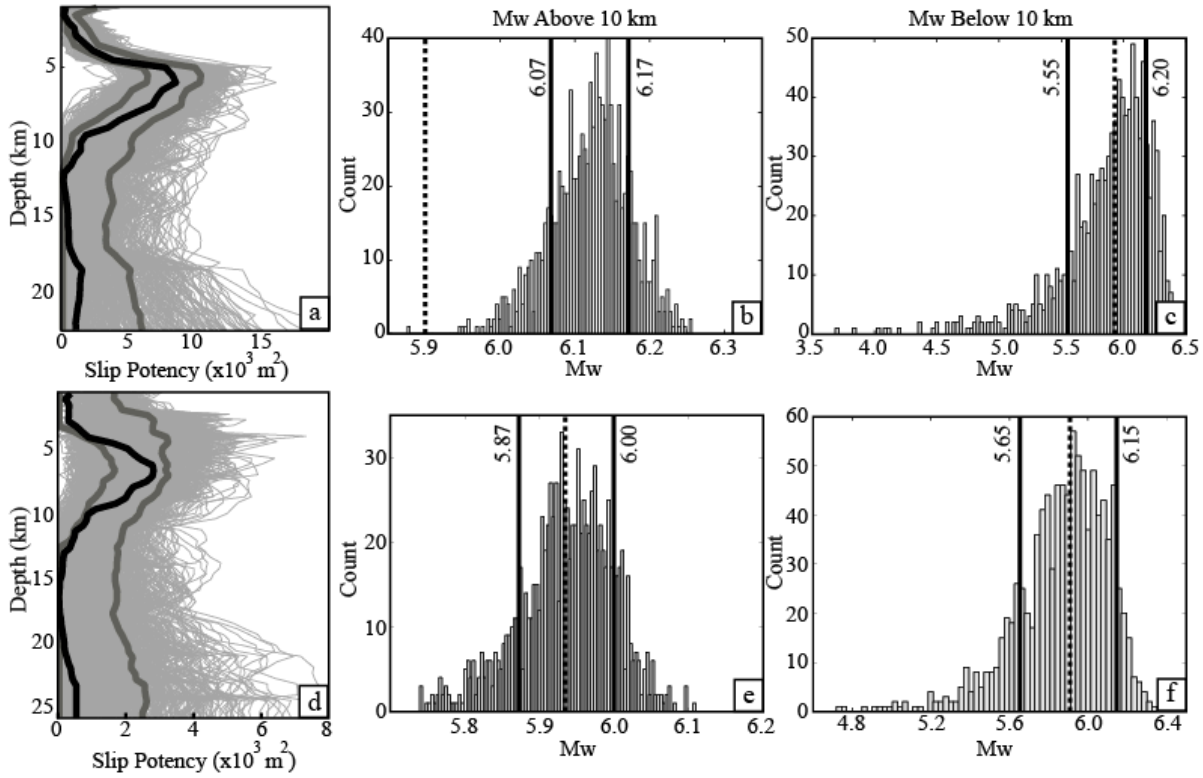

Figure 6.3: Best-fit slip distribution (black), models resulting from our Monte Carlo tests (thin gray lines), and associated error bounds (heavy gray lines) for the Qeshm (a) and Fin (d) events (Figure 2a,b). Error bounds are non-Gaussian and contain the 16th to 84th percentile of slip models for each depth. Histograms of moment magnitude for slip above (b, e) and below (c, f) 10 km indicate that error bounds on moment (black lines) bracket the Global CMT moment of 5.9 (dashed line) for the lower section of the fault.

fault length, and fault width using the Neighborhood algorithm (Sambridge, 1999). We cannot discriminate within error between the two potential nodal planes, so we consider two planes for each event in our conclusions. For the Fin and Qeshm events, which have relatively complicated surface deformation signatures, we fix the fault geometry to that of the best-fit fault patch with uniform slip and extend the fault both along-strike and down-dip so that a distributed slip inversion does not produce artifacts from interactions with the edges of the model. We then discretize the fault model with triangular dislocations (Meade, 2007) whose size varies with model resolution (Barnhart and Lohman, 2010), and invert for the best-fit slip distribution. We impose non-negative slip constraints and fix the rake to that from the uniform slip inversion. We

find that fixing the rake does not produce a noticeably different slip solution than when we allow rake to vary freely.

In general, the resolution of geodetic inversions decreases with distance from the data (in this case, depth below the surface). We perform Monte Carlo sensitivity tests that constrain the appropriate error bounds on our inferred slip models due to noise in the data (Figure 6.3). During the inversion, we pre-weight the Green's functions and displacement vectors by the inverse of the Cholesky factorization of the data covariance [*Harris and Segal,* 1987, *Barnhart and Lohman,* 2010], resulting in data that should contain noise with uniform unit variance. We generate 1000 noisy data sets by adding random noise to the displacement field predicted by our best-fit slip distribution. We then invert each noisy dataset for the best-fit slip distribution using the same fault plane parameterization and regularization as we used to invert the real data. From this population, we assess the 1-sigma error bounds on the magnitude of slip that occurs above and below different depth cutoffs (Figure 6.3), allowing us to estimate the magnitude of slip that could occur below a cutoff depth of 10km. For both the Qeshm and Fin earthquakes, we find that earthquakes with the observed Global CMT magnitudes of M_w 5.9 at 10-22 km – the depths of aftershocks – are permissible given the level of noise in the InSAR data [*Lohman and Simons*, 2005]. Our tests do not account for the contribution from errors in crustal elastic parameters, non-planar fault geometries, etc. Accounting for these errors would tend to increase the range of possible slip values - making it even more likely that the earthquakes could "hide" at depth.

The 2006 Tiab earthquake (Figure 6.1), located outside the salt-dominated SFB, provides a counter example and does not share the apparent separation of aftershocks and mainshock when we compare geodetic and seismic data. Inversions of the InSAR observations produce

fault slip within the depth ranges of locally recorded aftershocks (Figure 6.2c) (Gholamzadeh *et al.*, 2009), consistent with the behavior of typical mainshock-aftershock sequences. The collocation of InSAR-derived slip models and aftershock locations for the Tiab earthquake suggests that the separation observed in the SFB is not simply an artifact of our approach and is likely due to differences in behavior between the two regions.

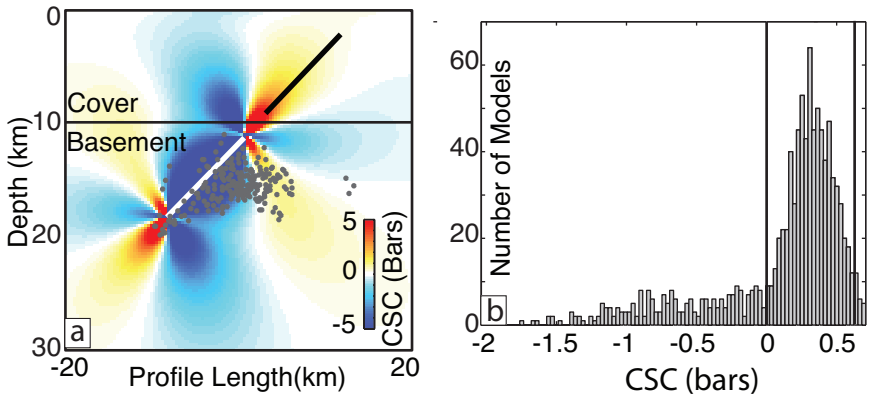

Figure 6.4: Predicted Coulomb stress change [Toda et al. 2005] for a basement earthquake (white plane) beneath a receiver fault in the stratigraphic section (black plane). Dots are recorded aftershocks [Nissen et al. 2010]. (b) Range of predicted static Coulomb stress change values at the location of InSAR-inferred aseismic slip based on 1000 potential mainshock ruptures within the basement. Values are the mean Coulomb stress change from the principal slip region in of the 2005/11/27 Qeshm earthquake. Vertical bars are 1-sigma bounds on Coulomb stress change.

6.5 Discussion

From these observations, we find that the InSAR and aftershock data for the Fin and Qeshm events are each consistent with two slip sources: One shallow source within the sedimentary section, and one deeper source within the basement. Because the deep sources are collocated with aftershocks in the basement, we infer that the deep sources are the coseismic ruptures recorded teleseismically. This removes the necessity to explain an extraordinary lack of aftershocks near the coseismic rupture. Furthermore, coseismic rupture in the basement is more consistent with perceived ground motions, which were initially over predicted by a seismic source within the sedimentary section, during the Qeshm Island earthquakes (Jaiswal *et al., 2009*).

We infer that the coseismic rupture in the basement induced aseismic fault slip within the sedimentary section, resulting in the primary signal apparent in the InSAR observations. Laboratory experiments on halite layers within sandstone produce both stick-slip behavior and ductile flow when an abrupt stress change is imposed (Shimamoto and Logan, 1986; Shimamoto, 1986). These experiments indicate that salt present along fault zones throughout the SFB (Jahani *et al.*, 2009) may permit triggered aseismic slip when exposed to stress changes of the sort considered here. Furthermore, predicted static Coulomb stress changes (King, 2009; Lin and Stein, 2004) for an earthquake occurring within the cloud of basement aftershocks and with the mechanism reported by the Global CMT would encourage slip at the location where we infer shallow aseismic creep (Figure 6.4).

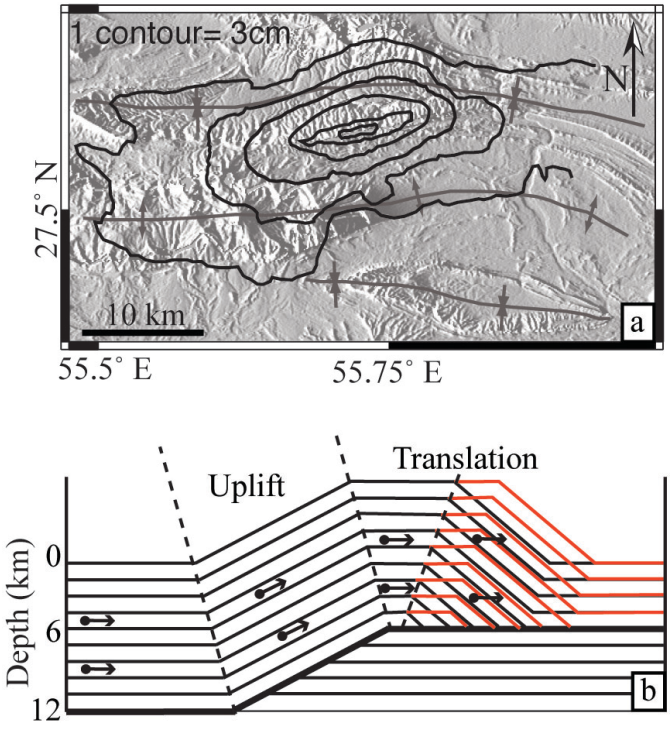

Figure 6.5: (a) Contours (2 cm intervals) of line-of-sight deformation (primarily vertical, uplift) spanning the Fin earthquake. Map symbols indicate anticlinal and synclinal crests interpreted from optical imagery and DEM by the authors. (b) Conceptual model of a fault-bend-fold with fault displacement in the inferred depth range of the Fin event. Arrows indicate predicted directions of particle motion. Heavy line indicates region of aseismic slip. Uplift is observed in InSAR, horizontal motions are inferred by the model but cannot be constrained by the data.

Additionally, the observed surface deformation during the Fin aseismic slip event is consistent with the long-term evolution of the individual folds (Figure 6.5). The line-of-sight uplift observed during the Fin sequence occurs primarily on the dipping limb of a fold identified

in optical imagery and digital elevation models (Figure 6.5a) and is consistent with fault-bend folding inferred elsewhere in the SFB (Burberry et al. 2008). Kinematic fault-bend fold models predict that, in a mature fold where total accumulated slip exceeds the width of the ramp, slip on the dipping ramp produces uplift of the limb above the ramp alone (Figure 6.5b), whereas fault-propagation and detachment fold models would predict uplift at the crest (Suppe, 1983). The Hormuz Salt (~11-12km) and shallower (3-4 km and ~6 km) evaporite and shale horizons (Jahani *et al.*, 2009; Sherkati *et al.*, 2005) bracket the inferred depths of the Fin aseismic slip event, which is consistent with shallow active detachments (Figure 6.5b). Earthquake-related fold shortening has been inferred for the 2005 Qeshm event (*Nissen et al.*, 2007) and elsewhere for other events, including the 1980 Algerian earthquake (*King and Vita-Finzi*, 1981) and the 1983 Coalinga earthquake (e.g. *Hill*, 1984; *Stein and Ekström*, 1992).

The data used in this study place no constraint on the geometric relationship between faults in the basement and sedimentary section or the processes by which slip is transferred through the intervening Hormuz Salt. While salt at 10-12km depth is likely to behave ductilely at longer timescales, it behaves elastically at short timescales (seconds) and perhaps can sustain the static coseismic Coulomb stress change long enough to initiate aseismic deformation in the sedimentary layers above it. Alternatively, the convergence history between Arabia and Eurasia may have resulted in basement relief that allows direct coupling between a single fault in the basement and the upper cover rocks. These questions may be resolved when we have further knowledge of the exact geometry of the two slip sources or the character of interseismic deformation associated with the fold belt. Where sufficient data exists, InSAR time series analysis can have sub-mm/yr detection thresholds (e.g., Finnegan *et al.,* 2008), suggesting that

future InSAR missions with frequent "background" acquisitions may allow us to resolve the timing between coseismic rupture and triggered aseismic slip.

This work shows that aseismic shortening in mountain belts such as the Zagros occurs, at least in part, episodically as seismically triggered, aseismic events. The inferred aseismic deformation accompanying the Fin and Qeshm earthquakes is equivalent to, if not greater than, the magnitude of the coseismic deformation (Figure 6.3, Table 6.2). Accordingly, the aseismic deformation may effectively double the moment release during each earthquake sequence. This indicates that a significant portion of the inferred seismic deficit (Jackson and McKenzie, 1988; Masson *et al.*, 2005) is accommodated over short periods (days to weeks) following earthquakes rather than through steady interseismic motion.

6.6 References

Alavi, M. 1980, Tectonostratigraphic evolution of the Zagrosides of Iran, *Geology*, **8**(3), 144–149.

Barnhart, W., and R. Lohman 2010, Automated fault model discretization for inversions for coseismic slip distributions, *J. Geophys. Res.*, **115**(B10), B10419.

Burberry, C.M, Cosgrove, J.W. & Liu, J-G., 2008, Landform morphology and drainage pattern characteristics as an indicator of fold type in the Zagros Simply Folded Belt, Iran. , Journal of Maps, v2008, 417-430.

Devlin, S., B. L. Isacks, M. E. Pritchard, W. D. Barnhart, and R. B. Lohman 2012, Depths and focal mechanisms of crustal earthquakes in the central Andes determined from teleseismic waveform analysis and InSAR, *Tectonics*, **31**.

Dragert, H., K. Wang, and T. S. James 2001, A silent slip event on the deeper Cascadia subduction interface, *Science*, **292**, 1525–1528.

Engdahl, E. R., J. A. Jackson, S. C. Myers, E. A. Bergman, and K. Priestley 2006, Relocation and assessment of seismicity in the Iran region, *Geophys. J. Int.*, **167**(2), 761–778.

Falcon, N. L. 1975, From Musandam to the Iranian Makran, *The Geographical Journal*, **141**(1), 55–59.

Farr, T. G. *et al.* 2007, The Shuttle Radar Topography Mission, *Reviews of Geophysics*, **45**(2).

Fielding, E. J., T. J. Wright, J. Muller, B. E. Parsons, and R. Walker 2004, Aseismic deformation of a fold-and-thrust belt imaged by Synthetic Aperture Radar Interferometry near Shahdad, Southeast Iran, *Geology*, **32**(7), 577–580.

Finnegan, N. J., M. E. Pritchard, R. B. Lohman, and P. R. Lundgren 2008, Constraints on deformation in the Seattle, WA, urban corridor from satellite radar interferometry time-series analysis, *Geophys. J. Int.,* **174**, 29-41.

Gholamzadeh, A., F. Yamini-Fard, K. Hessami, and M. Tatar 2009, The February 28, 2006 Tiab earthquake, M-w 6.0: Implications for tectonics of the transition between the Zagros continental collision and the Makran subduction zone, *Journal of Geodynamics*, **47**(5), 280–287.

Hill, M. L. (1984), Earthquakes and folding, Coalinga, California, *Geology*, *12*(12), 711–712, doi:10.1130/0091-7613.

Jackson, J., and D. McKenzie 1988, The relationship between plate motions and seismic moment tensors, and the rates of active deformation in the Mediterranean and Middle East, *Geophys. J. Int.*, **93**(1), 45–73.

Jahani, S., J.-P. Callot, J. Letouzey, and D. F. de Lamotte 2009, The eastern termination of the Zagros Fold-and-Thrust Belt, Iran: Structures, evolution, and relationships between salt plugs, folding, and faulting, *Tectonics*, **28**, 22 PP.

Jaiswal, K. S., J. D. Wald, P. S. Earle, K. A. Porter, and M. Hearne (2009), Earthquake casualty models within the USGS Prompt Assessment of Global Earthquakes for Response (PAGER) System, *International Workshop on Disaster Casualties*, *2*.

King, G. 2009, Fault interaction, earthquake stress changes, and the evolution of seismicity, in *Earthquake Seismology*.

King, G. C. P., and C. Vita-Finzi (1981), Active folding in the Algerian earthquake of 10 October 1980, *, Published online: 02 July 1981; | doi:10.1038/292022a0*, *292*(5818), 22–26, doi: 10.1038/292022a0.

King, G. C. P., R. S. Stein, and J. B. Rundle 1988, The Growth of Geological Structures by Repeated Earthquakes 1. Conceptual Framework, *J. Geophys. Res.*, **93**(B11), 13307-13,318.

Lin, J., and R. S. Stein 2004, Stress triggering in thrust and subduction earthquakes, and stress interaction between the southern San Andreas and nearby thrust and strike-slip faults, *J. Geophys. Res*., **109**.

Linde, A. T., M. T. Gladwin, M. J. S. Johnston, R. L. Gwyther, and R. G. Bilham 1996, A slow earthquake sequence on the San Andreas fault, *Nature*, **383**, 65–68.

Lohman, R. B., and J. J. McGuire 2007, Earthquake swarms driven by aseismic creep in the Salton Trough, California, *J. Geophys. Res.*, **112**(B4).

Lohman, R. B., and M. Simons 2005, Some thoughts on the use of InSAR data to constrain models of surface deformation: Noise structure and data downsampling, *Geochem. Geophys. Geosyst*, **6**(1), 12.

Lohman, R., and W. Barnhart 2010, Evaluation of earthquake triggering during the 2005–2008 earthquake sequence on Qeshm Island, Iran, *J. Geophys. Res.*, **115**(B12), B12413.

Maggi, A., J. A. Jackson, K. Priestley, and C. Baker 2000, A re-assessment of focal depth distributions in southern Iran, the Tien Shan and northern India: do earthquakes really occur in the continental mantle?, *Geophys. J. Int.*, **143**(3), 629–661.

Masson, F., J. ChÈry, D. Hatzfeld, J. Martinod, P. Vernant, F. Tavakoli, and M. Ghafory-Ashtiani 2005, Seismic versus aseismic deformation in Iran inferred from earthquakes and geodetic data, *Geophys. J. Int.*, **160**(1), 217–226.

Meade, B. J. 2007, Algorithms for the calculation of exact displacements, strains, and stresses for triangular dislocation elements in a uniform elastic half space, *Computers & Geosciences*, **33**(8), 1064–1075.

Nissen, E., M. Ghorashi, J. Jackson, B. Parsons, and M. Talebian 2007, The 2005 Qeshm Island earthquake (Iran) - a link between buried reverse faulting and surface folding in the Zagros Simply Folded Belt?, *Geophys. J. Int.*, **171**(1), 326–338.

Nissen, E., F. Yamini-Fard, M. Tatar, A. Gholamzadeh, E. A. Bergman, J. R. Elliott, J. A. Jackson, and B. Parsons 2010, The vertical separation of mainshock rupture and microseismicity at Qeshm island in the Zagros Simply Folded Belt, Iran, *Earth Plan. Sci. Lett.*, **296**, 181–194.

Okada, Y. 1992, Internal deformation due to shear and tensile faults in a half-space, *Bull. Seism. Soc. Amer.*, **82**(2), 1018.

Rosen, P. A., S. Hensley, G. Peltzer, and M. Simons 2004, Updated Repeat Orbit Interferometry Package released, *EOS*, **85**(5), 47.

Roustaei, M., E. Nissen, M. Abbassi, A. Gholamzadeh, M. Ghorashi, M. Tatar, F. Yamini-Fard, E. Bergman, J. Jackson, and B. Parsons 2010, The 2006 March 25 Fin earthquakes (Iran)-insights into the vertical extents of faulting in the Zagros Simply Folded Belt, *Geophys. J. Int.*, **181**(3), 1275–1291.

Sambridge, M. 1999, Geophysical inversion with a neighbourhood algorithm: Searching a parameter space, *Geophys. J. Int.*, **138**(2), 479–494.

Sherkati, S., M. Molinaro, D. Frizon de Lamotte, and J. Letouzey 2005, Detachment folding in the Central and Eastern Zagros fold-belt (Iran): salt mobility, multiple detachments and late basement control, *Journal of Structural Geology*, **27**(9), 1680–1696.

Shimamoto, T. 1986, Transition between frictional slip and ductile flow for halite shear zones at room temperature, *Science*, **231**(4739), 711–714.

Shimamoto, T., and J. M. Logan 1986, Velocity-dependent behavior of simulated halite shear zones: An analog for silicates, *Geophysical Monograph Series*, **37**, PP. 49-63.

Stein, R. S., and G. Ekström (1992), Seismicity and geometry of a 110-km-long blind thrust fault 2. Synthesis of the 1982–1985 California Earthquake Sequence, *Journal of Geophysical Research: Solid Earth*, *97*(B4), 4865–4883, doi:10.1029/91JB02847.

Suppe, J. 1983, Geometry and kinematics of fault-bend folding, *American Journal of Science*, **283**(7), 684–721.

Tatar, M., D. Hatzfeld, and M. Ghafory-Ashtiany 2004, Tectonics of the Central Zagros (Iran) deduced from microearthquake seismicity, *Geophys. J. Int.*, **156**(2), 255–266.

CHAPTER 7

ACCOMMODATION OF ARABIAN-EURASIAN CONVERGENCE IN SOUTHERN IRAN FROM INSAR, GPS, AND SEISMOLOGY

7.1 Introduction

Observations of fault zone behaviors, including constraints on the location and magnitude of earthquakes as well as aseismic processes, play a critical role in efforts to characterize how strain is actively accommodated along plate boundaries. While hypocentral locations from seismic observations are often the primary data source used to identify regions of elevated seismogenic hazard, to quantify the seismogenic thickness of the crust, and to define geometries and locations of major faults, geodetic observations such as interferometric synthetic aperture radar (InSAR) can provide independent, spatially dense observations of earthquake ground displacements over broad areas (>100km) [e.g., *Bürgmann et al.*, 2000; *Pritchard et al.*, 2002; *Barnhart et al.*, 2011; *Devlin et al.*, 2012]. Catalogs of events observed with InSAR can allow identification of biases in global seismic catalogs due to suboptimal station distribution and unmodeled velocity structures [e.g., *Ferreira et al.*, 2011; *Devlin et al.*, 2012], providing constraints on the precision of seismically-derived source locations. In regions where substantial aseismic slip accompanies earthquake ruptures [e.g., *Barnhart and Lohman*, accepted; *Langbein et al.*, 2006; *Lohman and McGuire*, 2007], InSAR observations can illuminate how overall strain accommodation varies across the plate boundary and throughout the seismic cycle.

In this work, we examine observation of surface displacements spanning earthquakes in the Zagros Mountains and surrounding regions of southern Iran (Figure 7.1). We provide an updated catalog with slip models of deformation observed with InSAR (M_w4.8-6.5) for the period 2003-2011. We demonstrate that teleseismic earthquake locations are biased towards the

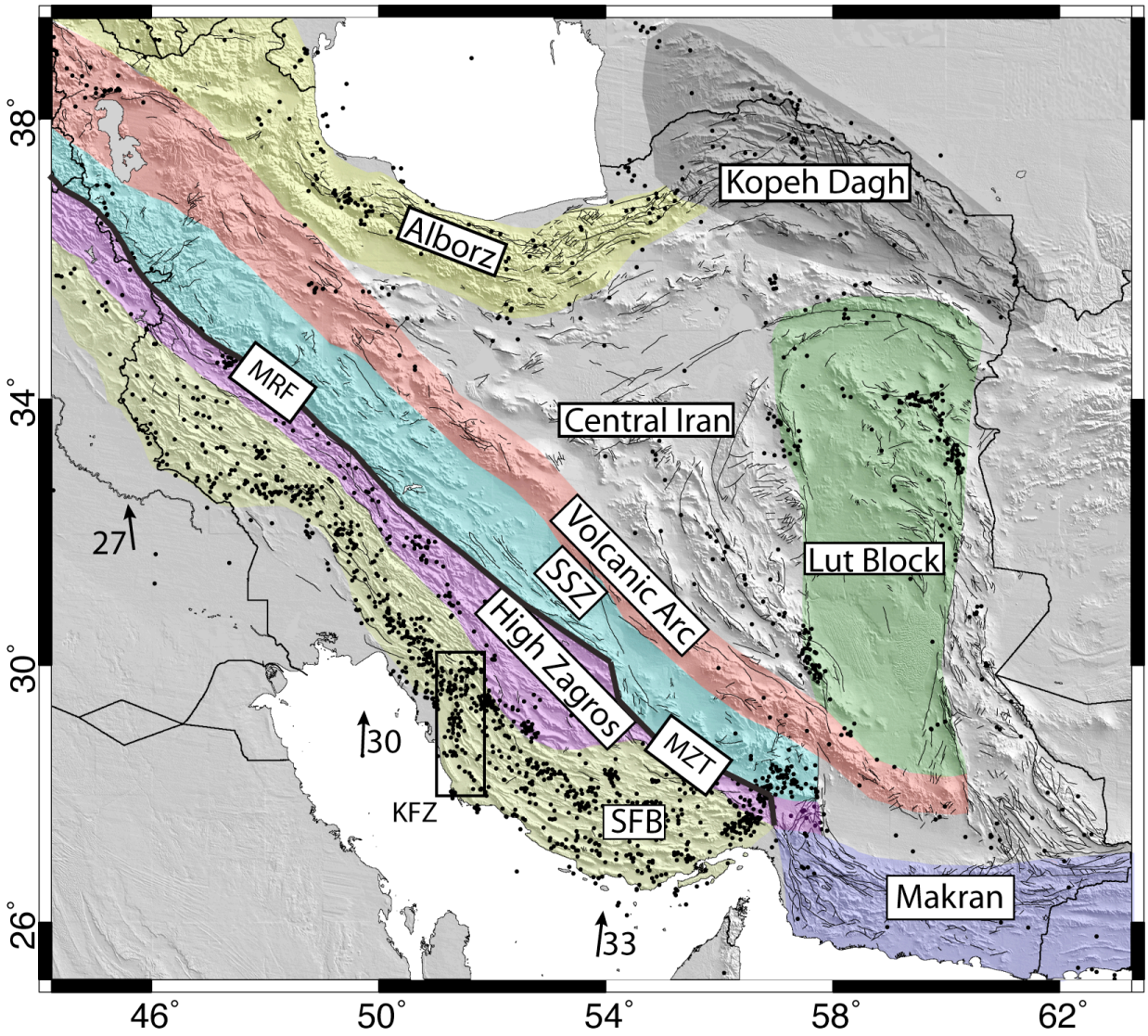

Figure 7.1: Tectonic Provinces of Iran overlain on shaded SRTM topography [*Farr et al.* 2007].. Dots are seismicity [*Engdahl et al.,* 2004], arrows indicate plate motion of Arabia relative to Eurasia in mm/yr [*DeMets et al.,* 2010]. SFB- Simply Folded Belt, SSZ- Sanandaj Sirjan Zone, MRF- Main Recent Fault, MZT - Main Zagros Thrust, KFZ - Kazerun Fault Zone. Bolded fault indicates suture between Arabia and Eurasia.

southwest in this region, likely resulting from one-dimensional approximations to the seismic velocity structure and the heterogeneous distribution of seismometers worldwide. We find that all coseismic ground displacement signals observed with InSAR within the Zagros Simply Folded Belt are consistent with fault slip within the active fold-and-thrust belt (<10 km) rather than in the underlying basement. Previous work on well-studied earthquakes within the Zagros Simply Folded Belt suggests that the observed deformation signals may be due to shallow aseismic slip

triggered by an earthquake at greater depth, with a magnitude of slip equal or greater than the coseismic slip itself [*Barnhart and Lohman*, accepted]. We argue that the primary observed coseismic geodetic signals for all events in the Simply Folded Belt may also reflect triggered aseismic fault slip above deeper earthquakes that are not well-resolved by the InSAR data. Lastly, we reassess the contributions of aseismic and seismic strain rates in the Zagros [*Jackson and McKenzie*, 1988; *Masson et al.*, 2005] to explore how these coupled earthquake-aseismic slip events would affect how long-term convergence is accommodated along this plate boundary.

7.2 Active Tectonics of Southern Iran

Convergence between the Arabian and Eurasian plates dominates the active tectonic setting of southern Iran and is accommodated in part by continental collision in the Zagros Mountains and subduction beneath the Makran accretionary Prism (Figure 7.1). North of the Makran, clockwise rotation of relatively stable blocks bounded by large strike-slip faults transfers plate motion northward (Figure 7.1). The Zagros have been described as an analog for the early stages of the more evolved Himalayan orogeny [e.g., *Ni and Barazangi*, 1986; *Hatzfeld and Molnar*, 2010]. One of the more intriguing observations about the mountain belt is that observed seismicity over the past century is far lower than what would be needed to accommodate the observed plate convergence [*Jackson and McKenzie*, 1988; *Masson et al.*, 2005].

Seismicity in the Zagros primarily occurs in the Zagros Simply Folded Belt (SFB) and the adjoining High Zagros (Figure 7.1). The SFB is a salt-detached fold-and-thrust belt wherein a thick (8-10km) package of sedimentary rocks lies above crystalline, Proterozoic Arabian shield, with an intervening 1-2km thick infra-Cambrian Hormuz Salt unit [*Falcon*, 1974; *Stocklin*, 1974; *Colman-Sadd*, 1978]. Uncertainties in teleseismic earthquake locations in this region are

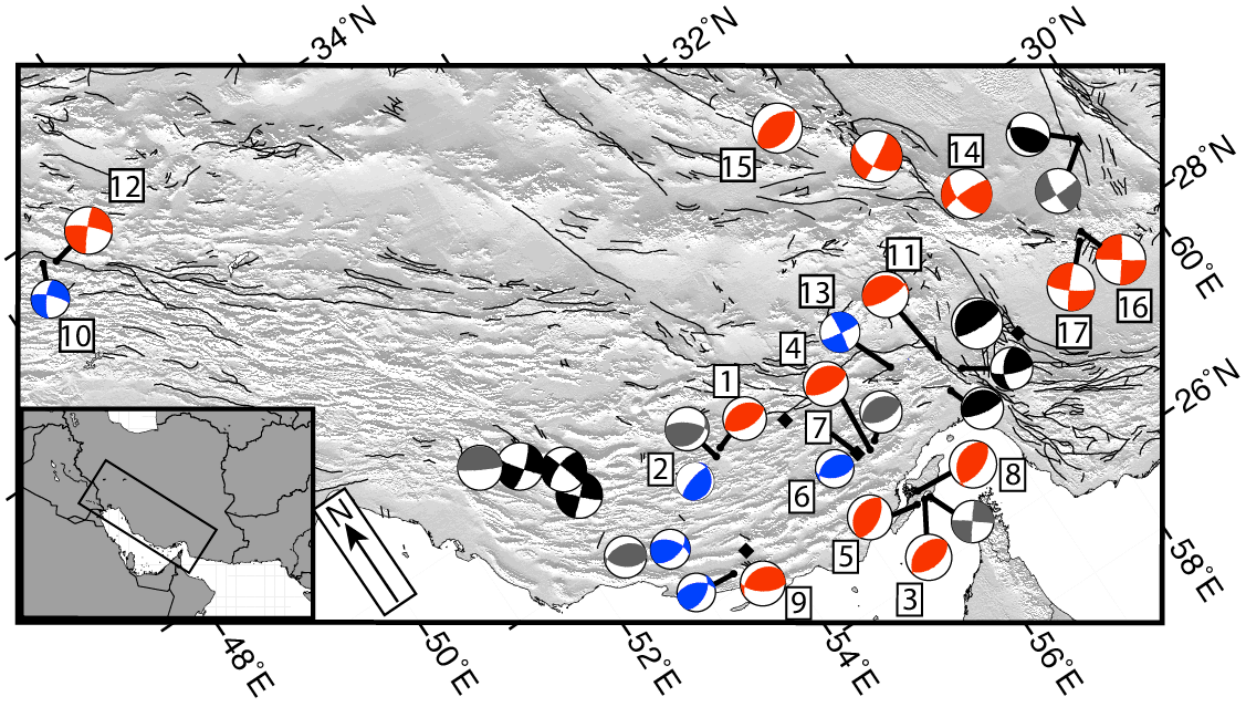

Figure 7.2: Global CMT focal mechanisms of all events >M_w5.5 in southern Iran from 1991-2011. Red events are observed with InSAR, Black event are not observed despite adequate data, gray events are unresolved due to insufficient data, blue events are observed and <M_w5.5. Numbered events occurred after 2003 and are analyzed in this paper; numbers are events IDs in Figure 7.3, Tables 7.1-7.2. Unnumbered events occurred prior to 2003 [*Fielding et al.,* 2004*, Lohman and Simons,* 2005a]. Diamonds are observed events but do not have a known focal mechanism in the GCMT catalog.

generally unable to resolve whether the events occurred in the sedimentary section or underlying crystalline basement [*Maggi et al.*, 2000; *Engdahl et al.*, 2006]. Recent geodetic work on two earthquakes (M_w5.9) combined with observations of aftershocks from dense, local seismic networks [*Nissen et al.*, 2010; *Roustaei et al.*, 2010] suggests that these events likely occurred in the crystalline basement and triggered a similar magnitude of aseismic slip in the overlying sedimentary section [*Barnhart and Lohman*, accepted]. The hypothesis that the basement deforms seismically and the cover strata deforms aseismically is further consistent with regional micro-earthquake surveys [e.g., *Tatar et al.*, 2004] and the general lack of surface rupturing earthquakes in historical records within the SFB. The triggered aseismic slip during these two events had a magnitude greater than or equal to the slip that occurred coseismically, opening up

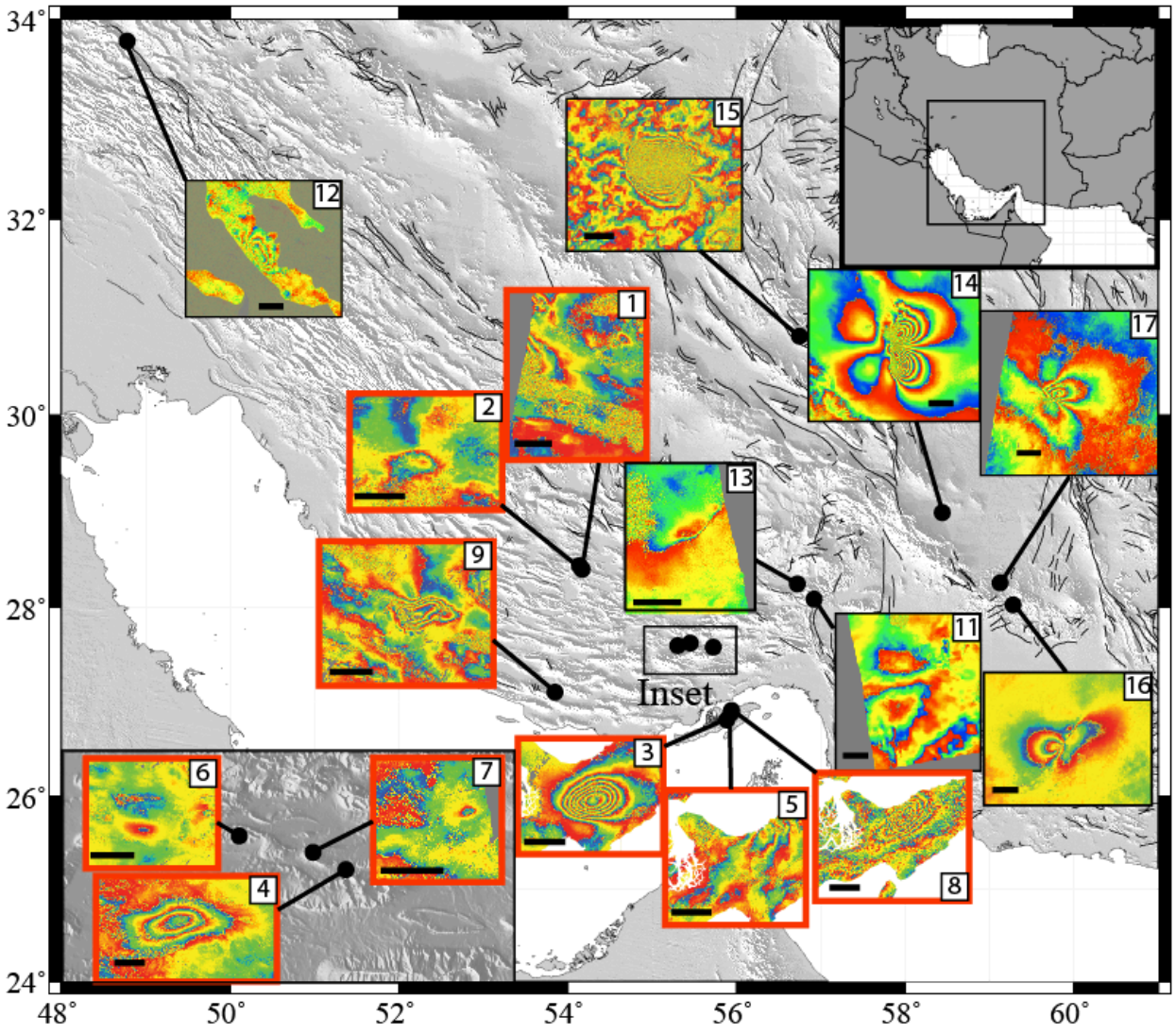

Figure 7.3: Wrapped interferograms of all observed events from 2003-2011. Numbers are event IDs (Figure 7.2, Tables 7.1-7.3). Interferograms shown are denoted in Appendix A2. Scale bars are 10km. Red-bound scenes occur in the SFB.

the question of whether triggered aseismic slip events can account for the large observed seismic strain rate deficit. If not, other mechanisms for reconciling the observed geodetic and seismic data, such as additional sources of aseismic deformation that act over longer time intervals within the interseismic period or large earthquakes that have not been sampled by the historical record, must be invoked.

Event	ID	Lon	Lat	Modeling	Reference
SFB					
2003.07.10	1	54.175	28.3967	sp	a
2003.11.28	2	54.138	28.435	sp	a
2005.11.27	3	55.910	26.880	dist	a,b,c,k
2006.03.25	4	55.725	27.58	dist	a,e,k
2006.06.28	5	55.942	26.913	dist	a,d
2007.03.23	6	55.303	27.597	dist	a
Unknown	7	55.454	27.624	sp	a
2008.09.10	8	55.939	26.885	dist	a,c,d
2010.07.20	9	53.848	27.104	dist	a
High Zagros					
2005.05.03	10	-	-	N/A	j
2006.02.28	11	56.923	28.086	sp	a,k
2006.03.31	12	49.90	33.62	dist	j
2007.08.25	13	56.723	28.247	sp	a
Other					
2003.12.26	14	58.35	29.08	dist	f,g,h
2005.02.22	15	56.75	30.809	dist	a,i
2010.12.20	16	59.125	28.257	dist	a
2011.01.27	17	59.281	28.025	dist	a

Table 7.1: Deformaiton events and event IDs (Figure 7.2, 7.3) observed with InSAR. Lon/Lat are center of fault patch with greatest slip (all determined from this study). Modeling indicates type of fault modeling: **sp** - single patch, **dist**- distributed slip.

References:
a)this study
b)Nissen et al. 2007
c)Lohman and Barnhart 2010
d)Nissen et al. 2010
e)Roustaei et al. 2010
f)Talebian et al. 2004
g)Fialko et al. 2005
h)Funning et al. 2005
i)Talebian et al. 2006
j)Peyret et al. 2008
k)Barnhart and Lohman accepted

7.3 Surface Deformation Sources

In order to further assess the locations of earthquakes and the relative contributions of earthquake and aseismic deformation in the Zagros and surrounding regions, we explore two end member models of strain accommodation across the Zagros and show that even if earthquake-triggered aseismic slip events are common, significant aseismic shortening must still occur through other mechanisms.

7.3.1 InSAR Data and Analysis

To construct our catalog of earthquake-related deformation observed with InSAR (Figure 7.2-3, Table 7.1), we use an orogen-wide InSAR time series based on data from the ENVISAT and ALSO satellites spanning 2003-2010 [*Barnhart and Lohman*, 2012]. For this paper, we define earthquake-related deformation as surface displacements observed with InSAR spanning coseismic intervals that are well fit by a fault slip model. We do not necessarily infer that the observed deformation is due to the earthquake but explore the alternative possibility that it may be triggered by a deeper earthquake, as we suggest occurred during the two earthquakes in *Barnhart and Lohman* [accepted]. The time series approach reduces the impact of noise present in individual SAR acquisitions and allows us to identify events that are near or below the detection threshold of single interferograms. When sufficient data coverage exists, InSAR time series analysis can allos detection of rates as low as ~1mm/yr over small spatial scales [e.g., *Finnegan et al.*, 2008; *Barnhart and Lohman*, 2012]. Following 2010, when extension of ENVISAT time

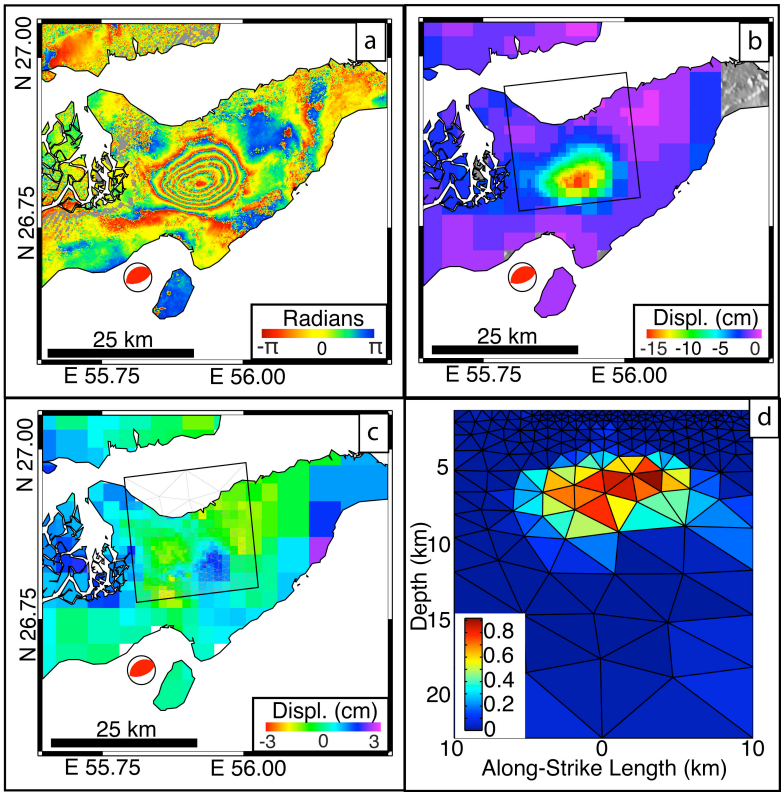

Figure 7.4: Example slip inversion for the 2005 Qeshm aseismic slip event (Event ID 3). A wrapped interogram is wrapped (a) then downsampled (b). The fixed fault plane is resampled and (c,d) and slip is inverted (c). c) shows a model residual. Slip distribution is viewed perpendicular to the fault plane. See Appendix A2 for InSAR acquisition details.

series was no longer possible due to change in the satellite orbit, we construct single ENVISAT and ALOS interferograms when available that span single teleseismically-recorded events. We also generate ERS interferograms for events >M_w5.5 between 1992 and 2002 that were not explored by Lohman & Simons [2005] but we do not find additional earthquake-related deformation. We ascribe earthquake-related events to single earthquakes by identifying the shortest time period in which the event occurred and correlate the event to earthquakes in the Global CMT catalog (GCMT) [*Ekström et al.*, 2012]. In all but one case, only one cataloged earthquake in the GCMT corresponds to each earthquake-related event (Figure 7.2-3, Table 7.1, ID7).

For each observed event, we generate interferograms at a resolution of 31x55 m using the JPL/Caltech Repeat Orbit Interferometry Package (ROI_PAC) [*Rosen et al.*, 2004] and remove the effect of topography with the Shuttle Radar Topography Mission (SRTM) DEM [*Farr et al.*, 2007] (Figure 7.3, 7.4a). When possible, we include multiple interferograms from different viewing geometries while avoiding repeated acquisitions dates, low signal coherence, and long post-seismic acquisition periods (Appendix A2). We downsample individual interferograms from ~10^6 to a computationally manageable ~10^2 pixels [*Lohman and Simons*, 2005b] (Figure 7.4b,c). For specific events (Appendix A2), we generate range and azimuth offsets through normalized cross correlation of the amplitude from full resolution SAR images using utilities available as part of ROI_PAC [*Rosen et al.*, 2004; *Barnhart et al.*, 2011].

To determine a best-fit fault geometry for each event, we first invert the downsampled interferograms for the geometry, location, orientation, and slip direction (rake) of a single rectangular fault with uniform slip [*Okada*, 1992] using the Neighborhood Algorithm

[*Sambridge*, 1999]. We consider both focal planes for blind thrust events where we cannot discriminate between either option. For several events, we invert for distributed slip by fixing the fault best-fit solution found by the Neighborhood Algorithm and extending the fault both along-strike and down-dip. We then discretize the fault plane with triangular dislocations [*Meade*, 2007] that vary in size according to the model resolution and invert for the best-fit slip distribution [*Barnhart and Lohman*, 2010] (Figure 7.4b). We impose non-negative slip constraints and fix the slip direction to the best-fit rake from the Neighborhood Algorithm inversion. We find that fixing rake does not produce noticeably different slip solutions than when we allow rake to vary. Slip distributions are smoothed with minimum moment constraints while the regularization coefficient is chosen using the $_j\boldsymbol{R}_i$ criterion (Appendix A.1) [*Barnhart and Lohman*, 2010].

7.3.2 InSAR Results

7.3.2.1 Zagros SFB Events

We identify nine events (M_w4.5-6.3) in the SFB from 2003-2010 (Figure 7.2-3, Table 7.1-2). All but one event can be linked to a single earthquake in the GCMT. The unknown event is the smallest (M_w4.5) and occurs in the vicinity of several earthquakes that exist in the ISC catalog [*International Seismological Centre*, 2010] between the dates spanned by the interferograms (2007.11.05 to 2008.05.06), so that we cannot definitively ascribe it to a single event. We find no other evidence of earthquake-like deformation in interferograms that do not span known earthquakes.

Inferred slip depths from distributed and single-patch slip inversions are consistently within the sedimentary section, shallower than 10-12km (Figure 7.5, Table 7.2). These depths,

ID	**Date**	**Mw**	**Depth**	**Depth**	**Strike**	**Dip**	**Rake**
		CMT/InSAR	*CMT/ISC*	*InSAR*	*CMT/InSAR*	*CMT/InSAR*	*CMT/InSAR*
	SFB Events						
1	2003.07.10^	5.7/5.9	15/19.7	6.3-10.3	277/274	33/36	93/97
2	2003.11.28	5.0/5.3	33/12.6	3.2-4.0	255/271	74/34	100/90
		5.0/5.3		2.5-5.1	43/94	19/48	60/105
3	2005.11.27	5.9/6.1	12/10*	3.5-9.5	257/264	39/47	83/68
		5.9/6.1		4.6-8.6	86/74	51/35	96/66
4	2006.03.25	5.9/6.0	14/10*	5-10.5	269/252	28/34	83/105
		5.9/6.0		4.7-12	97/72	63/50	93/95
5	2006.06.28	5.8/6.1	12/16	5.4-9.5	247/205	33/31	96/68
		5.8/6.1		3.6-12	59/45	57/64	86/112
6	2007.03.23	5.0/5.3	12/29.2	2.4-4.5	265/285	42/31	69/79
7	Unknown	-/4.5	-/-	0.7-2.5	-/241	-/55	-/110
		-/4.5		1.05-1.15	-/75	-/34	-/101
8	2008.09.10	6.1/6.3	12/12*	4.2-6.3	234/206	33/14	76/81
		6.1/6.2		2.5-11.6	71/35	58/56	99/99
9	2010.07.20	5.8/5.8	12/10	2.4-4.3	269/237	33/28	59/57
		5.8/5.8		1.4-6.9	124/69	62/42	109/73
	High Zagros						
11	2006.02.28	6.0	25.4/31.1	14.9-17.3	302/302	19/20	118/109
				12.2-18.2	93/93	73/71	81/53
12	2006.03.21	6.1/6.2	17/15.4	1.9-10.8	313/323	78/68	174/111
13	2007.08.25	5.0/5.0	23.5/10*	0.9-2.9	224/230	88/80	5/19
	Other						
14	2003.12.26	6.6/6.6	15/15	1.5-10	172/175	59/82	167/178
15	2005.02.22	6.4/6.4	12/13	0-8.5	266/79	47/64	100/101
16	2010.12.20	6.5/6.5	18.8/-	1.5-10	36/30	87/89	180/178
17	2011.01.27	6.2/6.3	14.3/-	2.3-11.8	129/123	77/90	5/2

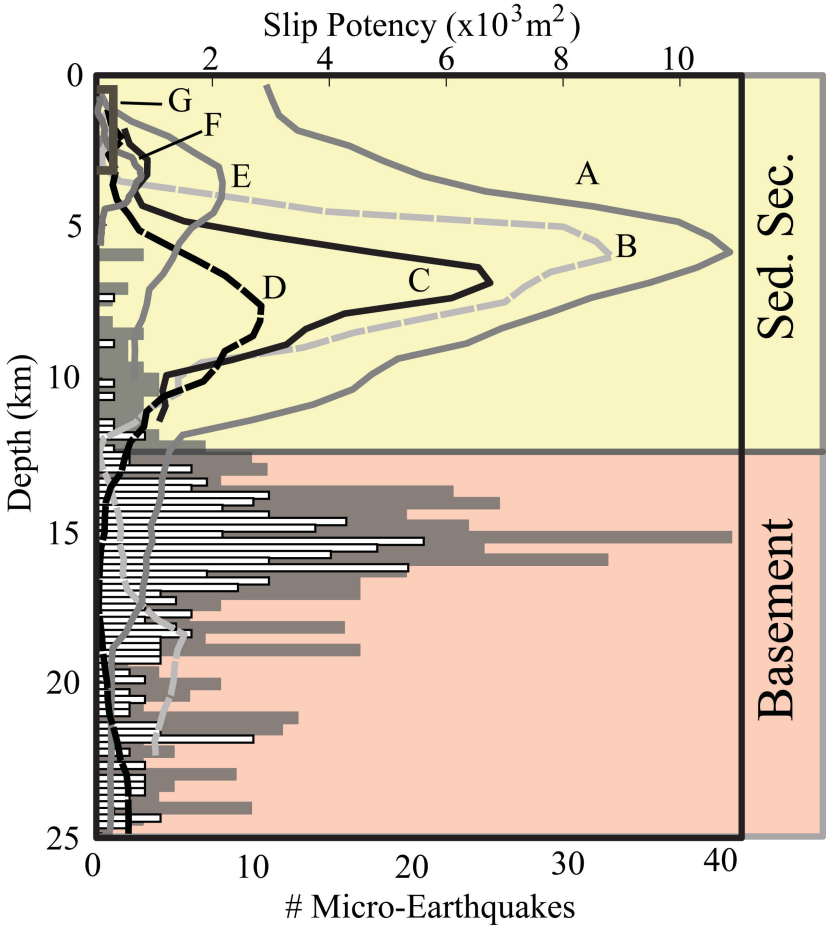

Figure 7.5: Slip profiles (lines) of SFB events (Figure 7.2, red focal mechanisms. A: 2008 Qeshm (ID8), B: 2006 Qeshm (ID5), C: 2005 Qeshm (ID3), D: 2006 Fin (ID4), E: 2010 Eshkanan (ID9), F: 2007 Fin (ID6), G: Unknown event (ID7). Dashed profiles indicate events discussed in Barnhart and Lohman [accepted]. Histograms indicate numbers of micro-earthquakes (Grey, Tatar et al. 2004) and 2005 Qeshm/2006 Fin aftershocks (White, Nissen et al. 2010, Roustaei et al. 2010) recorded from dense, local seismic networks. 10km is approximate depth of basement/ cover contact.

within error, are significantly shallower than both micro-earthquakes and aftershocks recorded throughout the SFB and are consistent with the depths of earthquake-triggered aseismic slip events postulated by *Barnhart and Lohman* [accepted]. Because no local observations of mainshock or aftershock depth are available for these other events, we cannot determine if the slip inferred from InSAR is aseismic or seismic. However, based on the similarities in depth, the presence of outcropping Hormuz Salt near these events, and the shallow depth of these events compared to locally-recorded micro-earthquakes [*Tatar et al.*, 2004] (Figure 7.5), we argue that

Table 7.2: Model parameters inverted from InSAR for all events and comparison to Global CMT and ISC catalog solutions. *-fixed value. Event IDs correspond to IDs in Figure 7.2-7.3 and Table 7.1. ^-event with poor data coverage, inversion is not well-resolved.

the relationship between basement earthquake rupture followed by aseismic slip in the sedimentary section could potentially hold for each of these events.

The magnitudes of slip that are inferred from the InSAR data are equal to or slightly larger than magnitudes determined from teleseismic observations (for μ=34GPa) for each event (Table 7.2). We observe no detectable post-seismic surface displacements in interferograms spanning timeperiods after the earthquakes [*Barnhart and Lohman*, 2012], although the InSAR constraints separating coseismic from postseismic intervals are not ideal. The shortest amount of post-seismic time included in coseismic interferograms available for the 2005 Qeshm and 2006 Fin events are 18 and 38 days [*Barnhart and Lohman*, accepted], while the shortest interval for any of the other SFB events is 6 days for the 2010.07.20 Eshkanan event. These observations imply that the total amount of convergence associated with earthquakes as much as doubles if one expands the time frame for each event to include a postseismic period of days to weeks where aseismic slip occurs in the sedimentary section.

7.3.2.2 Missing SFB Events

Five moderate earthquakes (M_w6.1 1994.03.01, M_w5.9 1994.06.20, M_w6.2 1999.05.06, M_w5.9 2010.09.27) exhibit no detectable surface displacement signal in the SFB (Figure 7.2, black focal mechanisms) [*Lohman and Simons*, 2005a, *this study*] [*Barnhart and Lohman*, 2012]. In each case, there are coherent InSAR observations spanning the coseismic period within 50km of the GCMT epicenter and no possible masking from nearby earthquakes. The absence of surface displacements despite high quality geodetic imagery strongly implies that each event occurred deep enough (e.g., in the basement) to not produce a detectable surface signal. These five earthquakes also did not apparently trigger detectable aseismic slip in the stratigraphic section. A

sixth event, located near the Zagros-Makran syntax (M_w6.6 1999.03.04) also does not produce a detectable surface signal, although errors in epicentral location may reasonably place this earthquake within or outside of the SFB. In addition to these six events, the absence of detectable deformation for three events (2003.07.10, 2006.03.25, and 2005.11.27), all of which are aftershocks following larger events, can be attributed to masking by the surface signal from the larger event (Figure 7.2, gray focal mechanisms). Likewise, an event on 2010.11.26 is located close to the Persian Gulf. This event could either have occurred in the basement and not triggered shallow aseismic slip, or it could have occurred offshore where it would be undetectable by InSAR.

7.3.2.3 2010-2011 Lut Block Strike Slip Earthquakes

We observe two strike slip events along the southern boundary of the Lut Block in addition to the 2003 Bam earthquake - the 2010.12.20 M_w6.5 and 2011.01.27 M_w6.2 events (Figure 7.3,6). Both events were shallow enough that the difference between candidate nodal plains could be distinguished using the InSAR observations, and we determine that the 2010.12.20 and 2011.01.27 event exhibited right- and left-lateral slip, respectively. These two events present an excellent example of conjugate fault planes accommodating horizontal, clockwise rotation of the Lut Block. They also help to define the southern boundary of the Lut Block, which is coincident with the volcanic arc of the Makran, where few strike slip faults are identified in geologic maps. The 2010.12.20 likely occurred on an unmapped extension of the Kahurak fault [*Kobayashi et al.*, 2012].

In the slip inversion for the 2010.12.20 event (Figure 7.6c), we incorporate high-quality ALOS interferograms and horizontal SAR azimuth offsets. Because both of these measurements

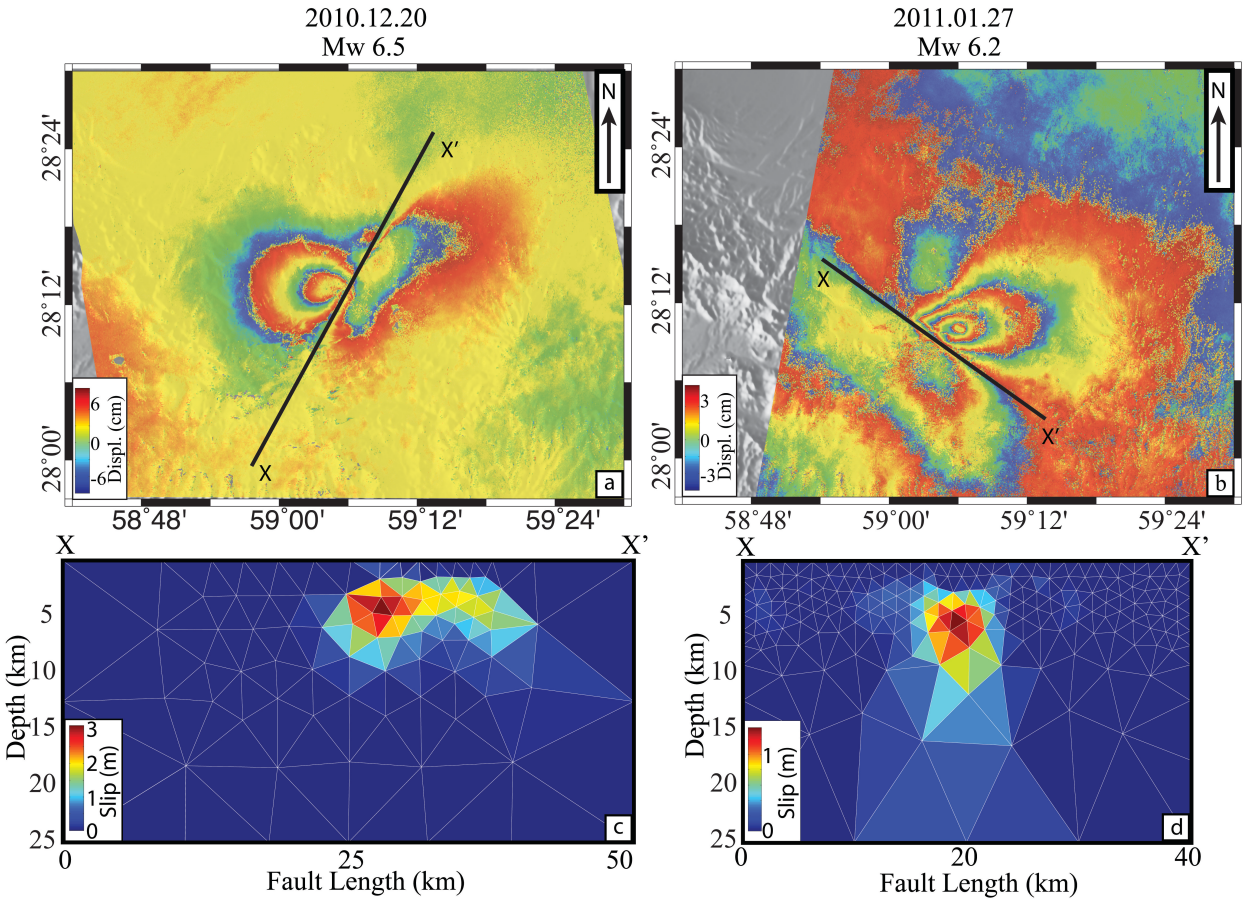

Figure 7.6: Wrapped interferograms (a,b) and slip distributions (c,d) of the 2010 (ID16) and 2011 (ID17) Lut Block strike-slip events. Map area for each interferogram is the same. Slip distributions are viewed perpendicular to the planes. See Appendix A2 for InSAR acquisition details.

yield measurements near the fault, we are able to resolve near surface fault slip. The earthquake likely does not rupture the surface, with a minimum slip depth of ~1.5km (Figure 7.6c). This observation of a shallow slip deficit is consistent with that found for the Bam earthquake and other strike slip faults globally [*Fialko et al.*, 2005]. We observe a similar shallow slip deficit in the 2011.01.27 event (Figure 7.6d); however, only a single viewing geometry is available and no horizontal offsets, so the presence of shallow slip is less constrained.

7.3.3 InSAR-Seismic Misfit

Here, we compare our catalog of earthquake locations inferred from InSAR to global catalogs (GCMT, NEIC, ISC) to explore if systematic epicentral mislocations exist. For many regions,

offsets between InSAR and teleseismic epicenter locations appear random [e.g., *Elliott et al.*, 2010; *Weston et al.*, 2011], and mislocations can be attributed to trade offs between epicenter, depth, and source function or random velocity structure errors [*Ferreira et al.*, 2011; *Devlin et al.*, 2012]. Regions where systematic mislocations exist help to identify major structures, such as subducting slabs, that must be accounted for with more accurate velocity models to correctly locate earthquakes [e.g., *Syracuse and Abers*, 2009]. In Iran, we define the epicentral location from InSAR to be the surface projection of the center of the fault patch with the greatest slip (analogous to the centroid from body-wave modeling, Figures 4d, 6c-d). In the SFB, where the observed deformation may likely result from triggered aseismic slip rather than from the main earthquake, we still use the slip distribution centroid as a proxy for the location of the underlying earthquake. This assumption is motivated by the observation that aftershocks of the 2005 Qeshm and 2006 Fin events occurred directly beneath the inferred aseismic slip and displacement signal [*Nissen et al.*, 2010; *Roustaei et al.*, 2010; *Barnhart and Lohman*, 2012]. The magnitude of misfits between the InSAR and teleseismic centroids are much greater than the spatial dimensions of the aftershock clouds, so our observation of a

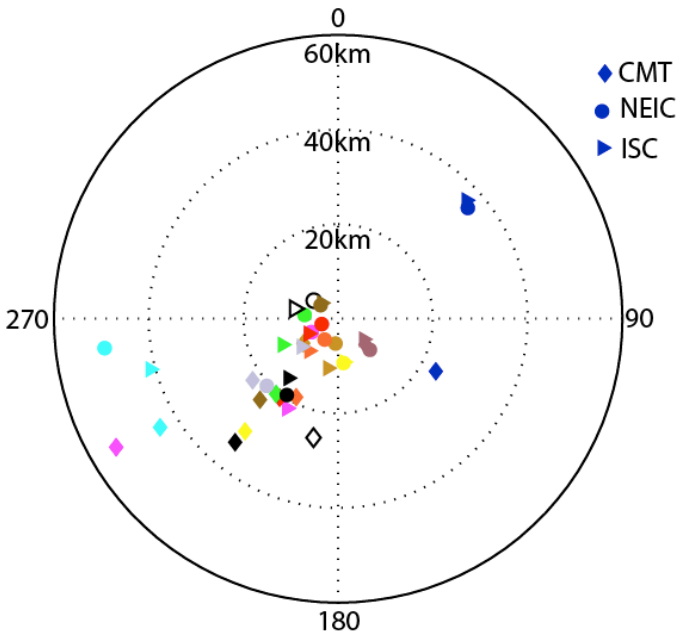

Figure 7.7: Polar plot showing misfit between teleseismic locations for all events in Table 7.2 and InSAR displacement location (center of plot). Colors indicate different events, shapes indicate seismic catalog. Contours are distance between InSAR (defined as center of InSAR signal) and catalog location; azimuth is direction of misfit.

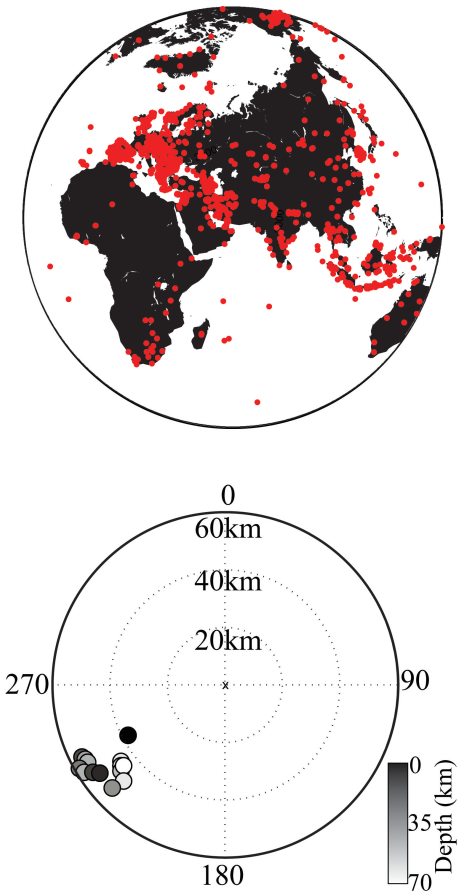

Figure 7.8: a) Maps of seismometers locations (red dots) relative to the 2010.12.20 (ID16) Lut earthquake (center of map). Little station coverage exists in Africa or eastern Asia. b) Polar plot of the 2010.12.20 event showing how location misfit changes with inferred depth (colored). Misfits move along SW-NE azimuth, but do not reach the InSAR location (center). Distance contours are in km. PREM velocity model used to generate shown misfits.

distinct azimuthal bias to the mislocations is probably robust to this assumption.

We find that teleseismic source locations are consistently mislocated to the southwest in the direction of Arabia and Africa (Figure 7.7). The only notable exception is the 2011.01.27 Lut event which is mislocated along the same azimuth but to the northeast. To explain the azimuthal misfit, we explore the sensitivity of earthquake locations to the coverage of global seismometers (Figure 7.8a), focusing on the largest event outside of the SFB – the M_w6.5 2010.12.20 Lut event (Figure 7.3, ID 16). We use seismometer locations and body wave picks reported by the ISC [*International Seismological Centre*, 2010] (Figure 7.8a,b) and relocate the events using the program *HYPOSAT* [*Schweitzer*, 2001]. We hypothesize that if earthquake locations are mislocated along a particular azimuth because of poor seismometer coverage, then adjusting reasonable tradeoffs between location, depth, and origin time will yield seismic locations collocated with the InSAR locations.

We fix event origin time to the ISC-reported value [*International Seismological Centre*, 2010], vary depth between 0 and 70km and invert for location. We also test different global one-dimensional velocity models (PREM, AK135, Jeffreys-Bullen Model, IASP91) [*Jeffreys et al.*,

1958; *Dziewonski and Anderson*, 1981; *Kennett and Engdahl*, 1991; *Kennett et al.*, 1995]. We find that as we vary depth, the preferred epicentral location varies, but never moves to within 35 km of the InSAR location (Figure 7.8c),. Locations migrate approximately along the NE-SW azimuth, which indicates that the distribution of seismometers may contribute, in part, to the observed bias (Figure 7.8). We infer that the remaining misfit is likely due to the neglect of three-dimensional variations in seismic velocity in our modeling, as postulated by *Ferreira et al.* [2011]. Specifically, the higher average body-wave velocity of African and Arabian lithosphere likely biases earthquake locations to the southwest.

7.4 Geodetic and Seismic Strain Rates

Strain rate tensors derived from ground-based geodetic observations (GPS) and earthquake focal mechanisms [*Kostrov*, 1974; *Molnar*, 1983] provide estimates of the relative contributions of seismic and aseismic strain accommodation. Across the Zagros, the small contribution of earthquake strain (15-22%) of the total shortening [*Jackson and McKenzie*, 1988; *Masson et al.*, 2005] suggests that significant shortening occurs aseismically of that seismic catalogs are too short to accurately characterize the distribution and magnitude of seismicity. In light of the inference that some earthquakes in the Zagros SFB generate significant aseismic slip in the sedimentary section [*Barnhart and Lohman*, accepted], we explore to end member models of strain accommodation. First, we consider strain rates imposed by earthquakes >M_w5.5 for the period 1911-2010 [*Jackson et al.*, 1995; *Ekström et al.*, 2012] (Figure 7.9, black dots), updating previous estimates to include the 2005-2008 Fin and Qeshm earthquake sequences and other recent events. Then, we consider a scenario in which every earthquake in the SFB triggers short-term aseismic slip equivalent in magnitude to the earthquake itself. This second scenario allows

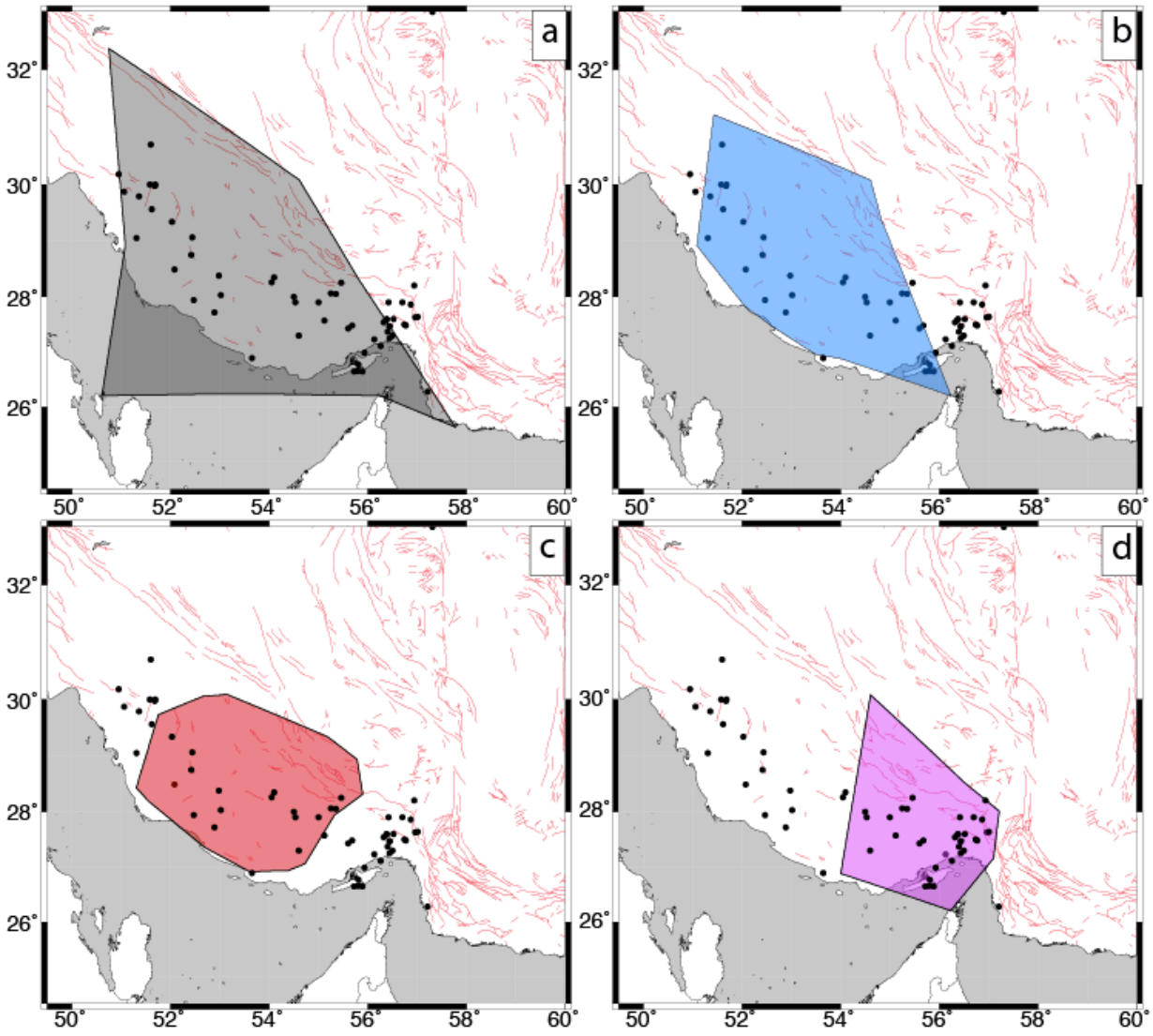

Figure 7.9: Outlines of campaign GPS networks used to determine mean horizontal strain rates. Dots are locations of earthquakes used to determine seismic strain rates. a: *Vernant et al.* 2004, b: *Nilforoushan et al*. 2003, c: *Hessami et al*. 2006, d: *Bayer et al*. 2006.

us to assess the contribution of coupled seismic-aseismic events to overall shortening across the Zagros.

7.4.1 Calculating Strain Rates

To calculated geodetic strain rates (ε_{ij}), we use campaign GPS measurements from four individual studies that span regions ranging from the southern SFB and the western-most Makran (Figure 7.9) [*Nilforoushan et al.*, 2003; *Bayer et al.*, 2006; *Hessami et al.*, 2006; *Walpersdorf et*

al., 2006]. To estimate the average strain within each region, we first use the GPS locations (X_i) and velocities (v_i) to invert for the four components of the velocity gradient tensor (L_{ij}) and two components of rigid body translation (d_i) [*Allmendinger et al.*, 2007; *Cardozo and Allmendinger*, 2009]:

$$v_i = d_i + L_{ij}X_j \qquad \text{(eq. 7.1)}$$

L_{ij} is an asymmetric tensor that we then decompose into the symmetric strain rate (e_{ij}) and antisymmetric rotation rate (Ω_{ij}) tensors:

$$L_{ij} = \varepsilon_{ij} + \Omega_{ij} = \left(\frac{L_{ij} + L_{ji}}{2}\right) + \left(\frac{L_{ij} - L_{ji}}{2}\right) \qquad \text{(eq. 7.2)}$$

An eigenvalue decomposition of ε_{ij} generates the principal strain orientations and magnitudes.

To determine the seismic strain rate, we use two catalogs (1900-1972 [*Jackson et al.*, 1995] and 1972-2011 [*Ekström et al.*, 2012]) that include moderate earthquake (>M 5.5) focal mechanisms located within the spatial bounds of the GPS networks (Figure 7.9). Events with reported M_S and m_b are converted to M_w using the relationships of [*Ekstrom and Dziewonski* [1988]. Because we do not know the appropriate focal planes for each earthquake, we use the methodology of *Kostrov* [1974]:

$$e_{ij} = \frac{1}{t}\frac{1}{V}\sum_{\#\ faults} M_0(u_i n_j) \qquad \text{(eq. 7.3)}$$

where t is the observation interval, V is the volume of the seismically deformed body (seismogenic thickness times surface area, defined by the area of the bounding networks), M_0 is the scalar moment, u is the unit vector parallel to slip, and n is the unit vector orthogonal to the

fault plane [*Marrett and Allmendinger*, 1990]. Again, an eigenvalue decomposition of e_{ij} produces the principal strain orientations and magnitudes. We use the principal shortening axis, which for the Zagros is near horizontal (<1° from horizontal) and comparable to the horizontal shortening axis inferred from GPS in equation 2.

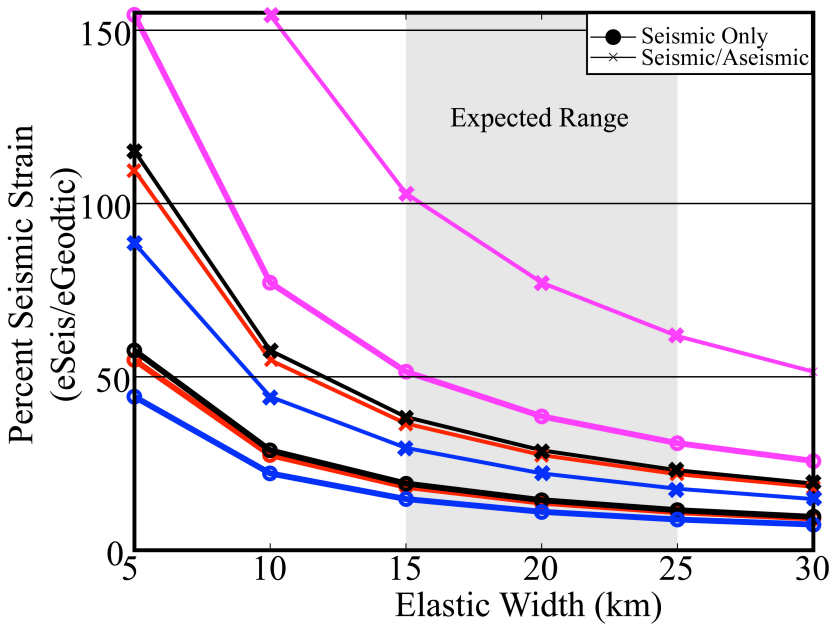

Figure 7.10: Percent of total convergence accommodated by seismic (dotted lines) and coupled seismic/aseismic (cross-hatched lines) for a range of inferred seismogenic thicknesses. Gray area indicates expected range of seismic thicknesses in the Zagros from micro-earthquake depths (Figure 7.5). Line colors correspond to network colors in Figure 7.9. The pink profile (Figure 7.9d) is consistently higher because of inclusion of the western Makran. Aseismic slip magnitudes assume a shear modulus of 34GPa, so these values are upper bounds of coupled seismic/aseismic strain.

ε_{ij} and e_{ij} are sensitive to several factors that we must account for in order to confidently compare the two values. First, e_{ij} is sensitive to both the surface area of the GPS network and to the homogeneity of strain with the network. If a network includes a large area outside of the deforming region, the inferred strain rate will be lower. To address this, we examine four independent GPS networks than span different proportions of the Zagros mountains and surrounding areas (Figure 7.9) [*Nilforoushan et al.*, 2003; *Bayer et al.*, 2006; *Hessami et al.*, 2006; *Walpersdorf et al.*, 2006]. Each network also has a different station density, with differing sensitivity to strain on individual structures within the Zagros. As shown in figure 7.10, the inferred strain rates within the networks agree despite inclusion of different spatial areas. The

only notable exception is the easternmost network (Figure 7.9d) [*Bayer et al.*, 2006] which includes portions of the Makran subduction zone. Secondly, ε_{ij} is highly sensitive to the deforming volume (V) and the assumed shear modulus (μ) used for calculating M_0. For V, there is a similar sensitivity to the area of the region used, and we account for the effect of assumed seismogenic thickness by varying depths used in our calculations from 5-30km. A 10km seismic thickness would span depth ranges of either the uppermost basement or sedimentary section, while a thickness of 20-25km would include deformation in both the basement and sedimentary section. We fix μ to 34GPa, which is a common value for continental crust and is an upper bound for sandstone and limestone [*Lee*, 2005]; thus, our seismic strain rate values should be considered a conservative estimate.

7.4.2 Strain Rate Results: A Persistent Discrepancy

Our comparison of geodetic (e_{ij}) and seismic catalog-based seismic (ε_{ij}) strains rates reveals low contributions of seismic strain of 10-20% for thicknesses of 10-15km (Figure 7.10). This is in agreement with previous work [*Jackson and McKenzie*, 1988; *Masson et al.*, 2005]. When we consider the scenario where all earthquakes in the SFB produce an equivalent magnitude of aseismic moment, the total strain accommodated during the days-weeks spanning earthquakes doubles, remaining well below the average geodetically-constrained rate. This discrepancy implies that an additional source of shortening is active in the Zagros (Figure 7.10).

One possible way to reconcile the missing strain budget would be if the historical seismic catalog has not adequately sampled larger magnitude earthquakes (Figure 7.11). The short time period spanned by historical seismic catalogs results in fairly low magnitude of completeness, so it is possible that the number of $>M_w7$ earthquakes has been lower during this past century than

the average. Using the standard Gutenburg-Richter relationship, we fit the annual moment release rates vs. magnitude for seismic catalogs [*Engdahl et al.*, 2006; *International Seismological Centre*, 2010; *Ekström et al.*, 2012] to predict the expected recurrence intervals of $>M_w7$ events. This results in abnormally high concentrations of smaller earthquakes relative to larger ones (B-values of 1.5-1.7), indicating that either earthquakes in the Zagros exhibit swarm-like behavior or that existing seismic catalogs do not capture the long-term magnitude frequency relationship of earthquakes in this region (Figure 7.11a). We determine the annual seismic moment deficit using the discrepancy between ε_{ij} and e_{ij} using the mean focal earthquake focal mechanism generated from equation 3 and a range of seismic thicknesses (Figure 7.11b). For a seismogenic thickness of 20km, we find the budget deficit is $\sim M_w7.0$ per year for the earthquake-only scenario. For the coupled seismic/aseismic slip scenario the deficit is $\sim M_w6.7$ per year, which is equivalent to the largest known SFB event [*Dewey and Grantz*, 1973]. While it may be possible that the catalogs have not adequately sampled the true occurrence of Mw 7 events, it is not likely that they occur, on average, at such elevated rates.

7.5 Discussion

The work presented here addresses several characteristics of active deformation in southern Iran. There are two end member hypotheses of the vertical partitioning of seismic and aseismic strain in the Zagros SFB: 1) Earthquakes shorten rigid, crystalline basement beneath the dominantly aseismic cover strata [e.g., *Berberian*, 1976, 1995; *Ni and Barazangi*, 1986; *Tatar et al.*, 2004; *Engdahl et al.*, 2006], and 2) the cover strata shortens through earthquake slip while the crystalline basement deforms aseismically [*Nissen et al.*, 2011]. Our work favors the seismically active Arabian basement model with the added caveat that aseismic shortening in the cover strata

occurs, in part, as earthquake-triggered aseismic fault slip during short time periods (days-weeks) following each earthquake. The similarity between the depth of slip during the 2005 Qeshm and 2006 aseismic events to the depths inferred in this study suggest that coupled seismic-aseismic slip events in the SFB may be common (Figure 7.5). These events are not ubiquitous, though, as several strike slip and reverse-type earthquakes >M_w6 exhibit no detectable surface displacements and likely occurred in the basement without triggering any aseismic deformation at shallower depths (Figure 7.2, black focal mechanisms).

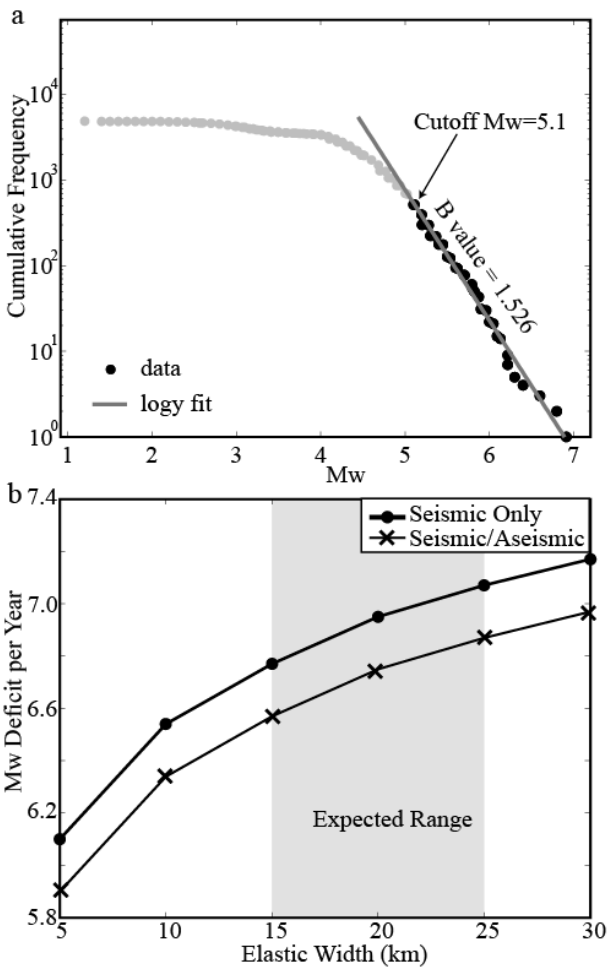

Figure 7.11: a: Gutenburg-Richter magnitude frequency plot for Zagros SFB events from the ISC catalog. B-value of 1.526 is slope of log fit (gray line) for events of M_w 5.1 or greater (black dots). Gray dots indicate earthquake magnitudes below the cutoff magnitude. b: Missing annual moment magnitude in the Zagros as a function of inferred elastic width. Profiles generated based on geodetic and seismic strain rates within the Zagros-bounding GPS network[*Vernant et al.* 2004] (Figure 7.9a). Gray region indicates expected range of seismogenic thicknesses from micro-earthquake depths (Figure 7.5).

We have further shown that neither observed seismicity nor coupled seismic/ aseismic events can account for the full convergence rate between Arabia and Eurasia. One earthquake of ~M_w7.0 (seismic only) and ~M_w6.7 (coupled seismic/aseismic) per year (Figure 7.11b) can explain the strain deficit; however, because a yearly recurrence interval of M_w6.7 events is not observed and there is no record of events as large as M_w7.0 in the Zagros [*Ambraseys and Melville*, 2005], it is unlikely

that the observed seismic strain deficit is due to random sampling of the expected probability distribution for earthquakes over the past century. We acknowledge, though, that it is difficult to estimate the maximum expected magnitude earthquake even in regions with longer seismic catalogs [*Kijko*, 2004]. Excluding the possibility of a large (>M_w7) earthquake, the remaining strain rate deficit is probably accommodated by a combination of long-term aseismic deformation and short-term transient aseismic deformation events that have not yet been observed with geodesy. Active detachment folding [e.g., *Burberry et al.*, 2008] and the lack of detectable interseismic deformation across single structures in the SFB [*Barnhart and Lohman*, 2012] provide evidence for long-term (decades to millennia) shortening within the SFB.

7.6 Conclusions

The accommodation of shortening in southern Iran results from complicated partitioning of strain vertically, along-strike, and across the width of the Zagros, Makran, and Central Iran. InSAR and micro-seismicity recorded from dense local networks suggest that the rigid, crystalline Arabian crust deforms seismically while driving aseismic fault slip and fold growth in the overriding Zagros Simply Folded Belt in the period of time immediately following earthquakes. Despite high seismicity rates and the possibility that each earthquake may be accompanied by an equal amount of moment release within the sedimentary section in the weeks following its occurrence, >50% of shortening across the Zagros must be accommodated by deformation processes not related to observed earthquakes. Candidate processes include the possibility that the region has experienced a deficit of earthquakes over the past century of a M7.0 earthquake per year, significant transient aseismic deformation episodes unrelated to earthquakes that have happened to not be observed with InSAR, and long-term, perhaps continuous, aseismic deformation that is

below the detection threshold of InSAR. Forthcoming InSAR missions will help to provide increased temporal resolution of deformation processes to further resolve discrepancies in earthquake catalogs and address the nature of earthquake cycle deformation across the Zagros and adjoining regions.

7.7 References

Allmendinger, R. W., R. Reilinger, and J. Loveless (2007), Strain and rotation rate from GPS in Tibet, Anatolia, and the Altiplano, *Tectonics*, *26*(3), TC3013, doi: 10.1029/2006TC002030.

Ambraseys, N. N., and C. P. Melville (2005), *A History of Persian Earthquakes*, Cambridge University Press.

Barnhart, W. D., and R. B. Lohman (accepted), Phantom earthquakes and triggered aseismic creep: Vertical partitioning of strain during earthquake sequence in Iran, *Geophys. Res. Lett.*

Barnhart, W. D., and R. B. Lohman (2010), Automated fault model discretization for inversions for coseismic slip distributions, *J. Geophys. Res.*, *115*(B10), B10419, doi: 10.1029/2010JB007545.

Barnhart, W. D., and R. B. Lohman (2012), Regional trends in active diapirism revealed by mountain range-scale InSAR time series, *Geophys. Res. Lett.*, *39*(8), L08309, doi: 10.1029/2012GL051255.

Barnhart, W. D., M. J. Willis, R. B. Lohman, and A. K. Melkonian (2011), InSAR and Optical Constraints on Fault Slip during the 2010–2011 New Zealand Earthquake Sequence, *Seismological Research Letters*, *82*(6), 815–823, doi:10.1785/gssrl.82.6.815.

Bayer, R., J. Chery, M. Tatar, P. Vernant, M. Abbassi, F. Masson, F. Nilforoushan, E. Doerflinger, V. Regard, and O. Bellier (2006), Active deformation in Zagros–Makran transition zone inferred from GPS measurements, *Geophysical Journal International*, *165*(1), 373–381, doi:10.1111/j.1365-246X.2006.02879.x.

Berberian, M. (1976), *Contribution to the seismotectonics of Iran (part II-III): in commemoration of the 50th anniversary of the Pahlavi dynasty*, Ministry of Industry and Mines, Geological Survey of Iran, Tectonic and Seismotectonic Section.

Berberian, M. (1995), Master “blind” thrust faults hidden under the Zagros folds: active basement tectonics and surface morphotectonics, *Tectonophysics*, *241*(3–4), 193–224, doi:10.1016/0040-1951(94)00185-C.

Burberry, C. M., J. W. Cosgrove, and J. G. Liu (2008), Spatial arrangement of fold types in the Zagros Simply Folded Belt, Iran, indicated by landform morphology and drainage pattern characteristics, *Journal of Maps*, *4*(1), 417–430, doi:10.4113/jom.2008.97.

Bürgmann, R., P. A. Rosen, and E. J. Fielding (2000), Synthetic Aperture Radar Interferometry to Measure Earth's Surface Topography and Its Deformation, *Annual Review of Earth and Planetary Sciences*, *28*(1), 169–209, doi:10.1146/annurev.earth.28.1.169.

Cardozo, N., and R. W. Allmendinger (2009), SSPX: A program to compute strain from displacement/velocity data, *Computers & Geosciences*, *35*(6), 1343–1357, doi:10.1016/j.cageo.2008.05.008.

Colman-Sadd, S. P. (1978), Fold development in Zagros simply folded belt, Southwest Iran, *AAPG Bulletin*, *62*(6), 984–1003.

Devlin, S., B. L. Isacks, M. E. Pritchard, W. D. Barnhart, and R. B. Lohman (2012), Depths and focal mechanisms of crustal earthquakes in the central Andes determined from teleseismic waveform analysis and InSAR, *Tectonics*, *31*(2), TC2002, doi:10.1029/2011TC002914.

Dewey, J. W., and A. Grantz (1973), The Ghir earthquake of April 10, 1972 in the Zagros Mountains of southern Iran: seismotectonic aspects and some results of a field reconnaissance, *Bulletin of the Seismological Society of America*, *63*(6-1), 2071–2090.

Dziewonski, A. M., and D. L. Anderson (1981), Preliminary reference Earth model, *Physics of the Earth and Planetary Interiors*, *25*(4), 297–356, doi:10.1016/0031-9201(81)90046-7.

Ekstrom, G., and A. Dziewonski (1988), Evidence of Bias in Estimations of Earthquake Size, *Nature*, *332*(6162), 319–323, doi:10.1038/332319a0.

Ekström, G., M. Nettles, and A. M. Dziewoński (2012), The global CMT project 2004–2010: Centroid-moment tensors for 13,017 earthquakes, *Physics of the Earth and Planetary Interiors*, *200–201*(0), 1–9, doi:10.1016/j.pepi.2012.04.002.

Elliott, J. R., R. J. Walters, P. C. England, J. A. Jackson, Z. Li, and B. Parsons (2010), Extension on the Tibetan plateau: recent normal faulting measured by InSAR and body wave seismology, *Geophysical Journal International*, *183*(2), 503–535, doi:10.1111/j.1365-246X.2010.04754.x.

Engdahl, E. R., J. A. Jackson, S. C. Myers, E. A. Bergman, and K. Priestley (2006), Relocation and assessment of seismicity in the Iran region, *Geophys. J. Int.*, *167*(2), 761–778, doi:10.1111/j.1365-246X.2006.03127.x.

Falcon, N. (1974), Zagros Mountain, Mesozoic-Cenozoic Orogenic Belts, *Geological Society, London*, *Spec. Pub. 4*, 199–211.

Farr, T. G. et al. (2007), The shuttle radar topography mission, *Rev. Geophys.*, *45*(2), doi: 10.1029/2005RG000183.

Ferreira, A. M. G., J. Weston, and G. J. Funning (2011), Global compilation of interferometric synthetic aperture radar earthquake source models: 2. Effects of 3-D Earth structure, *J. Geophys. Res.*, *116*(B8), B08409, doi:10.1029/2010JB008132.

Fialko, Y., D. Sandwell, M. Simons, and P. Rosen (2005), Three-dimensional deformation caused by the Bam, Iran, earthquake and the origin of shallow slip deficit, *Nature*, *435*(7040), 295–299, doi:10.1038/nature03425.

Finnegan, N. J., M. E. Pritchard, R. B. Lohman, and P. R. Lundgren (2008), Constraints on surface deformation in the Seattle, WA, urban corridor from satellite radar interferometry time-series analysis, *Geophysical Journal International*, *174*(1), 29–41, doi:10.1111/j. 1365-246X.2008.03822.x.

Hatzfeld, D., and P. Molnar (2010), Comparisons of the kinematics and deep structures of the Zagros and Himalaya and of the Iranian and Tibetan plateaus and geodynamic implications, *Rev. Geophys.*, *48*(2), RG2005, doi:10.1029/2009RG000304.

Hessami, K., F. Nilforoushan, and C. J. Talbot (2006), Active deformation within the Zagros Mountains deduced from GPS measurements, *Journal of the Geological Society*, *163*(1), 143–148, doi:10.1144/0016-764905-031.

International Seismological Centre (2010), *On-line Bulletin*, Int. Seis. Cent., Thatcham, United Kingdom. [online] Available from: http://www.isc.ac.uk

Jackson, J., and D. McKenzie (1988), The relationship between plate motions and seismic moment tensors, and the rates of active deformation in the Mediterranean and Middle East, *Geophysical Journal*, *93*(1), 45–73, doi:10.1111/j.1365-246X.1988.tb01387.x.

Jackson, J., J. Haines, and W. Holt (1995), The accommodation of Arabia-Eurasia Plate convergence in Iran, *J. Geophys. Res.*, *100*(B8), 15205–15,219, doi:10.1029/95JB01294.

Jeffreys, S. H., K. E. Bullen, and B. A. for the A. of Science (1958), *Seismological tables*, Office of the British Association.

Kennett, B. L. N., and E. R. Engdahl (1991), Traveltimes for global earthquake location and phase identification, *Geophysical Journal International*, *105*(2), 429–465, doi:10.1111/j. 1365-246X.1991.tb06724.x.

Kennett, B. L. N., E. R. Engdahl, and R. Buland (1995), Constraints on seismic velocities in the Earth from traveltimes, *Geophysical Journal International*, *122*(1), 108–124, doi: 10.1111/j.1365-246X.1995.tb03540.x.

Kijko, A. (2004), Estimation of the Maximum Earthquake Magnitude, m max, *Pure appl. geophys.*, *161*(8), 1655–1681, doi:10.1007/s00024-004-2531-4.

Kobayashi, T., M. Tobita, A. Suzuki, and Y. Noguchi (2012), InSAR-derived Coseismic Deformation of the 2010 Southeastern Iran Earthquake (M6.5) and its Relationship with the Tectonic Background in the South of Lut Block, *Bull. Geospat. Info. Auth. Japan*, *60*, 7–17.

Kostrov, V. (1974), Seismic moment and energy of earthquakes, and seismic flow of rock, *Physics of the Solid Earth*, *1*, 13–21.

Langbein, J., J. R. Murray, and H. A. Snyder (2006), Coseismic and Initial Postseismic Deformation from the 2004 Parkfield, California, Earthquake, Observed by Global Positioning System, Electronic Distance Meter, Creepmeters, and Borehole Strainmeters, *Bulletin of the Seismological Society of America*, *96*(4B), S304–S320, doi: 10.1785/0120050823.

Lee, M. W. (2005), Proposed moduli of dry rock and their application to predicting elastic velocities of sandstones, *USGS Scientific Investigations Report 2005-5119*, 1–14.

Lohman, R. B., and J. J. McGuire (2007), Earthquake swarms driven by aseismic creep in the Salton Trough, California, *J. Geophys. Res.*, *112*(B4), B04405, doi: 10.1029/2006JB004596.

Lohman, R. B., and M. Simons (2005a), Locations of selected small earthquakes in the Zagros mountains, *Geochem. Geophys. Geosyst.*, *6*(3), Q03001, doi:10.1029/2004GC000849.

Lohman, R. B., and M. Simons (2005b), Some thoughts on the use of InSAR data to constrain models of surface deformation: Noise structure and data downsampling, *Geochem. Geophys. Geosyst.*, *6*(1), Q01007, doi:10.1029/2004GC000841.

Maggi, A., J. A. Jackson, K. Priestley, and C. Baker (2000), A re-assessment of focal depth distributions in southern Iran, the Tien Shan and northern India: do earthquakes really occur in the continental mantle?, *Geophys. J. Int.*, *143*(3), 629–661, doi:10.1046/j. 1365-246X.2000.00254.x.

Masson, F., J. Chéry, D. Hatzfeld, J. Martinod, P. Vernant, F. Tavakoli, and M. Ghafory-Ashtiani (2005), Seismic versus aseismic deformation in Iran inferred from earthquakes and geodetic data, *Geophysical Journal International*, *160*(1), 217–226, doi:10.1111/j. 1365-246X.2004.02465.x.

Meade, B. J. (2007), Algorithms for the calculation of exact displacements, strains, and stresses for triangular dislocation elements in a uniform elastic half space, *Computers & Geosciences*, *33*(8), 1064–1075, doi:10.1016/j.cageo.2006.12.003.

Molnar, P. (1983), Average Regional Strain Due to Slip on Numerous Faults of Different Orientations, *Journal of Geophysical Research*, *88*(NB8), 6430–6432, doi:10.1029/JB088iB08p06430.

Ni, J., and M. Barazangi (1986), Seismotectonics of the Zagros continental collision zone and a comparison with the Himalayas, *J. Geophys. Res.*, *91*(B8), 8205–8218, doi:10.1029/JB091iB08p08205.

Nilforoushan, F. et al. (2003), GPS network monitors the Arabia-Eurasia collision deformation in Iran, *Journal of Geodesy*, *77*(7-8), 411–422, doi:10.1007/s00190-003-0326-5.

Nissen, E., F. Yamini-Fard, M. Tatar, A. Gholamzadeh, E. Bergman, J. R. Elliott, J. A. Jackson, and B. Parsons (2010), The vertical separation of mainshock rupture and microseismicity at Qeshm island in the Zagros fold-and-thrust belt, Iran, *Earth and Planetary Science Letters*, *296*(3–4), 181–194, doi:10.1016/j.epsl.2010.04.049.

Nissen, E., M. Tatar, J. A. Jackson, and M. B. Allen (2011), New views on earthquake faulting in the Zagros fold-and-thrust belt of Iran, *Geophysical Journal International*, *186*(3), 928–944, doi:10.1111/j.1365-246X.2011.05119.x.

Okada, Y. (1992), Internal Deformation Due to Shear and Tensile Faults in a Half-Space, *Bull. Seismol. Soc. Amer.*, *82*(2), 1018–1040.

Pritchard, M. E., M. Simons, P. A. Rosen, S. Hensley, and F. H. Webb (2002), Co-seismic slip from the 1995 July 30 Mw= 8.1 Antofagasta, Chile, earthquake as constrained by InSAR and GPS observations, *Geophysical Journal International*, *150*(2), 362–376, doi:10.1046/j.1365-246X.2002.01661.x.

Rosen, P. A., S. Hensley, G. Peltzer, and M. Simons (2004), Updated repeat orbit interferometry package released, *Eos Trans. AGU*, *85*(5), 47, doi:10.1029/2004EO050004.

Roustaei, M., E. Nissen, M. Abbassi, A. Gholamzadeh, M. Ghorashi, M. Tatar, F. Yamini-Fard, E. Bergman, J. Jackson, and B. Parsons (2010), The 2006 March 25 Fin earthquakes (Iran)—insights into the vertical extents of faulting in the Zagros Simply Folded Belt, *Geophysical Journal International*, *181*(3), 1275–1291, doi:10.1111/j.1365-246X.2010.04601.x.

Sambridge, M. (1999), Geophysical inversion with a neighbourhood algorithm—I. Searching a parameter space, *Geophysical Journal International*, *138*(2), 479–494, doi:10.1046/j.1365-246X.1999.00876.x.

Schweitzer, J. (2001), HYPOSAT – An Enhanced Routine to Locate Seismic Events, *Pure and Applied Geophysics*, *158*(1), 277–289, doi:10.1007/PL00001160.

Stocklin, J. (1974), Possible ancient continental margins in Iran, in *Geology of Continental Margins*, pp. 873–877, Springer, New York.

Syracuse, E. M., and G. A. Abers (2009), Systematic biases in subduction zone hypocenters, *Geophys. Res. Lett.*, *36*(10), L10303, doi:10.1029/2009GL037487.

Tatar, M., D. Hatzfeld, and M. Ghafory-Ashtiany (2004), Tectonics of the Central Zagros (Iran) deduced from microearthquake seismicity, *Geophysical Journal International*, *156*(2), 255–266, doi:10.1111/j.1365-246X.2003.02145.x.

Walpersdorf, A., D. Hatzfeld, H. Nankali, F. Tavakoli, F. Nilforoushan, M. Tatar, P. Vernant, J. Chéry, and F. Masson (2006), Difference in the GPS deformation pattern of North and Central Zagros (Iran), *Geophysical Journal International*, *167*(3), 1077–1088, doi: 10.1111/j.1365-246X.2006.03147.x.

Weston, J., A. M. G. Ferreira, and G. J. Funning (2011), Global compilation of interferometric synthetic aperture radar earthquake source models: 1. Comparisons with seismic catalogs, *J. Geophys. Res.*, *116*(B8), B08408, doi:10.1029/2010JB008131.

APPENDIX A1

REGULARIZATION: ¡ℜ¡[1]

A1.1 Regularization

We define a "good" choice of regularization strength, **λ**, as one that would fit the underlying, noise-free signal (**d_0**) as well as possible without introducing model characteristics that are merely fitting the noise. Increasing **λ** decreases our ability to fit the underlying signal, as the inferred model is forced to be increasingly smooth. As we decrease **λ**, the inferred model fits more and more of the noise with an increasingly complex model that does not necessarily produce a good fit to **d_0**. Our goal is to find the value of **λ** that balances these two sources of error, for the real-world scenario where we do not know the actual properties of **d_0**. Below, we break down the two sources of error in the case where we do have access to the real value of **d_0** and the exact statistical properties of the data noise, and then describe how we apply our method to real data.

To better understand the behavior of regularized slip inversions, we will consider the effects of the inversion on our fit to **d_0** and to the noise, respectively. This focus on the directly observable data values differs from approaches that depend on measures of model length or roughness, such as the "L curve" parameter choice methods. We rely on the fact that we can treat our observed data, **d_i**, as a sum of two parts:

$$d_i \equiv d_o + n_i \qquad \text{(eq. A1.1)}$$

[1] Published as an appendix in: Barnhart,W.D., R.B. Lohman (2010), Automated fault model discretization for inversions for co-seismic slip distributions, J. Geophys. Res., 115, B10419, doi:10.1029/2010JB007545. Reprinted with permission of AGU

where $\mathbf{d_0} = \mathbf{G m_0}$ is the physical response of the earth to an input slip distribution ($\mathbf{m_0}$) in the absence of noise, and $\mathbf{n_i}$ are realizations of independent, identically distributed Gaussian noise with variance 2σ and zero mean. If the forward and inverse problems are linear, we can separate the inversion into the parts controlled by the exact data, $\mathbf{d_0}$, and by the noise. Below, we will discuss the more general, nonlinear case which holds when positivity constraints are incorporated into the inversion.

The regularization error [e.g., Hansen, 1998] quantifies the degree to which the inferred slip models can fit the exact data in the absence of noise:

$$m_0^* = G^{-g^*} d_0$$
$$d_0^* = G m_0^* \qquad \text{(eq. A1.2, A1.3)}$$

where $\mathbf{G^{-g^*}}$ is the generalized inverse for a regularized inversion with a given λ [e.g., Menke, 1989], $\mathbf{m_0}^*$ is the smoothed version of m0 that we would infer with a particular regularization, and $\mathbf{d_0}^*$ is the smoothed surface deformation predicted by $\mathbf{m_0}^*$. In general we use the asterisk to signify inversion quantities where we have applied smoothing. We define the regularization error, $_0\mathbf{r_0}$, as the difference between the exact data ($\mathbf{d_0}$) and the deformation predicted by the smoothed model ($\mathbf{d_0}^*$):

$$_0 r_0 \equiv d_0 - d_0^* \qquad \text{(eq. A1.4)}$$

The perturbation error [e.g., Hansen, 1998] is the degree to which a given realization of the noise in the data, $\mathbf{n_i}$, is mapped by the inversion into the inferred slip, $\mathbf{m_i}^*$, and back into our predicted synthetic data, $\mathbf{d_i}^*$. We separate the operation of $\mathbf{G^{-g^*}}$ on the noisy data into a sum of its parts:

$$m_i^* = G^{-g^*} d_0 + G^{-g^*} n_i$$
$$d_i^* = d_0^* + n_i^* \qquad \text{(eq. A1.5, A1.6)}$$

where $\mathbf{n_i}^*$ is the noise filtered by our regularization. To help us separate out that part of the inversion that is only fitting the noise in the data, we define:

$$ {}_j r_i^n \equiv n_j - n_i^* \qquad \text{(eq. A1.7)} $$

$\mathbf{{}_j r_i^n}$ compares a smoothed set of noise ($\mathbf{n_i}^*$) with a completely independent realization of the noise ($\mathbf{n_j}$). This quantity, which we define as the perturbation error, increases as λ decreases, because an inversion that fits one set of noise very well will not necessarily fit an independent set of noise. The total error when we compute a residual between one data set and a smoothed, independent data set is:

$$ {}_j r_i \equiv d_j - d_i^* \qquad \text{(eq. A1.8)} $$

Combining equations (A1.4) and (A1.8)), we get:

$$ {}_j r_i = {}_0 r_0 + {}_j r_i^n \qquad \text{(eq. A1.9)} $$

indicating that the total error is equivalent to the sum of the perturbation and regularization errors. The total error is the quantity that we wish to minimize in our choice of λ. We define measures of the size of these residuals as:

$$ {}_j\Re_i \equiv \tfrac{1}{k} \sum {}_j r_i^2 $$
$$ {}_0\Re_0 \equiv \tfrac{1}{k} \sum {}_0 r_0^2 \qquad \text{(eq. A1.10, A1.11)} $$

where k is the number of observation points used in the inversion. The value of λ that minimizes $\mathbf{{}_j\Re_i}$ is the optimum regularization that we use in our inversions. As λ approaches 0, the perturbation error approaches 2σ and the regularization error approaches 0. We use a script $\mathfrak{R}$ to avoid confusion with **R**, the model resolution matrix. As λ becomes large and smoothing increases, the perturbation error decreases and the regularization error increases.

A1.2 Calculating $\mathbf{{}_j\Re_i}$ for Exact Data

One way to calculate the value of p or λ that optimizes ${}_j\mathfrak{R}_i$ for a synthetic system where the input model and data noise characteristics are known would be to create a large number of synthetic data sets with different realizations of the noise, and to calculate ${}_j\mathfrak{R}_i$ numerically by computing all the permutations of $\mathbf{d_j} - \mathbf{d_i}^*$. However, we can be more efficient in these synthetic cases and capitalize on the fact that we know the input model, $\mathbf{m_0}$, and the covariance structure, $\mathbf{C_d}$, of the noise. We can use these two quantities to find the value of ${}_j\mathfrak{R}_i$ analytically for any (p, λ).

We can also write equations (A1.2)–(A1.4) as:

$$m_0^* = Rm_0$$
$$d_0^* = Nd_0 \qquad \text{(eq. A1.12- A1.14)}$$
$${}_0r_0 = [I - N]\left[\frac{d_0}{d_0}\right]$$

where $\mathbf{R} = \mathbf{G}^{-\mathbf{g}^*}\mathbf{G}$ and $\mathbf{N} = \mathbf{G}^{-\mathbf{g}^*}$ are the model and data resolution matrices, respectively [e.g., Menke, 1989] and **I** is an identity matrix. If we define a matrix **M** as **[I −N]**, then we can express the residual quantities as:

$${}_0r_0 = M\left[\frac{d_0}{d_0}\right]$$
$${}_jr_i = M\left[\frac{d_j}{d_i}\right] \qquad \text{(eq. A1.15-A1.17)}$$
$${}_jr_i^n = M\left[\frac{n_j}{n_i}\right]$$

We can expand equation (A1.10) using equation (A1.9):

$${}_j\mathfrak{R}_i = \tfrac{1}{k}\sum\left[({}_0r_0)^2 + 2({}_0r_0)({}_jr_i^n) + ({}_jr_i^n)^2\right] \qquad \text{(eq. A1.18)}$$

Since ${}_j\mathbf{r}_i^{\mathbf{n}}$ is a random variable with mean 0, the middle term disappears and we are left with:

$$ {}_j\Re_i = \tfrac{1}{k}\sum({}_0r_0)^2 + \tfrac{1}{k}\sum({}_jr_i^n)^2 \qquad \text{(eq. A1.19)} $$

The first term is equivalent to the definition of $\mathbf{{}_0\Re_0}$. Since the mean of $\mathbf{{}_jr_i^n}$ is 0, the expectation of the second term in equation (A1.19) is a sum over the variances of $\mathbf{{}_jr_i^n}$ at each data point. If $\mathbf{C_d}$ is the data covariance matrix, then by the law of covariance propagation:

$$ C_r = MC_dM^T \qquad \text{(eq. A1.20)} $$

where $\mathbf{C_r}$ is the covariance matrix of $\mathbf{{}_jr_i^n}$. Therefore, we have:

$$ {}_j\Re_i = {}_0\Re_0 + \tfrac{1}{k}\sum diag(C_r) \qquad \text{(eq. A1.21)} $$

This formulation of $\mathbf{{}_j\Re_i}$ depends only on the input model, $\mathbf{m_0}$, and on the noise covariance, which are both quantities that we would know for a synthetic system.

A.1.3 Approximating $\mathbf{{}_j\Re_i}$ for Real Data: $\mathbf{{}_j\Re_i^a}$

In order to form an approximation of $\mathbf{{}_j\Re_i}$ in the case where we only have one data set and impose nonlinear constraints such as bounds on the inferred model, we attempt to infer the quantities described in section A2 from our inversion of the single data set and our knowledge of characteristics of the noise in the data.

Given the data covariance matrix $\mathbf{C_d}$, we can compute the second term in equation (A9) and are left with a need to approximate $\mathbf{{}_0\Re_0}$. We can compute one realization of $\mathbf{{}_ir_i = d_i - d_i^*}$ and $\mathbf{{}_i\Re_i \equiv (1/k)\,\Sigma_i r_i^2}$ using our existing data set, and can then use the same process as described in equations (A1.19)–(A1.21) to find:

$$ {}_i\Re_i = {}_0\Re_0 + \tfrac{1}{k}\sum diag(C_2) \qquad \text{(eq. A1.22)} $$

where

$$ C_2 = MI_2M^T \qquad \text{(eq. A1.23)} $$

where $\mathbf{I_2}$ is a matrix constructed of 2 × 2 **I** matrices. At this point all values needed to solve for ${}_0\mathfrak{R}_0$ are at least approximated. We are left with our approximation of the ${}_j\mathfrak{R}_i$ value:

$$ {}_j\Re_i^a = {}_i\Re_i - \tfrac{1}{k}\sum diag(C_2) + \tfrac{1}{k}\sum diag(C_r) \qquad \text{(eq. A1.24)} $$

We find that for many fault slip inversions, the use of bound constraints during the initial calculation of ${}_j\mathfrak{R}_i$, although it violates many of the assumptions made in constructing **R**, **N**, etc., results in a slightly lower choice of λ, as would be expected. Synthetic tests using many realizations of noisy data sets and a known input model $\mathbf{m_0}$ with bound constraints on $\mathbf{m_i}^*$ result in values of λ that are consistent with the ones inferred using the ${}_j\mathfrak{R}_i^a$ approach discussed here.

APPENDIX A2

INSAR ACQUISITIONS

Note: All SAR acquisitions used in Chapters 6 and 7. `- interferograms shown in Figures 6.1, 6.2, 7.3, and 7.6 * - ALOS interferogram (All others are Envisat). ^ - Azimuth offsets generated from SAR SLCs. $ - Range offsets generated from SAR SLCs. Bperp is perpendicular baseline between acquisitions in meters. Date 1 is pre-seismic scene, Date 2 is post-seismic scene. Event IDs correspond to those in Table 7.1,7.2 and Figure 7.2, 7.3.

Event	**ID**	**Track**	**Frame**	**Date 1**	**Date 2**	**Bperp**
SFB Events						
2003.07.10	1	478`	3033	2003.03.23	2004.03.07	13
		478	3033	2003.03.23	2004.06.20	146
		478	3033	2003.03.23	2004.07.25	209
2003.11.28	2	249`	3033	2003.10.03	2004.01.16	97
		249	3033	2003.11.07	2004.04.30	530
2005.11.27	3	242	531	2004.07.08	2005.12.15	270
		328	513	2005.01.05	2005.12.21	37
		435`	3069	2005.11.24	2005.12.29	185
2006.03.25	4	206`	3051	2005.05.17	2006.05.02	1
		328	531	2005.05.25	2006.06.14	166
		435	3051	2005.12.29	2009.05.07	104
2006.06.28	5	328`	513	2006.06.14	2006.07.19	790
		435	3069	2006.05.18	2008.04.17	239
2007.03.23	6	99	531	2007.01.29	2009.12.14	32
		99	531	2007.03.05	2009.02.02	79
		206`	3051	2004.12.28	2008.10.28	45
Unknown	7	99`	531	2007.11.05	2009.02.02	79
		206	3051	2006.05.02	2008.05.06	289

2008.09.10	8	328	513	2006.06.14	2008.10.01	360
		435`	3069	2008.04.17	2008.10.09	200
		565*	520	2008.08.19	2008.10.04	405
		566*	520	2008.09.05	2008.10.21	369
2010.07.20	9	142`	513/531	2009.12.17	2010.08.19	305
		249	3051/3069	2010.04.09	2010.10.01	15
		249	3051/3069	2010.06.18	2010.10.01	152
Non-SFB Events						
2003.12.26	14	120`^	3015/3033	2003.12.03	2004.02.11	7
		385	567/585	2003.11.16	2004.02.29	7
		392	3015	2003.10.13	2004.01.26	211
2005.02.22	15	285		2004.09.19	2005.03.13	40
		428	603	2004.07.21	2005.03.23	109
		435$`	2997	2005.02.17	2005.03.24	79
2006.02.28	11	163	3033/3051	2005.05.14	2006.04.29	258
		285`	549	2005.04.17	2006.05.07	256
2006.03.31	12	192`	2925	2006.02.20	2006.05.02	519
2007.08.25	13	56`	549	2007.03.02	2009.03.06	19
		163	3033	2006.04.29	2008.07.12	85
		285	549	2007.02.11	2007.12.23	27
		435	3033	2005.12.29	2009.05.07	86
2010.12.20	16	559*^`	550	2010.06.30	2010.12.31	637
		559*	550	2010.09.30	2010.12.31	217
2011.01.27	17	422`	3033	2011.01.25	2011.02.24	107
		422	3033	2011.01.25	2011.05.25	313

APPENDIX A3

IRAN SLIP DISTRIBUTIONS

Note: All slip distributions from Chapter 6 and 7 with IDs corresponding to Table 7.1. Both north and south dipping fault planes are shown where data cannot discriminate between planes. Maps show surface projection of the fault planes, with red outlines indicating the north dipping plane, purple outlines indicate the south dipping plane. Black lines indicate the top of the fault plane. All slip distributions are viewed orthogonal to the fault plane. Slip distributions and fault locations of the 2010 and 2011 Lut Block events are shown in Figure 7.6.

Event 2005.11.27 (Qeshm 1, ID 3)

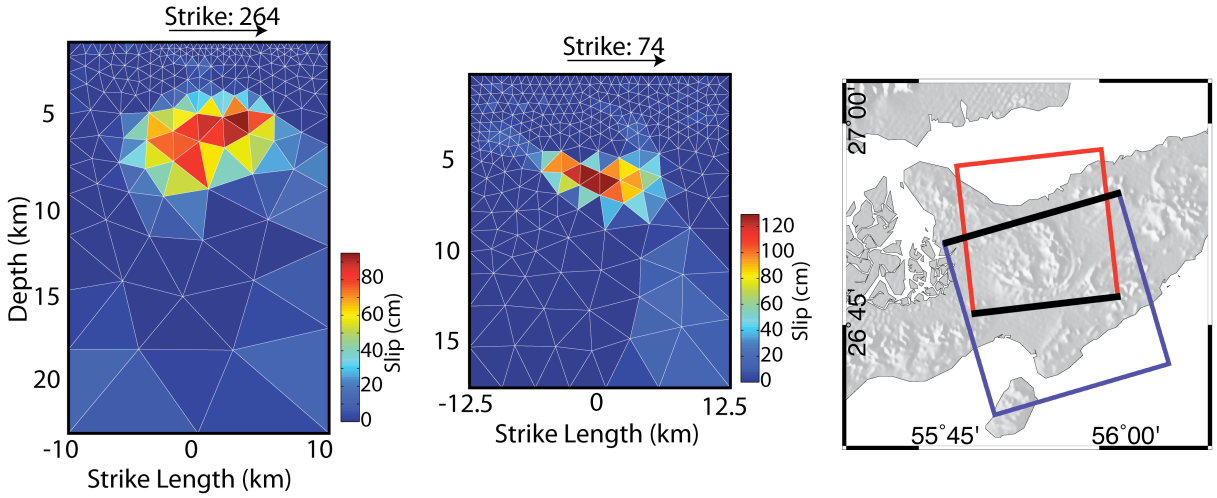

Event 2006.03.25 (Fin, ID 4)

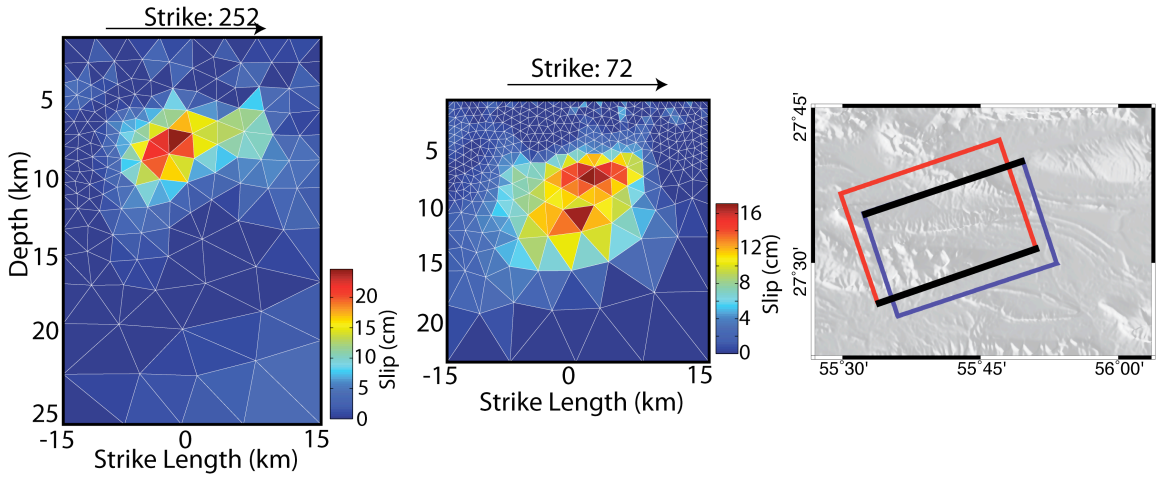

Event 2006.06.28 (ID 5)

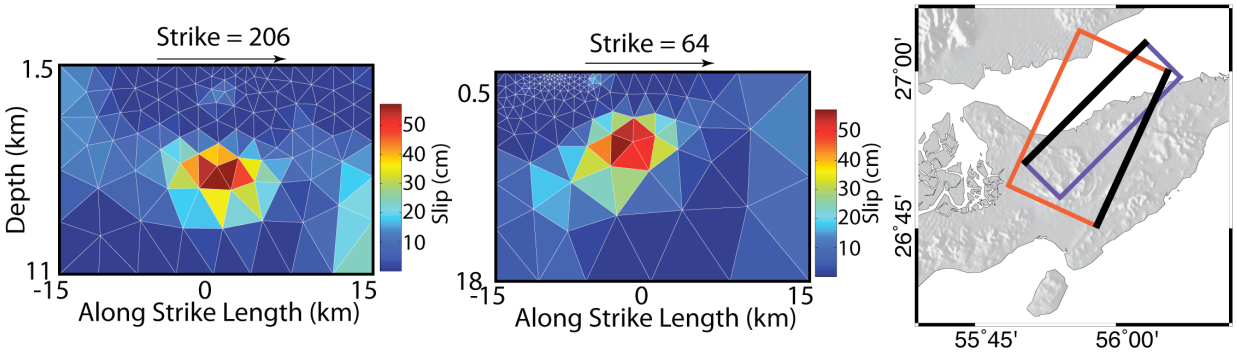

Event 2007.03.23 (ID 6)

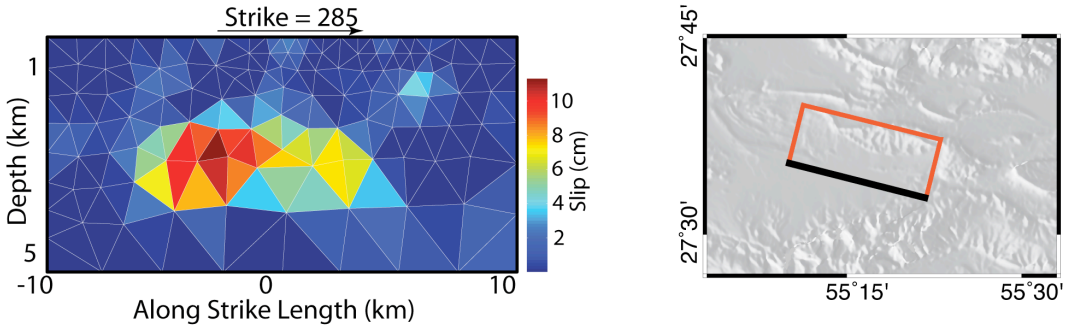

Event 2008.09.10 (ID 8)

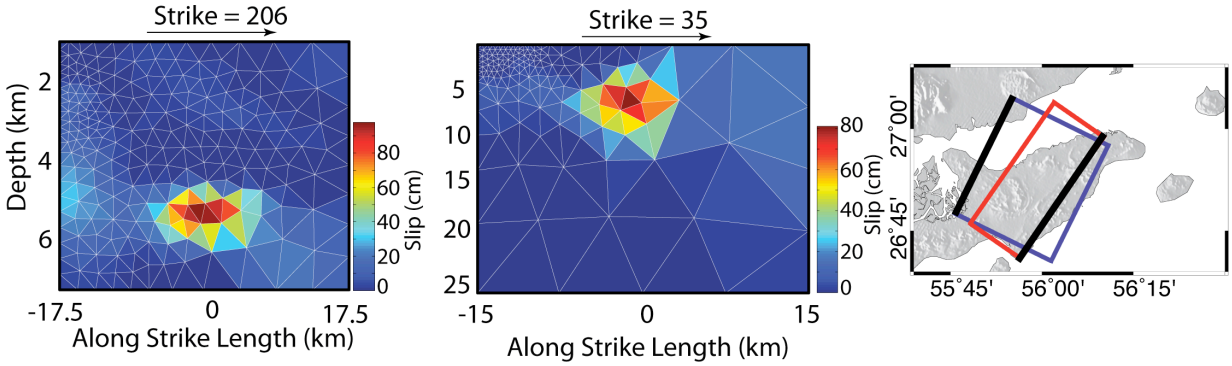

Event 2010.07.20 (ID 9)

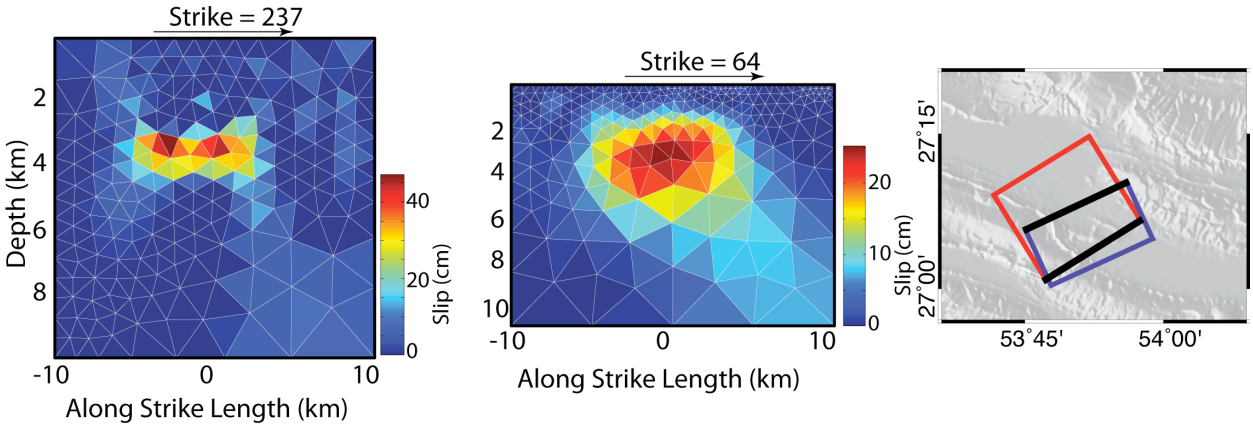

Event 2003.03.31 (ID 12)

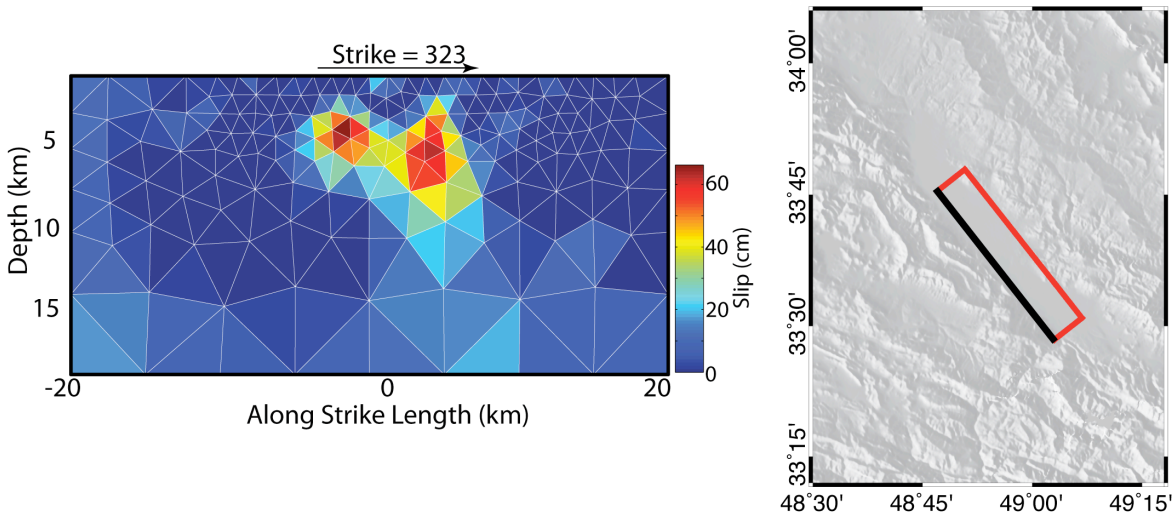

Event 2003.12.26 (ID 14)

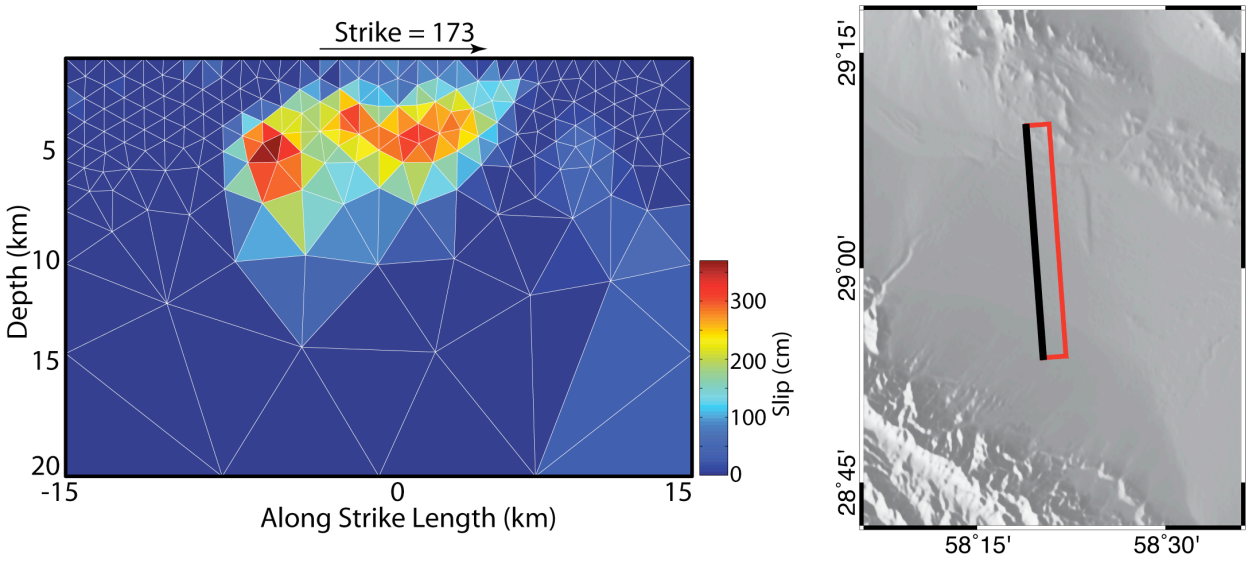

Event 2005.02.22 (ID 15)